Università degli Studi di Ferrara

INTERNATIONAL DOCTORAL COURSE
***EARTH AND MARINE SCIENCES (EMAS)***

CYCLE XXXV

COORDINATOR
Prof. Paolo Ciavola

# New constraints on the physico-chemical state of Earth's upper mantle

Scientific Disciplinary Sector (SDS) GEO/07 PETROLOGY AND PETROGRAPHY

Years 2019/2022

**Candidate**
Dott. Luca Faccincani

**Supervisor**
Prof. Massimo Coltorti

**Co-supervisors**
Prof. Fabrizio Nestola (Unipd)
Prof. Maurizio Mazzucchelli (Unimore)
Prof. Carlo Doglioni (INGV)

*To my mum and dad, for their immense love and unconditional support, guidance, and encouragement every step of the way*

## Table of contents

**Abstract** ..... **1**

**1. Introduction** ..... **4**

1.1 Earth's upper mantle: general overview ..... 4

1.2 Inclusions in diamonds as probes of Earth's upper mantle (and deeper) ..... 8

1.2.1 Diamond formation and the link to oxygen fugacity ..... 11

1.3 Seismic reference models of Earth's upper mantle and the relationships between the elastic properties of minerals and propagating sound waves ..... 14

1.3.1 Fitting Equations of State (EoS) ..... 20

1.4 Evidence of the presence of water in Earth's upper mantle ..... 23

1.4.1 Effects of water incorporation on the physical properties of NAMs ..... 26

References ..... 29

**2. Methods** ..... **36**

2.1 Synchrotron Mössbauer spectroscopy ..... 36

2.2 Single-crystal X-ray diffraction ..... 39

2.2.1 Structure refinements ..... 42

2.3 Brillouin spectroscopy ..... 44

References ..... 47

**3. Relatively oxidized conditions for diamond formation at Udachnaya (Siberia)** ..... **49**

3.1 Introduction ..... 50

3.2 Experimental approach ..... 52

3.2.1 Synchrotron Mössbauer spectroscopy ..... 52

3.2.2 Single-crystal X-ray diffraction ..... 53

3.3 Results ..... 53

3.3.1 Synchrotron Mössbauer spectroscopy ..... 53

3.3.2 Single-crystal X-ray diffraction ..... 55

3.4 Discussion ..... 56

3.4.1 Thermobarometric analysis of the inclusion pair and thermal state of the mantle ..... 56

3.4.2 $fO_2$ analysis of the inclusion pair and oxidation state of the mantle ..... 60

3.4.3 Implications for the redox state evolution and diamond formation ..... 63

3.5 Summary and conclusions ..... 66

Author contribution ..... 66

Acknowledgments ..... 67

Financial support ..... 67

Appendix A. Supplementary data ..... 67

References ..... 67

**4. EoS of mantle minerals coupled with composition and thermal state of the lithosphere: Inferring the density structure of peridotitic systems ..... 73**
4.1 Introduction ..... 74
4.2 Data selection and EoS fitting ..... 76
4.2.1 Orthopyroxene ..... 77
4.2.2 Clinopyroxene ..... 78
4.2.3 Spinel ..... 79
4.2.4 Garnet ..... 80
4.3 Density variations in the lithospheric mantle ..... 82
4.3.1 Density calculations ..... 82
4.3.2 Results ..... 86
4.3.3 Discussion ..... 89
4.3.3.1 Density models and the effect of the thermal state ..... 89
4.3.3.2 Comparison between Perple_X and simplified calculations ..... 91
4.4 Concluding remarks ..... 93
Author contribution ..... 94
Acknowledgments ..... 94
Funding ..... 94
Appendix A. Supplementary data ..... 95
References ..... 95
**5. Sound velocities and single-crystal elasticity of hydrous Fo90 olivine to 12 GPa ..... 99**
5.1 Introduction ..... 100
5.2 Materials and methods ..... 102
5.3 Results and discussion ..... 105
5.3.1 Compressibility of hydrous Fo90 olivine ..... 105
5.3.2 Sound wave velocities of hydrous Fo90 olivine and $c_{ij}$ inversion strategy ..... 108
5.3.3 Elastic properties of hydrous Fo90 *vs* anhydrous Fo90 olivine ..... 113
5.3.4 Effect of hydration on sound wave velocities of Fo90 olivine and its geophysical implications ..... 118
5.4 Concluding remarks ..... 121
Author contribution ..... 121
Acknowledgments ..... 122
Appendix A. Supplementary data ..... 122
References ..... 122
**6. Conclusions and future perspectives ..... 127**
**Acknowledgements ..... 130**

# Abstract

**New constraints on the physico-chemical state of Earth's upper mantle.** Understanding the many physico-chemical features of Earth's upper mantle which play a key role in important geological processes, such as diamond formation, plate tectonics, deep water cycle, etc. has crucial significance and is one of the major frontiers in Earth sciences.

This thesis focuses on the physico-chemical state, structure, rheology, and dynamics of Earth's upper mantle, with three manuscripts addressing different aspects of the topic: project (1) provides petrological insights into an inclusion trapped in a Siberian diamond, and explores the (favourable) $fO_2$ conditions for diamond formation; project (2) presents an assessment of the Equations of State (EoS) of major mantle minerals, and combines such EoS to investigate the density structure of the lithospheric mantle; project (3) reports high-pressure single-crystal X-ray diffraction and Brillouin scattering experiments on Fo90 olivine with ~0.20 wt.% $H_2O$ to place constraints on the effect of hydration on olivine elastic properties and sound wave velocities.

In project (1) – **Relatively oxidized conditions for diamond formation at Udachnaya (Siberia)** – a magnesiochromite-olivine touching pair hosted in a diamond from the Udachnaya kimberlite (Siberia) has been investigated by in situ single-crystal X-ray diffraction, to assess mineral chemical compositions through structure refinements, and energy-domain synchrotron Mössbauer spectroscopy to determine the $Fe^{3+}/\sum Fe$ ratio for magnesiochromite. These measurements are critical to place constraints on both the physical-chemical conditions of diamond formation and the redox state of this portion of the Siberian craton when the diamond was formed. Thermo-/oxybarometric analyses indicate the $P$–$T$–$fO_2$ conditions of the inclusion pair at the time of entrapment in its host diamond to be ~5.7(0.4) GPa, ~1015(50) °C (although entrapment at higher $T$ and re-equilibration during subsequent mantle storage are also possible) and $fO_2$ near the enstatite-magnesite-olivine-diamond (EMOD) buffer. The determined $fO_2$ is similar to, or slightly more oxidized than, those of xenoliths from Udachnaya, but whilst the last equilibration of xenoliths with the surrounding mantle occurred just prior to their entrainment in the kimberlite at ~360 Ma, the last equilibration of the inclusion pair is much older, occurring at 3.5–3.1, ~2 or ~1.8 Ga before final encapsulation in its host diamond. This similarity suggests that the redox state of this portion of the Siberian lithosphere was attained relatively early after its formation and may have persisted for billions of years, at least at the local scale. The calculated $fO_2$ values for the inclusion pair are also found to be good indicators of the redox conditions of diamond

formation and provide direct evidence that this diamond formed near the EMOD buffer. This is consistent with recent models suggesting relatively oxidized, water-rich CHO fluids as the most likely parents for lithospheric diamonds.

In project (2) – **EoS of mantle minerals coupled with composition and thermal state of the lithosphere: Inferring the density structure of peridotitic systems** – an assessment of the Equations of State of mantle orthopyroxene, clinopyroxene, spinel and garnet based on X-Ray diffraction data and direct elastic measurements available in literature has been presented. Determination of the thermoelastic parameter of major mantle minerals is important for modelling the density and seismic velocities of the lithospheric mantle. The new EoS, in combination with those published for mantle olivine and magnesiochromite, have been used to evaluate the influence of bulk composition (fertile lherzolite *vs* depleted harzburgite) and thermal regimes on the density structure of potential lithospheric mantle sections. Under cold thermal conditions (35 mW $m^{-2}$), the density of both depleted and fertile peridotitic systems progressively increases with increasing depth. In mantle sections characterized by intermediate geotherms (45 mW $m^{-2}$), the density of the depleted peridotitic system remains nearly constant down to ca. 4 GPa, whereas it moderately increases in the fertile system due to higher modes of garnet. Under relatively hot thermal conditions (60 mW $m^{-2}$), the density of both systems progressively decreases up to ca. 3 GPa, and then increases downwards. These results have been calculated following a simplified parameterisation (no phase relations allowed, mineral modes only vary across the spinel-garnet transition) and have been compared with classic thermodynamic modelling results from literature. The agreement between the two models further corroborates the conclusion that the density structure of the lithospheric mantle is predominantly controlled by the thermal gradient variations, whereas the compositional control may be less than previously suggested.

In project (3) – **Sound velocities and single-crystal elasticity of hydrous Fo90 olivine to 12 GPa** – the single-crystal elasticity of Fo90 olivine with ~0.20 wt.% $H_2O$ has been determined by means of high-pressure single-crystal X-ray diffraction and Brillouin spectroscopy experiments. Plate tectonics on Earth is integrated into global material cycles that exchange chemical components between Earth's surface and Earth's mantle. Subduction zones are the primary carriers of water into the mantle and when water is hosted in the crystalline structures of nominally anhydrous minerals, it alters their physical properties. Experimental data on water solubility in olivine indicate that 0.2–0.5 wt.% $H_2O$ can be

hosted in its crystal structure at deep upper mantle conditions. Although water incorporation in olivine has long been known to have substantial effects on many of its physical and chemical properties, the results of this study show that the sound wave velocities of hydrous and anhydrous olivines are indistinguishable within uncertainties at pressures corresponding to the base of the upper mantle. Therefore, if amounts of water were to be incorporated into the crystal structure of Fo90 olivine, its elastic and seismic behaviour at high pressure would likely remain unchanged. This suggests that water in olivine is not seismically detectable, at least for contents consistent with deep upper mantle conditions. Moreover, the incorporation of water in olivine is unlikely to be a key factor in reconciling seismological observations at the 410-km discontinuity with a pyrolitic mantle, but rather corroborates previous evidence of a deep upper mantle that is less enriched in olivine than the pyrolite model.

# 1. Introduction

Earth is a dynamic planet. From a geological perspective, the most unique traits of Earth, compared to other bodies in the Solar System, are active plate tectonics, i.e., the fragmentation of Earth's outer shell into rigid plates that are in relative motion to one another, and oceans, more than 70% of Earth's surface being covered by water. The dynamic view of Earth was developed in the late 1960's, at the point when Alfred Wegener's theory of continental drift, originally conceived fifty years earlier, was merged with the theory of plate tectonics, and these concepts gained acceptance and became cornerstones between geoscientists. This fostered an interest in the dynamics of the deep Earth and made more evident the close link between processes occurring at Earth's surface and depths, giving new momentum to the geoscience community.

One of the major challenges in Earth sciences is to understand the many facets of Earth's mantle physico-chemical state, structure, and dynamics, and their implication for large-scale geological processes. This requires a multidisciplinary approach, where petrological-geochemical studies on natural samples must be complemented with, and compared to, thermodynamic modelling, laboratory experiments at high pressure and temperatures as well as geophysical data.

This chapter provides an introduction to our current knowledge of the structure and mineralogy of Earth's upper mantle. Key ingredients fostering this progress are our improved understanding of the physico-chemical properties of geological materials under relevant mantle conditions, and the possibility to retrieve the pressure and the temperature at which minerals and rocks come from or, conversely, reproducing experimentally those conditions. Emphasis will be given to mineralogical models of Earth's upper mantle, which are both inferred and constrained by petrological studies of mantle xenoliths and diamonds, and seismological observations. The relationships between the elastic properties of minerals and the propagation of sound waves are introduced, together with an overview of the evidence of water in Earth's mantle and its effect on the elastic properties of nominally anhydrous minerals.

## 1.1 Earth's upper mantle: general overview

The broad-scale internal structure of Earth is well known from the analysis of seismic observations of body waves ($v_P$ and $v_S$) that propagate through it. Earth is conventionally divided into three main layers – the crust, the mantle, and the core – but each of these has further subdivisions that are almost as fundamental. Both $v_P$ and $v_S$ are triggered by natural

earthquakes all around the globe. After propagating through Earth's interior, body waves are detected by arrays of seismometer stations distributed across the world and the travel times of direct and reflected waves offer the most direct and precise information on the structure, composition, temperature, and physical state of Earth's upper mantle (UM) and its deeper portions. However, interpreting seismic travel time information requires knowledge of the mineralogical composition of the UM. As if they were in *Voyage au centre de la Terre* novel by Jules Verne, geologists have been striving to investigate the nature of Earth's building blocks since the XVIII century and are still contributing to establishing a more and more clear picture.

In this context, the knowledge of the composition and the mineralogy of the UM, and therefore its physico-chemical properties, derives from both petrological-geochemical studies of natural samples (mantle xenoliths, inclusions in diamonds, tectonically exposed mantle sections, etc.) and indirect investigations (laboratory experiments at relevant pressure and temperature conditions, thermodynamic calculations, etc.).

Earth's UM extends from the base of the crust down to about 660 km (boundary with the lower mantle) and its deeper portion, located between a depth of 410 and 660 km, is referred to as mantle transition zone (MTZ). Nonetheless, direct evidence of 'how the UM looks like' is restricted to its shallower part, i.e., the lithosphere. Indeed, natural mantle-derived samples originate from depths up to ~250 km and reveal much about the physical, thermal, and compositional characteristics of the lithospheric UM, showing that peridotites – ultramafic rocks composed of variable amounts of olivine, orthopyroxene, clinopyroxene and an additional aluminous phase that changes from plagioclase to spinel and then to garnet with increasing pressure – dominate its mineralogical composition, with minor eclogites and pyroxenites. The widespread occurrence of mantle xenoliths from all over the world shows that the lithospheric mantle, at least underneath continents, comprises a variety of peridotite rocks, ranging from lherzolites, harzburgites to dunites (e.g., Coltorti et al., 2021; Faccini et al., 2020; Ionov et al., 2010; Melchiorre et al., 2020; Rizzo et al., 2021, 2018).

Experimental data (e.g., Ghiorso and Sack, 1995; Presnall et al., 2002; Walter, 1998) show that partial melting of lherzolites (up to ~30%) produces basaltic melts, leaving residual harzburgites or dunites, depending on the extent of melt extraction they experienced. However, the formation of dunites is more likely to be the result of combined partial melting and ascending melts deriving from deeper mantle levels, which dissolve pyroxene and precipitate olivine at the level of dunite occurrence (e.g., Braun and Kelemen, 2002; Mazzucchelli et al., 2009). During the process of partial melting, incompatible elements (such as Ca, Al, Na) are preferentially partitioned into the melt whereas compatible elements

(especially Mg) remain in the solid residual mantle. Therefore, partial melting induces a significant variability between mantle peridotites, evidence of which are being found in their chemical compositions, which range from fertile Ca-, Al-, Na-rich lherzolites to depleted/ultradepleted Mg-rich and Ca-, Al-, Na-poor harzburgites/dunites (e.g., Carlson et al., 2005; Fumagalli and Klemme, 2015; McDonough and Rudnick, 1998; Pearson et al., 2003). Although the melting process of peridotites is complex and involves all mantle minerals, the more evident mineralogical expression of the transition from fertile to depleted peridotites is the decrease, or loss, of clinopyroxene (e.g., Arai, 1994; Bénard et al., 2018; Niu et al., 1997). The knowledge of the mineralogical composition of the UM is essential to derive its density structure, which is also a prerequisite to interpreting seismic travel time information. In this context, Chapter 4 will present an assessment of the density structure of the lithospheric mantle, taking into consideration the influences of different bulk compositions (lherzolitic *vs* harzburgitic) and thermal regimes.

Evidence for another source of variability in mantle peridotites has been extensively documented and is related to metasomatic processes. Mantle metasomatism refers to compositional/modal changes in peridotites caused by the percolation and interaction of mantle fluids/melts with the overlying mantle, which leads to the formation of refertilised lithologies (e.g., Aulbach et al., 2013; Casetta et al., 2022; Coltorti et al., 1999; Dawson, 2002; Rivalenti et al., 2007). The examples of mantle metasomatism involve an enormous variety of melt/fluid types, including silicate melts, carbonatite or carbonated melts, sulphide melts, CHO-bearing fluids ranging from $H_2O$, $CH_4$, and $CO_2$, dense brines and hydrous silicic fluids, hydrocarbon-bearing fluids (the reader is referred to O'Reilly and Griffin, 2013 for a review).

The lithospheric UM is a palimpsest recording the multiple events of melt extraction and metasomatism/refertilisation that have repeatedly modified and overprinted the pristine mantle signature. Reconstructing the prolonged and complex record of the lithospheric mantle is a prerequisite to unravelling the nature and evolution of the lithosphere and may also provide important insights into how and where volatiles are stored and/or migrate through the deep Earth.

In most cases, therefore, natural samples derived from the lithospheric UM have been modified by the processes of partial melting and metasomatism compared to the underlying asthenospheric UM or what might be considered the pristine mantle. Much remains to be learned about the physical and chemical properties from which the rheological differences between the lithosphere and asthenosphere arise (e.g., Anderson, 1995; Fischer et al., 2010), but the chemically depleted signature of lithospheric peridotites has been recognized among

the factors. In this context, the most common petrological model of a primitive mantle composition, called pyrolite, was introduced by Ringwood (1975). The starting point of this model is the notion that the partial melting of fertile peridotites generates basalts and, from this line of argument, that the compositions of residual peridotites and basalts are somewhat complementary to one another. Therefore, the pyrolite composition is obtained by mixing the known products of peridotites partial melting with the residues, i.e., a mixture comprised of a 1:4 ratio of MORB (mid-oceanic ridge basalt) and harzburgite components, respectively. Investigations of the UM mineralogy using pyrolitic and harzburgitic compositions (Figure 1.1) indicate that it is predominantly constituted by olivine, pyroxenes, and garnet up to the MTZ at ~410 km depth (about 14 GPa), where α-olivine transforms to its high-pressure polymorph wadsleyite, referred to as β-phase or modified spinel. This transition is widely accepted to cause the discontinuity in seismic wave velocity observed globally at this depth (e.g., Akaogi et al., 1989; Frost, 2008; Katsura et al., 2004; Katsura and Ito, 1989).

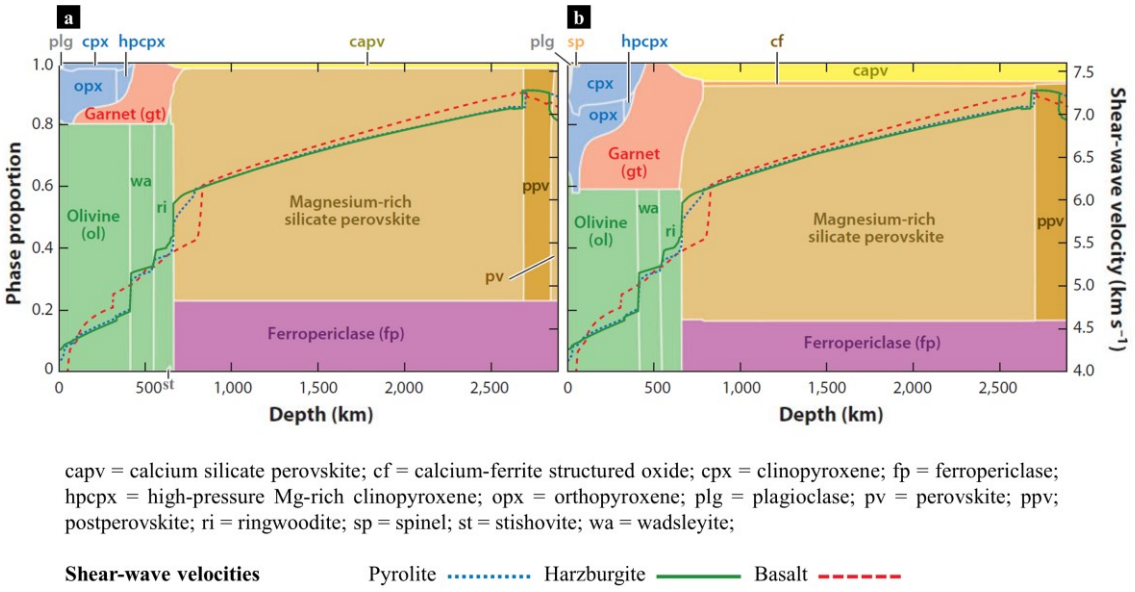


**Figure 1.1.** Phase proportions (expressed as atomic fractions) of (a) harzburgite and (b) pyrolite calculated along the mantle adiabat. Shear-wave velocities (see section 1.3) of pyrolite (dotted blue line), harzburgite (solid green line), and basalt (dashed red line) are superimposed and repeated in both panels. Adapted from Stixrude and Lithgow-Bertelloni (2012).

Because mantle-derived samples originate from depths restricted to a maximum of ~250 km, investigating the mineralogical, thermal, and chemical structure of the deep UM mantle principally relies on the interpretation of geophysical observations, primarily those from seismology. In general terms, the physical (e.g., temperature) and chemical properties of the mantle can be constrained by examining the mismatch between the observed seismic wave velocities with those calculated for a specific mineral assemblage (reflecting a chosen

average composition) using either thermodynamic concepts or experimental data from mineral physics (e.g., Bass and Anderson, 1984; Frost, 2008; see section 1.3). In this context, geophysical studies made more evident that heterogeneities are not restricted to the lithospheric UM, but are ubiquitous also in the deeper, asthenospheric portions of the UM, both radially and laterally, that is, velocities at a given depth in different parts of the globe are different from one another (e.g., Su et al., 1994). Convection in Earth's mantle gives rise to horizontal density variations causing lithospheric plate motions at Earth's surface, which is also the engine for subduction zones in convergent plate boundaries, variations in seismic velocity discriminate the two main different types of lithospheres, oceanic *vs* continental, which can be further distinguished (e.g., high seismic velocities of the thick, cold lithosphere of Precambrian cratons, compared to younger, Phanerozoic units; Schaeffer and Lebedev, 2015), etc. Therefore, heterogeneity can be observed in several different ways, each yielding a complementary perspective on the Earth's bulk properties, structure, and dynamics.

## 1.2 Inclusions in diamonds as probes of Earth's upper mantle (and deeper)

Research into natural diamonds and their mineral inclusions has emerged over the last decades as one of the keys to understanding the deep Earth. Virtually all diamonds (98%, defined as 'lithospheric') are interpreted to have formed beneath cratons, ancient and deep-reaching continental blocks, at depths between about 130–230 km, in the so-called diamond window, where lithosphere and diamond stability field overlap (e.g., Stachel et al., 2022; Stachel and Harris, 2008). The diamond window is bounded at the top by the graphite-diamond (G-D) transition and at the bottom by the maximum thickness of the non-convecting mantle, that is the lithosphere. Such enormous lithospheric thicknesses are only achieved beneath cratons (Figure 1.2). The remaining and very rare counterpart (2%, defined as 'superdeep') are believed to form at depths exceeding the lithosphere, 300–800 or more km (Harte, 2010; Kaminsky, 2012; Walter et al., 2011), even though the real depth of origin has been established in rare cases (e.g., Nestola et al., 2018; Pearson et al., 2014).

Diamonds are thus the deepest-sourced terrestrial samples that are carried to Earth's surface from the mantle as xenoliths either slowly, by complex geodynamic phenomena such as mantle convection, or more rapidly, by explosive eruptions of volatile-rich magmas such as kimberlites, lamproites, and occasionally lamprophyres (Gurney et al., 2010).

About 1% of the lithospheric diamonds (Stachel and Harris, 2008) contain mineral inclusions that were trapped during diamond growth. The physical strength and chemically inert nature

of their diamond hosts protect inclusions from alteration or re-equilibration processes during exhumation, which then may remain pristine and thus represent key geological samples, revealing the physico-chemical environment in which their host diamonds were formed.

The distribution of diamonds in the Earth's mantle has been indirectly inferred from the characterization of their mineral inclusions. In this regard, the chemical composition of mineral inclusions can be related to the source mantle rock in which the host diamonds formed. Inclusions in diamonds derived from the subcratonic lithospheric mantle are conventionally divided into three suites, the former of which is predominant: (i) a peridotitic (P-type) suite (65%), (ii) an eclogitic (E-type) suite (33%); (iii) a websteritic suite (2%) (Meyer, 1987; Stachel and Harris, 2008). While the nature and relative abundance of E-type and websteritic-type mineral inclusions are respectively consistent with the eclogitic and pyroxenitic bulk rock mineral modes, P-type mineral inclusions – 29% garnet, 28% olivine, 27% magnesiochromite, 12% orthopyroxene, 4% clinopyroxene, further subdivided in harzburgitic and lherzolitic paragenesis (~7:1 ratio) – are consistent with a peridotite source rock, but their relative abundances markedly differ relative to the typical abundance in cratonic peridotites (McDonough and Rudnick, 1998). This evidence suggests (but it is still largely unknown) (i) preferential nucleation of diamonds on garnet and magnesiochromite, or (ii) the presence of chromite-rich / garnet-rich rocks in the mantle percolated by diamond-forming fluids/melts. Moreover, the ~2:1 ratio of peridotitic to eclogitic suite diamonds is at odds with the < 1 to 5% estimated volumetric abundance of eclogite in the subcratonic lithospheric mantle. Overall, this indicates that harzburgite and eclogite are strongly preferred substrates for diamonds, compared to lherzolite (Stachel and Luth, 2015).

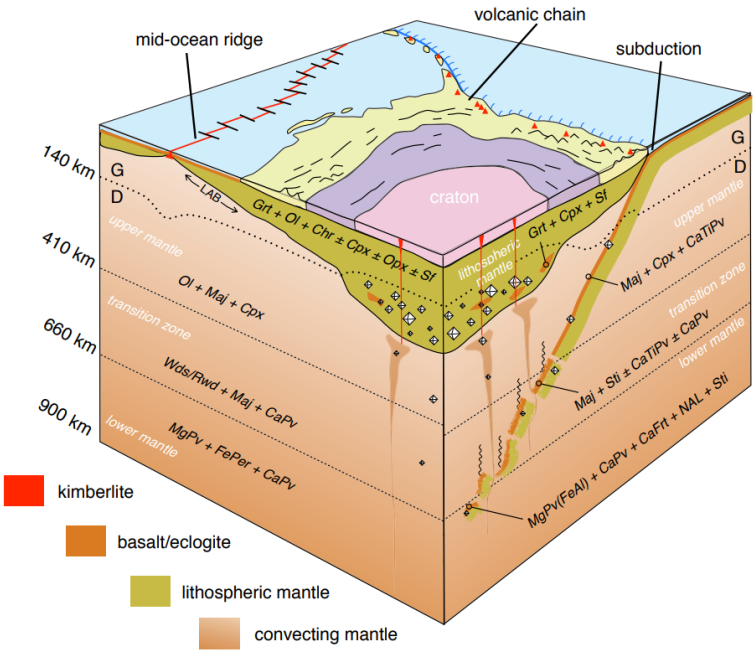

**Figure 1.2 (on the preceding page).** Schematic block diagram showing the basic relationship between a continental craton, its lithospheric mantle keel and diamond stable regions in the keel, and the convecting mantle. Under the right conditions, diamonds can form in the convecting mantle, the subducting slab, and the mantle keel. The reported assemblages give the expected inclusions to be found in peridotitic or ultramafic (left) and eclogitic or basaltic (right) rock compositions. G=graphite, D=diamond, LAB=lithosphere/asthenosphere boundary (from Shirey et al., 2013).

Mineral inclusions can be both found as individual minerals or coexisting minerals within the same diamond, either as separate (i.e., non-touching) or as intergrowths (i.e., touching), from which estimates of the last equilibration *P–T* conditions can be obtained by thermobarometry. Chemical thermobarometers are formulations that allow to retrieve the pressure and/or temperature of the formation of a mineral species or mineral assemblage knowing the chemical compositions, and how compositions are expected to vary with *P* and/or *T*. Elastic methods (Angel et al., 2014a) provide a potential alternative to chemical thermobarometry for the evaluation of the pressure of formation of a diamond containing an individual inclusion, if *T* is known independently (e.g., from nitrogen aggregation thermometry), but will not be further discussed. Chemical thermobarometers are based on chemical equilibria between at least two phases, but certain approximate formulations consider only the composition of a single phase, assumed to be in equilibrium with another phase capable of buffering its composition under certain pressures and temperatures (e.g., Shirey et al., 2013). In general, the resulting *P–T* estimates for individual and non-touching pairs inclusions reflect the conditions of diamond formation. The overall distribution of pressure estimates for worldwide lherzolitic and harzburgitic diamonds has a mode at ~5–6 GPa, corresponding to depths of ~175 ± 15 km, and temperatures of 1130 ± 120 °C (Stachel and Harris, 2008; Stachel and Luth, 2015). Conversely, two-mineral thermobarometry of touching-pair inclusions, although does provide the depth of provenance of the diamond, may not necessarily deliver the temperature of diamond formation, given that inclusions may re-equilibrate to ambient conditions during long-time mantle storage (Stachel and Harris, 2008). Indeed, diamonds are thought to be among the oldest available terrestrial samples, their residence time in the mantle being on the order of billions of years (e.g., Richardson et al., 1984; Shirey and Richardson, 2011). At present, it is still not possible to date monocrystalline diamonds by direct analysis of the diamond crystal itself, and diamond ages are indirectly extrapolated based on the radiometric dating of their mineral inclusions. However, not all inclusions in diamonds formed (and got trapped) at the same time as their diamond host, that is, they are syngenetic (Meyer, 1987). Protogenetic inclusions, representing pre-existing material passively incorporated in their diamond host during its growth, have been documented (e.g., Milani et al., 2016; Nestola et al., 2019, 2017, 2014).

While syngenesis implies that inclusions would presumably be in equilibrium with the diamond-forming medium, the composition of protogenetic inclusions may or may not be fully reset before their entrapment, which raises the question as to the reliability of the genesis ages of diamonds using mineral inclusions. Nonetheless, diffusion modelling studies in garnets (Sm-Nd), sulphides (Re-Os), and clinopyroxenes (Sm-Nd) inclusions at relevant pressures and temperatures (Nestola et al., 2019a; Pamato et al., 2021; Pasqualetto et al., 2022) demonstrated that isotopic resetting would generally occur for small inclusions (e.g., < 200 μm for clinopyroxene) over geologically short time scales, that is, diamond formation is likely to generate isochronous relationships despite protogenicity.

### 1.2.1 Diamond formation and the link to oxygen fugacity

Diamond formation in the mantle is commonly considered to be a metasomatic process. The metasomatic agent is generally referred to as CHO-bearing fluid or melt, which percolates through mantle rocks over a large range of depths and generates diamonds (e.g., Shirey et al., 2013; Stachel et al., 2005). By comparing inclusion-based temperature estimates to experimentally determined solidus temperatures for diamond host lithologies, some constraints can be placed on the fluid *vs* melt nature of the diamond-forming medium.

The key argument supporting the involvement of supercritical CHO-bearing fluids in the formation of diamonds is the close association between diamonds and highly depleted cratonic peridotites (harzburgites, dunites), which is explained by the fact that an average cratonic model geotherm (e.g., 40 $mW/m^2$; Hasterok and Chapman, 2011) intersects the carbonated, hydrous solidus of harzburgite at ~1300 °C. Therefore, except for the deepest regions located near the lithosphere-asthenosphere boundary, diamond formation in strongly depleted substrates occurs predominantly under subsolidus conditions. On the other hand, thermobarometric calculations for a worldwide database of lherzolitic and eclogitic inclusions in diamond indicate growth in the presence of a melt, as they dominantly fall above the solidi for carbonated lherzolite and carbonated eclogite, respectively (Stachel and Luth, 2015).

The traditionally accepted model of diamond formation involves redox reactions between such percolating carbon-bearing fluids/melts and their wall rocks. These reactions would either involve the reduction of carbonate-bearing (or $CO_2$-bearing) fluids or melts, or oxidation of $CH_4$-bearing fluids, depending on the relative redox states of the metasomatic agent and the wall rocks, simple examples of which are:

$$CO_2 = C + O_2 \quad or \quad CO_3^{2-} = C + O_2 + O^{2-} \tag{1.1}$$

$$CH_4 + O_2 = C + 2H_2O \tag{1.2}$$

Therefore, diamond formation is intimately associated with the oxidation state of mantle rocks, which is mostly controlled and expressed by the $Fe^{3+}/Fe^{2+}$ equilibria between minerals (e.g., Frost and McCammon, 2008). Equations (1.1) and (1.2) require the mantle to act as a source or sink for the quantity of $O_2$ needed for diamond precipitation; in other words, the assumption which underpins the model of diamond formation is that the oxygen fugacity is controlled (i.e., buffered) by the host rocks.

Lithospheric diamonds originate in the cratonic lithosphere and so the prevailing oxygen fugacity in cratonic mantle peridotites is important to consider. Earth's mantle oxidation state is usually addressed in terms of oxygen fugacity, $fO_2$ (by convention log $fO_2$), and oxygen buffers, i.e., assemblages which control the chemical potential of oxygen by chemical reactions. In general, log $fO_2$ absolute values are expressed relative to the FMQ buffer – Fayalite-Magnetite-Quartz – as $\Delta$log $fO_2$ (FMQ).

In diamond studies, it is convenient to introduce specific buffers to bound the diamond stability field relating to $fO_2$ conditions (Frost and McCammon, 2008; Figure 1.3).

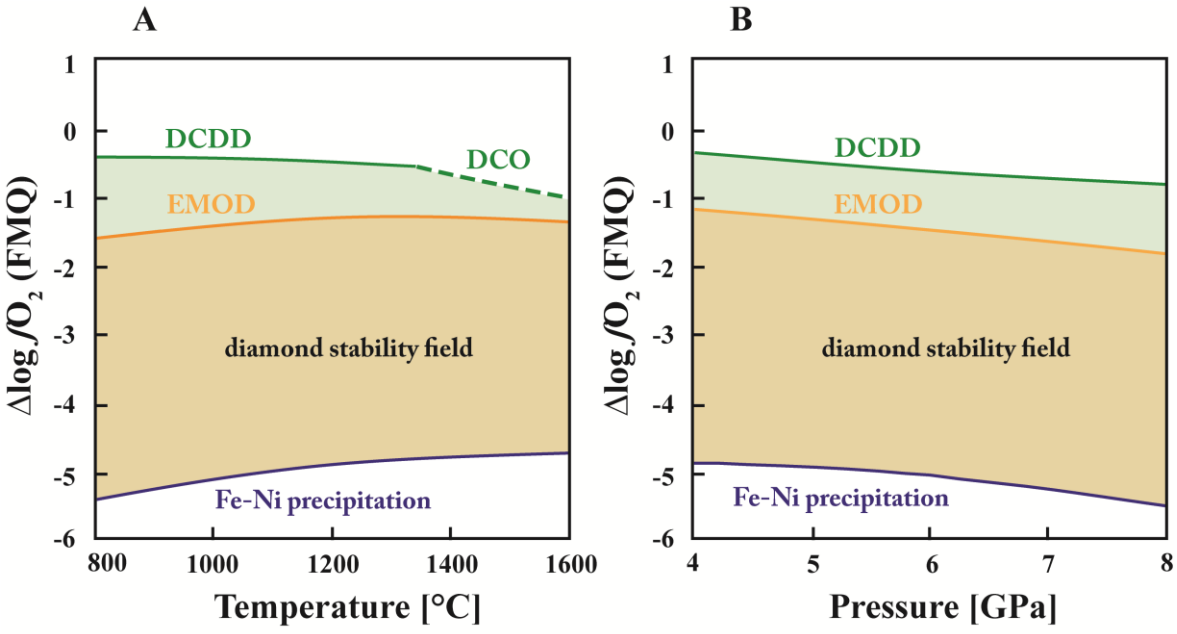


**Figure 1.3.** (a) Location of buffer curves that determine the speciation of carbon in $\Delta$log $fO_2$ (FMQ) – $T$ space, at $P$ = 5 GPa, and (b) in $\Delta$log $fO_2$ (FMQ) – $P$ space, calculated along an average (40 mW $m^{-2}$) cratonic geothermal. Diamond stability field in peridotite rocks is shown in yellow, whereas the additional field of stability in eclogitic rocks, in virtue of the DCDD buffer being ca. 1 log unit above the EMOD, is shown in green (adapted from Shirey et al., 2013)

These buffers include the DCO, defined as:

$$C_{diamond} + O_2 = CO_{2\,fluid} \quad (1.3)$$

which marks the highest $fO_2$ at which diamonds can form with respect to a $CO_2$ fluid, the DCDD, defined as:

$$\begin{aligned} CaMg(CO_3)_{2\,dolomite} + 2SiO_{2\,coesite} \\ = CaMgSi_2O_{6\,diopside} + 2C_{\,diamond} + 2O_2 \end{aligned} \quad (1.4)$$

which sets the upper limit of $fO_2$ at which diamond could form within carbonated eclogitic assemblages, the EMOD, defined as:

$$MgSiO_{3\,enstatite} + MgCO_{3\,magnesite} = MgSiO_{4\,olivine} + C_{\,diamond} + O_2 \quad (1.5)$$

corresponding to the highest $fO_2$ at which diamond could form within carbonated peridotite assemblages, and the Fe-Ni precipitation curve, which denotes the conditions at which Ni-rich Fe alloys start to precipitate and the lowest $fO_2$ at which diamond could form.

The implicit view of the mantle acting as an oxidizing or reducing agent for the traditional models of diamond formation has recently been challenged by Luth and Stachel (2014) and Stachel and Luth (2015). Thermodynamic calculations showed that peridotites are very poor sinks or sources of $O_2$ for possible redox reactions to form diamonds. A corollary of these results is that the lithospheric mantle $fO_2$ is unlikely to be rock-buffered, but rather is fluid-buffered, i.e., the $fO_2$ of host rocks may be easily reset to that of the metasomatic fluid that percolates through them. Thermodynamic modelling of CHO-bearing fluids (Luth and Stachel, 2014; Stachel and Luth, 2015) indicates that for fluids with composition near the water maximum (i.e., $O/(O+H)_{mol}$ ~0.33, taking place at $fO_2$ near the EMOD buffer) decreasing temperature or ascent along a conductive geotherm lower the carbon solubility in these fluids and may provide alternative modes of diamond formation. In this context, Chapter 3 will present a petrological investigation of a touching-pair inclusion hosted in a lithospheric diamond, as well as a more detailed discussion about diamond formation from CHO-bearing fluids.

Diamonds containing mineral inclusions are of paramount importance as they provide fragments of the Earth's mantle which can deliver unique information on processes and conditions occurring in the deep regions of our planet. Because of their rarity, however, geophysical observations are required to place further constraints on the mineralogy and structure of Earth's UM, and deeper interior.

## 1.3 Seismic reference models of Earth's upper mantle and the relationships between the elastic properties of minerals and propagating sound waves

Perhaps, one of the most popular ways to constrain the physical and chemical properties of the mantle is to assume a mantle bulk composition (e.g., pyrolite, harzburgite, etc.), determine the stable phase assemblage as a function of depth either in high-pressure, high-temperature experiments or phase equilibria calculations (e.g., Connolly, 2009), calculate the sound velocities for the assemblage and compare them with seismic reference models for global body wave velocity structure, such as PREM (preliminary reference Earth model; Dziewonski and Anderson, 1981) or AK135 (Kennett et al., 1995). These models provide a one-dimensional velocity-depth profile of the Earth based on the global inversion of thousands of seismic-wave travel time data, in addition to some other constraints. They describe seismic velocities by refining sets of polynomial functions between specific depth intervals, defined by seismic discontinuities which are known from independent data. Both PREM and AK135 are averaged, radial velocity models of Earth and, therefore, the observed variations of $v_P$, $v_S$, and densities reflect both radial and lateral variations of mineral/chemical compositions and temperature (Figure 1.4).

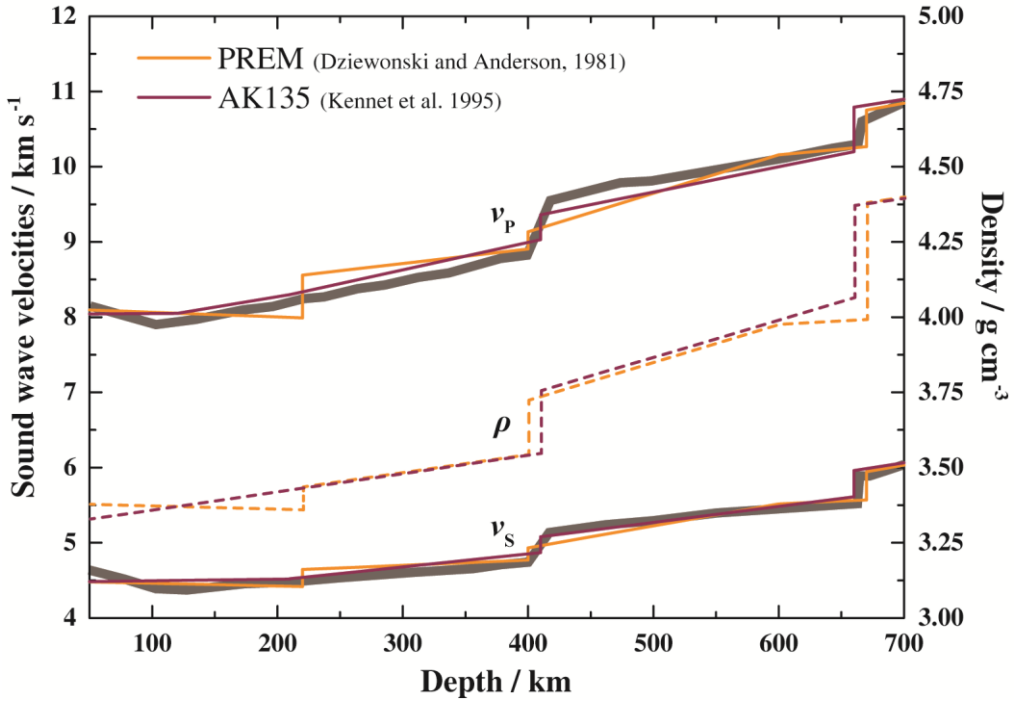


**Figure 1.4.** Seismic reference models PREM, and AK135 show $v_P$, $v_S$, and density profiles in the UM and MTZ. The superimposed grey curve indicates the range of reference models from Cammarano et al. (2005), which derive from the fitting of a pyrolitic mineral assemblage (using slightly different sets of mineral elastic properties, adjusted within the range of their relative uncertainties) against global seismic data. Adapted from Frost (2008).

Seismic discontinuities are characterized by abrupt changes in wave velocities and density and are accepted to arise both from changes in mineralogy resulting from pressure-induced equilibrium phase changes (e.g., Agee, 1998) and major compositional changes (for example, the Mohorovičić discontinuity at the base of the mafic crust and top of the ultramafic mantle, or the core-mantle boundary (CMB) at the base of the silicate mantle and top of the iron core). Such discontinuities can be directly correlated with the proportions of the transforming minerals at the discontinuity. But what is the relationship between propagating sound waves and the elastic properties of mantle minerals?

When earthquakes occur, they generate two types of sound waves, which propagate through the Earth: primary, or compressional, P-waves, referred to as $v_P$, are faster and vibrate material parallel to the direction the wave is travelling, and secondary, or shear, S-waves, referred to as $v_S$, are slower and vibrate material perpendicular to the direction the wave is travelling. When direct and reflected waves are detected by arrays of seismometer stations distributed on the globe, they reveal the velocity variation of $v_P$ and $v_S$ with depth. However, one essential element is required to relate this information into quantities of interest, such as mineralogy, temperature, and chemical composition, that is, the knowledge of the elastic properties of minerals, especially at high pressures and high temperatures, through either laboratory experiments or computational studies (e.g., Bass et al., 2008; Bass and Parise, 2008). For propagation in an elastically isotropic medium, the seismic wave velocities depend on the bulk modulus $K$, the shear modulus $G$, and the density $\rho$ of the medium through which they travel according to the following identities (Poirier, 2000):

$$v_P = \sqrt{\frac{K + 4G/3}{\rho}} \tag{1.6}$$

$$v_S = \sqrt{\frac{G}{\rho}} \tag{1.7}$$

$K$ describes the incompressibility of a material of a given density $\rho$, i.e., the resistance of a material against a change of volume, whereas $G$ describes its rigidity in response to shear stress. The important point is that the elastic moduli $K$ and $G$, and the density $\rho$, directly relate to the velocities, and vice versa.

The notion of elasticity is intimately related to the two fundamental concepts of stress (the force applied to a body) and strain (the resulting elastic deformation). The elastic properties of a material, therefore, relate stresses to the resulting strains. When seismic waves propagate

through Earth, they impose stresses and strains on its rocks and the individual constituent mineral grains. Such grains respond to seismic waves in the same way they do with respect to compression and heating as well, that is, by reversible elastic deformation (Nye, 1985). The general relationship between the stresses applied to a crystal ($\sigma_{ij}$, stress tensor) and the resulting strains ($\varepsilon_{ij}$, strain tensor) can be assumed to obey a linear relationship with the components of the elastic stiffness tensor $c_{ijkl}$ and the elastic compliance tensor $s_{ijkl}$ of the crystal (Nye, 1985):

$$\sigma_{ij} = c_{ijkl}\varepsilon_{kl} \tag{1.8}$$

$$\varepsilon_{ij} = s_{ijkl}\sigma_{kl} \tag{1.9}$$

meaning that the resulting strain is proportional to the applied stress, an example of Hook's Law. Both stress and strain are second-rank tensors and thus, the elastic stiffness and elastic compliance tensors are fourth-rank tensors containing 81 components (Nye, 1985). Although each elasticity tensor has 81 components, these are not all independent. Static equilibrium conditions (no net translations or rotations forces, that is, stress and strain tensors are symmetric) and additional constraints resulting from considerations about the change in energy per unit volume of a body resulting from a set of strains $\varepsilon_{ij}$ reduce to 21 the number of maximum independent components for the elastic stiffness and compliance tensors (Angel et al., 2009). The number of independent components is further reduced in crystal systems having high symmetries, e.g., cubic crystals, which have just three independent components (Nye, 1985).

However, working with matrices (i.e., second-rank tensors) is often preferred over the use of fourth-rank tensors and, therefore, the Voigt notation is used. In the matrix or Voigt notation, pairs of suffixes are reduced to a single suffix, which runs from 1 to 6. Terms with the same suffixes will take the single suffix (e.g., $\sigma_{11} \rightarrow \sigma_1$), while terms with differing suffixes will take a single suffix equal to 9 –i –j (e.g., $\sigma_{23} \rightarrow \sigma_4$). This rearrangement transforms the stress tensor to a vector with six components, and a similar transformation can be applied to the components of the elastic stiffness tensor (e.g., $c_{2233} \rightarrow c_{23}$ and $c_{2323} \rightarrow c_{44}$). Thus, the elastic stiffness tensor is transformed into a symmetric 6x6 matrix, enabling Equation (1.8) to be replaced with the simpler matrix equation:

$$\sigma_i = c_{ij}\varepsilon_j \tag{1.10}$$

and, with slightly different suffixes re-indexing, Equation (1.9) with:

$$\varepsilon_i = s_{ij}\sigma_j \tag{1.11}$$

where the compliance matrix is the inverse of the stiffness matrix ($s_{ij} = c_{ij}^{-1}$).

The elastic moduli of a material can be calculated in the ideal conditions of equal stress (Reuss bound, subscript R) and equal strain (Voigt bound, subscript V) from the elastic compliance ($s_{ij}$) and elastic stiffness ($c_{ij}$) as:

$$K_V = \frac{[c_{11} + c_{22} + c_{33} + 2(c_{12} + c_{13} + c_{23})]}{9} \tag{1.12}$$

$$G_V = \frac{[(c_{11} + c_{22} + c_{33}) - (c_{12} + c_{13} + c_{23}) + 3(c_{44} + c_{55} + c_{66})]}{15} \tag{1.13}$$

$$K_R = \frac{1}{[s_{11} + s_{22} + s_{33} + 2(s_{12} + s_{13} + s_{23})]} \tag{1.14}$$

$$G_R = \frac{15}{[4(s_{11} + s_{22} + s_{33}) - 4(s_{12} + s_{13} + s_{23}) + 3(s_{44} + s_{55} + s_{66})]} \tag{1.15}$$

Since rocks are aggregates composed of grains mutually interlocked, any externally applied hydrostatic pressure does not simply translate into an equal stress on each grain, but this also depends on how the neighbouring grains press on one another. Thus, for an aggregate of randomly oriented grains of a single material the values of *K* and *G* lie between two limits called the Reuss and Voigt bounds. The Reuss bound represents an ideal situation where every grain is subject to a uniform stress field equal to the imposed external stress, as grains can slip past one another as pressure is increased. Conversely, the Voigt bound assumes the strain is homogeneous throughout an aggregate of interlocked grains, regardless of their orientation (Angel et al., 2009; Watt et al., 1976).

Considering that in elastically anisotropic materials the Reuss and Voigt bounds are not equivalent, Hill (1963) proposed the arithmetic average of the two bounds to describe the elastic behaviour of crystalline aggregates of randomly oriented grains:

$$K_{VRH} = \frac{K_V + K_R}{2} \tag{1.16}$$

$$G_{VRH} = \frac{G_V + G_R}{2} \tag{1.17}$$

Such average properties are often used to compare sound wave velocities computed through mineral physics data and seismic velocities (e.g., Buchen, 2021; Criniti et al., 2021; Kurnosov et al., 2017).

Earth is composed of rocks, i.e., multiphase assemblages with different minerals having different elastic properties. Hence, averaging schemes are required to combine the elastic properties of each mineral phase into those of the multiphase assemblage. The density $\rho$ of the mineral aggregate is calculated from the densities $\rho_i$ of $n$ constituent minerals as:

$$\rho = \frac{\sum_{i=1}^{n} \rho_i \times v_i}{n} \tag{1.18}$$

where $v_i$ is the volume fraction of each mineral. Unlike density (and volumes), there is no direct way to average $K$ and $G$ of a multiphase rock, and several averaging schemes for the elastic moduli exist (e.g., Cottaar et al., 2014; Hacker and Abers, 2004; Watt et al., 1976). In most instances, for a multiphase assemblage composed of different phases with volume fractions $v_i$ and bulk and shear moduli $M_i$, the bulk and shear moduli of the assemblage are combined to the Voigt and Reuss bounds as (Watt et al., 1976):

$$M_V = \sum_{i=1}^{n} v_i \times M_i \tag{1.19}$$

$$M_R = 1 \Big/ \sum_{i=1}^{n} \frac{v_i}{M_i} \tag{1.20}$$

and then are converted to the Voigt-Reuss-Hill averages using Equations (1.16) and (1.17). The important point however is that, once the elastic moduli of the multiphase assemblage are calculated by any averaging scheme, the propagation velocities $v$ of longitudinal (P) and transverse or shear waves (S) can be computed and compared to seismic velocities.

Numerous experimental techniques for measuring the components of the elastic stiffness tensor of different types of materials are available. Considering that the pressure and temperature conditions within Earth are potentially extreme, techniques have been developed to target, or at least approach, such conditions (see the reviews by Angel et al., 2009; Bass, 2007). The components of the elastic stiffness tensor can be derived experimentally by measuring the velocities of sound waves that propagate through a single crystal along a set of different directions using light scattering techniques, such as Brillouin spectroscopy (Speziale et al., 2014) and impulsive stimulated laser scattering (ISLS, Abramson et al., 1999). Both techniques, based on inelastic scattering of light by sound waves, are routinely combined with diamond anvil cells (DACs) and have proven successful in deriving full elastic stiffness tensors of mantle minerals up to pressures of the lower mantle

and at combined high-pressure, high-temperature conditions. Sound wave velocities can be also derived by ultrasonic travel time measurements, i.e., by measuring the time needed for high-frequency acoustic waves to pass through a sample of known length. A much more advantageous method is however ultrasonic interferometry, which uses the interference between waves reflected from the two ends of the sample to determine travel times and then velocities (Li and Liebermann, 2014), and has been successfully combined with piston-cylinder or multi-anvil presses to measure the elastic properties of minerals at *P*–*T* conditions of Earth's crust and mantle. The ultrasonic resonance frequencies of a specimen with a well-defined shape (solids have natural frequencies at which they vibrate when mechanically excited) are measured in the resonant ultrasound spectroscopy (RUS, which is particularly suited for high-temperature measurements; e.g., Isaak et al., 1998) and are then inverted for the elastic properties. The development of intense third-generation synchrotron X-ray sources has resulted in the advancement of new techniques, such as inelastic X-ray scattering (INS, Burkel, 2000) and nuclear resonant inelastic X-ray scattering (NRIXS, Sturhahn, 2004). Ideally, experimentally determined sound wave velocities are combined with measurements of density (or in more precise terms, volume) at the same pressure and temperature. Thus, the techniques outlined above can be combined, and some of them routinely are, with X-ray diffraction, which is used to determine the unit-cell parameters and volume of crystalline materials.

X-ray diffraction is also among the most widely used method to investigate the elastic behaviour of minerals at non-ambient conditions, especially at high pressure with DACs (see section 2.2; Angel, 2000; Boffa Ballaran et al., 2013). As the vast majority of high-pressure experiments, DAC experiments are aimed to be carried out under hydrostatic conditions. To produce such conditions, pressure is transmitted on the sample/s hosted in a sample chamber consisting of a hole in a thin metal foil via a soft medium such as He, Ne (Klotz et al., 2009) by the small culet surfaces of two gem-quality diamonds. In the case of hydrostatic pressure, the normal stresses are all equal ($\sigma_1 = \sigma_2 = \sigma_3 = P$) and there are no shear stresses ($\sigma_4 = \sigma_5 = \sigma_6 = 0$). Hence, an infinitesimal increase in pressure $\delta P$ generates strains that can be calculated through linear elasticity theory (Equation 1.11). The volume strain of the crystal is the sum of the three normal strains ($\Delta V/V = \varepsilon_1 + \varepsilon_2 + \varepsilon_3$), which simply is the bulk modulus $K$ (in the Reuss bound), defined as a sum over some of the elements of the elastic compliance matrix of the crystal:

$$K_{TR} = -V\delta P/\delta V = \frac{1}{[s_{11} + s_{22} + s_{33} + 2(s_{12} + s_{13} + s_{23})]} \qquad (1.21)$$

equally to Equation 1.14 (see above). Diffraction however does not provide information about the shear modulus $G$.

Note the subscript $_T$ of $K_{TR}$ (termed *isothermal* bulk modulus). If a material is compressed, it heats up if the system is not allowed to dissipate this energy. There is a subtle difference between the elastic properties obtained from experiments employing time scales relatively long compared to atomic scale processes, allowing heat to escape (such as X-ray diffraction) and those being fast relative to the time required to dissipate heat from a sample (such as spectroscopy). The former elastic properties are defined as *isothermal*, and the latter (i.e., direct measurements of the elastic tensor) as *adiabatic*. The conversion between $K_T$ and $K_S$ can be performed by applying the relationship $K_{SR} = (1 + \alpha_V \gamma T)K_{TR}$, where $\alpha_V$ is the volume thermal expansion coefficient, and $\gamma$ is the thermal Grüneisen parameter (Anderson, 1995; Angel et al., 2009).

### 1.3.1 Fitting Equations of State (EoS)

Elasticity equations introduced in the previous section impose that the applied stress induces a proportional strain in a material. This is true for small strains, such as those resulting from a seismic wave passing through a rock. However, strains arising from compression and heating of the rock to pressures and temperatures in the mantle are much larger, and modifications to the elasticity equations are required to describe this behaviour. In other words, a formalism describing the large (finite) changes in volume, or density, due to large (finite) changes in pressure or temperature is required. In this sense, an equation of state (EoS) is an extension of linear elasticity. In exact terms, EoS describes how the volume or density of a material varies with changes in pressure and temperature. However, they can also be seen as a definition of the variation of $K$ and $G$ with pressure and temperature (Angel, 2000; Stixrude and Lithgow-Bertelloni, 2005a). In general terms, no absolute thermodynamic basis for specifying the correct form of the EoS of solids exists and, therefore, all EoS that have been developed are based upon several assumptions, the validity of which can only be judged in terms of whether the derived EoS reproduces experimental data for volume or elasticity.

Isothermal EoS are usually parameterized in terms of the values of the bulk modulus $K$ and its pressure derivatives, $K' = -\partial K/\partial P$ and $K'' = -\partial^2 K/\partial P^2$, evaluated at zero pressure (or, almost equivalent, at room-pressure). The isothermal EoS which provides the best fit to experimental $P$–$V$ data, and the best match to independent measurements of the compliance tensors is the Birch-Murnaghan (BM) EoS (Angel, 2000; Angel et al., 2014b). This 'finite strain' EoS is derived from the assumption that the strain energy of a solid undergoing

compression can be expressed as a Taylor series in the finite Eulerian strain, $f_E = [(V_0/V)^{2/3} - 1]/2$, where $V_0$ is the volume of the crystal at the reference state, and its fourth-order expression can be written as:

$$P = 3K_0 f_E(1+2f_E)^{\frac{5}{2}}(1+\frac{3}{2}(K'-4)f_E + \frac{3}{2}(K_0K'' + (K'-4)(K'-3) + \frac{35}{9}){f_E}^2) \quad (1.22)$$

*P–V* datasets can be adequately fitted by 2nd-, 3rd-, and 4th-order BM EoS, depending on their curvature. The 2nd-order truncation of Equation (1.22) requires the coefficient $f_E$ to be equal to zero, which imposes the first pressure derivative *K*' having the fixed value of 4. The 3rd-order truncation sets the coefficient $f_E^2$ to zero, yielding a three-parameter EoS ($V_0$, $K_0$, and *K*') with an implied value of *K*''. A visual diagnostic tool in discriminating whether higher order terms such as *K*' and *K*'' might be significant in an EoS is provided by the $f_E$-$F_E$ plot. In the case of the BM EoS, a 'normalised stress' is defined as $F_E = P/3f_E(1+2f_E)^{5/2}$, where $f_E$ is the finite Eulerian strain defined above. If the *P–V* data are transformed into $f_E$ (x-axis) and $F_E$ (y-axis) and plotted, a direct indication of the compressional behaviour can be obtained (Angel, 2000). If data points lie on (i) a horizontal line, the data can be fitted with a BM2 EoS (=2nd-order Birch-Murnaghan), (ii) an inclined straight line requires a BM3 EoS, whereas (iii) 4th-order BM EoS is required when data fall on a parabolic curve.

In the case of *P–V–T* datasets, the biggest challenge in EoS calculations is to adequately treat the cross derivatives of the elastic parameters with respect to *P* and *T*, that is, for example, $\partial K/\partial T$ (bulk modulus change with *T*) or $\partial\alpha/\partial P$ (thermal expansion coefficient change with *P*). In this context, there are two possible approaches: one based on isothermal-type models at high temperatures, and the other based on the thermal-pressure models (cf. Angel et al., 2018), the fundamental difference being the path in *P–T* space upon which volume is calculated (Figure 1.5).

Isothermal-type models at high temperatures describe the thermal expansion at room pressure and the variation with temperature of *K* and *K*'. The volume at high *P–T* is then calculated using $V(P = 0, T)$, $K_{TR}(P = 0, T)$, and its pressure derivatives at high *T* and room *P* in an isothermal EoS. Thermal pressure models, such as Holland-Powell and Mie-Grüneisen-Debye thermal-pressure EoS, calculate $V(P, T)$ starting with an isothermal compression to the required volume at $T_0$, followed by a path along an isochor (that is, by heating the material at constant *V*, which generates an additional pressure, *P*th).

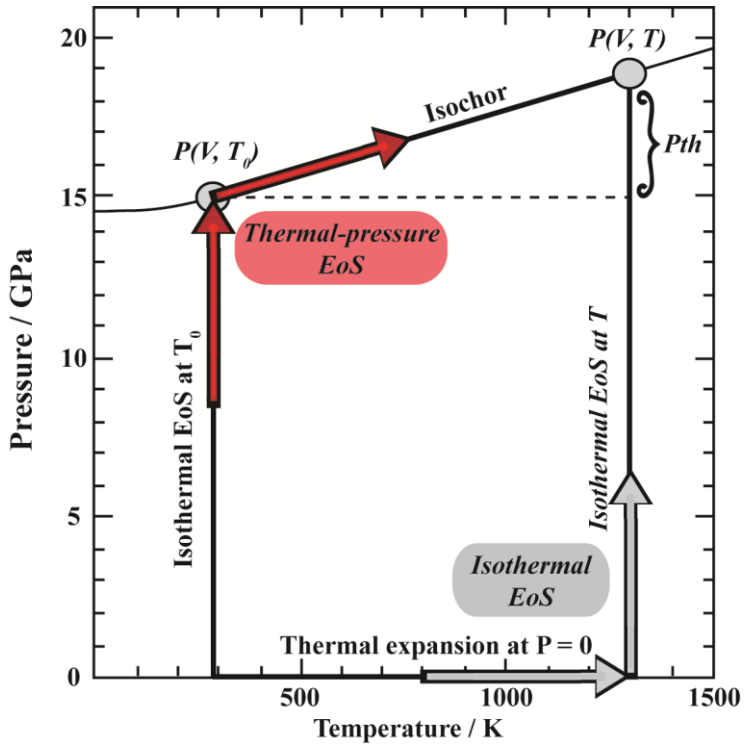


**Figure 1.5.** *P–T* diagram showing the two different paths used in calculating the volume *V* in isothermal-type models at high temperature (grey arrows) and thermal-pressure models (red arrows). *P*th corresponds to the thermal pressure (see text). Redrawn from Angel et al. (2018)

A generalization of finite-strain theory for anisotropic materials and strains has been presented by Stixrude and Lithgow-Bertelloni (2005), in which physical properties, including pressure and elastic stiffnesses ($c_{ij}$, $K_S$, $G$) can be described as a function of volume and temperature. The self-consistent thermodynamic model of Stixrude and Lithgow-Bertelloni (2005) combines finite strain theory with Mie-Grüneisen EoS with a quasi-harmonic Debye model for thermal contributions to calculate pressure and elastic properties. The 3rd-order expression for the adiabatic elastic stiffness tensor components is given by:

$$\begin{aligned} c_{ijkl} = {} & (1+2f)^{\frac{5}{2}}\{c_{ijkl,0} + \left(3K_0 c'_{ijkl,0} - 5c_{ijkl,0}\right)f \\ & + [6K_0 c'_{ijkl,0} - 14c_{ijkl,0} - \frac{3}{2}K_0\delta^{ij}_{kl}(3K'_0 - 16)]f^2\} \\ & + \left[\gamma_{ij}\gamma_{kl} + \frac{1}{2}\left(\gamma_{ij}\delta_{kl} + \gamma_{kl}\delta_{ij}\right) - \eta_{ijkl}\right]\rho\Delta U_q - \gamma_{ij}\gamma_{kl}\rho\Delta(C_V T) \end{aligned} \quad (1.23)$$

where $c_{ijkl,0}$ is the elastic stiffness coefficient at ambient conditions, $c'_{ijkl,0}$ its pressure derivative, and $\delta^{ij}_{kl} = -\delta_{ij}\delta_{kl} - \delta_{il}\delta j_k - \delta_{jl}\delta_{ik}$. The thermal contribution is expressed in line 3 of Equation (1.23) and includes the components of the Grüneisen tensor $\gamma_{ij}$ and their strain derivatives $\eta_{ijkl}$, the thermal part of the internal energy $U_Q$ and the isochoric heat capacity

$C_V$ (see Stixrude and Lithgow-Bertelloni, 2005). The 3rd-order expressions for the elastic moduli are given by:

$$K = (1+2f)^{\frac{5}{2}}\left[K_0 + (3K_0K_0' - 5K_0)f + \frac{27}{2}(K_0K_0' - 4K_0)f^2\right] + (\gamma + 1 + q)\gamma\rho\Delta U_q - \gamma^2\rho\Delta(C_V T) \quad (1.24)$$

$$G = (1+2f)^{\frac{5}{2}}\left[G_0 + (3K_0G_0' - 5G_0)f + \left(6K_0G_0' - 24K_0 - 14G_0 + \frac{9}{2}K_0K_0'\right)f^2\right] - \eta_S\rho\Delta U_q \quad (1.25)$$

The thermal contribution for $K$ and $G$ is expressed in lines 2 of Equations (1.24) and (1.25), respectively, where $q$ is typically taken as constant and $\eta_S$ is the shear strain derivative of $\gamma$ (Stixrude and Lithgow-Bertelloni, 2005a).

It is known that the elastic moduli of mantle minerals, and their pressure and temperature derivatives, may change in response to crystal-chemical substitutions, such as Fe for Mg and Al for Si. Among these substitutions, much attention has been drawn to hydrogen (or in more familiar terms, water) incorporation in the crystal structure of NAMs – $n\mathrm{H}^+ \leftrightarrow \square$, where $\square$ indicates a cation vacancy – which has been shown to have potentially massive effects on the elasticity of nominally anhydrous minerals (NAMs) (e.g., Jacobsen, 2006; Mao and Li, 2016). Therefore, the next section aims to provide a general overview of the various evidence of the presence of water in Earth's mantle, and then discuss the effects of water incorporation on the physical properties of NAMs, with emphasis given to the elastic properties.

## 1.4 Evidence of the presence of water in Earth's upper mantle

The hallmark of our 'blue' planet is copious surface water, mainly stored in oceans, but also in ice sheets, lakes, rivers, etc., whose presence is perhaps the key element for Earth's climate and habitability and has important bearings on Earth's geological history. Nonetheless, surface water is only a rather small fraction of Earth's water budget. Indeed, the notion that magma coming from the mantle contain small amounts of water (e.g., Michael, 1988) set the basis for the inference that Earth's mantle has to be slightly hydrated, at least. However, most of the mantle consists of NAMs, such as olivine, pyroxenes, garnet, etc., and so it was initially thought that water resided in hydrous minerals, such as amphiboles. Subsequently, the pioneering work of Bell and Rossman (1992) showed that the hosts for water in Earth's mantle are chiefly the NAMs themselves, which accommodate hydrogen ions as trace

defects. The modern view of the deep-Earth water cycle is strongly coupled to plate tectonics, subducting slabs being the main carrier of water to Earth's mantle, whereas degassing from volcanism in mid-oceanic ridges and arcs being the major source of water loss (see Hirschmann and Kohlstedt, 2012, for an introductory reading).

Estimates of Earth's mantle water budget may be inferred from (i) geochemical arguments, i.e., by mass-balance calculations involving the water contents of the different reservoirs and their respective mass fractions, (ii) from the water concentration of MORBs, i.e., knowing the melt fraction, and the partition coefficient of water between the solid and the liquid and by assuming batch melting, (iii) from geophysical observation and (iv) from mantle xenoliths (see Bolfan-Casanova, 2005). Here, a special emphasis will be given to point (iv), that is, the water concentrations of NAMs.

The occurrence of water in NAMs is closely related to the presence of hydroxyl-bearing ($OH^-$) point defects in their crystal structure, where hydrogen is bonded to lattice oxygen and is charge-balanced by cation vacancies. A simplified sketch of the substitution mechanisms of H in olivine is provided in Figure 1.6 and more details will be found in Chapter 5, where the effect of water incorporation on olivine elastic properties will be presented.

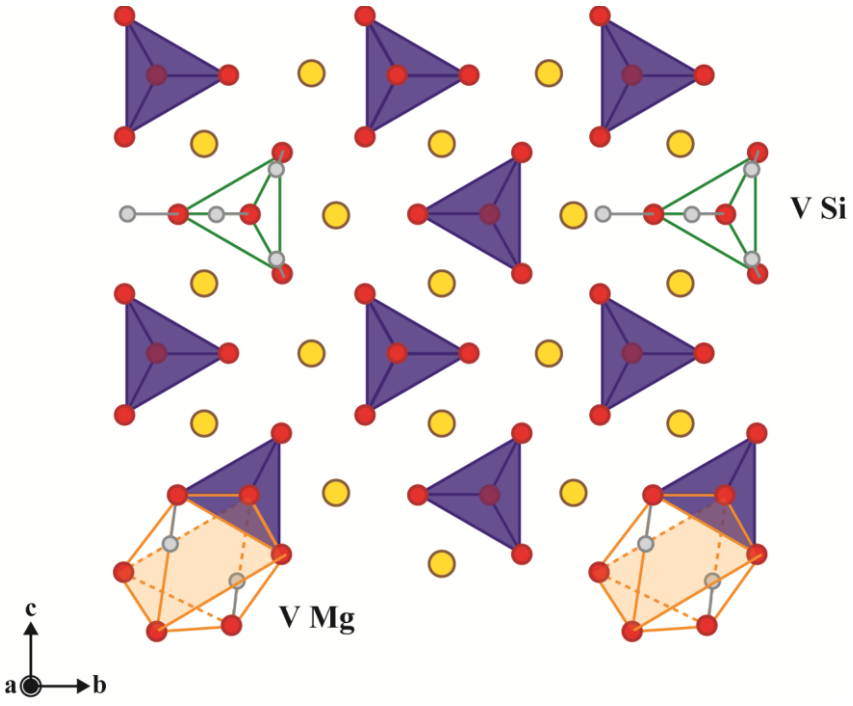


**Figure 1.6.** Simplified sketch of the crystal structure of $Mg_2SiO_4$ forsterite and hydrogen substitution mechanisms. $Si^{4+}$ ions (not shown) are hosted in tetrahedral sites (blue), $Mg^{2+}$ ions (yellow) are hosted in octahedral sites (orange, only the vacant octahedral sites are shown here), and $O^{2-}$ ions (red) occupy the corners. Hydrogen ions (grey) can be both hosted at a vacant Si site (V Si), where four $H^+$ ions can substitute for a single $Si^{4+}$ ion, or at a vacant Mg site (V Mg), where two $H^+$ ions can substitute for a single $Mg^{2+}$ ion. Redrawn from Hirschmann and Kohlstedt, 2012.

Many reviews of water in NAMs are available in the literature (e.g., Bell and Rossman, 1992; Beran and Libowitzky, 2006; Bonadiman et al., 2009; Peslier, 2010; Skogby, 2006; Xia et al., 2010) and confirmed that essentially all NAMs contain substantial amounts of water. Pyroxenes have been shown to carry the largest amount of water among the major UM minerals and are considered major hosts for water in the mantle, as their water concentrations range from hundreds up to ~1000 ppm $H_2O$. Besides pyroxenes, the mineral structures of olivine and garnet (plus other accessory minerals), although at comparatively low extents respect to pyroxenes, offer other important storage sites for water in Earth's mantle, typically in the range of 100–200 ppm. However, various caveats have to be considered when dealing with water concentrations in NAMs, some of which are more evident while others are subtler. Because they are sampled at relatively shallow depths within the lithosphere, it is unlikely that xenoliths are representative of the convective UM with respect to their water content, but rather they may provide a minimum value for the water content that can be incorporated in natural mantle phases. Nonetheless, whether the water concentrations recorded in xenoliths are representative of the conditions in the UM, or if their original hydrogen contents were reset during their ascent to the surface, is still a fundamental question. Kinetic data indicate that hydrogen diffusion in mantle minerals at magmatic temperatures occurs at much faster rates than other defects in silicates (e.g., Kohlstedt and Mackwell, 1998), and therefore any H loss may occur without substantial compositional change of the host mineral and in just a few hours during ascent from depths. Although diffusion rates in olivine and pyroxenes are of the same order of magnitude, H loss particularly affects olivine, especially in the case of olivines from xenoliths found in alkali basalts, which commonly show H diffusion patterns, whereas the fast ascent of kimberlite magmas should prevent dehydration in olivine during xenolith transport (Demouchy et al., 2006; Peslier, 2010; Peslier et al., 2008). Despite all efforts, we are not fully aware of the actual abundance of water in NAMs, and laboratory experiments conducted at relevant UM conditions have demonstrated that NAMs can host gigantic amounts of water compared to natural samples, as high as 10.000 ppm $H_2O$ (i.e., ~1 wt.%) in olivine (Smyth et al., 2006) or 8.000 ppm $H_2O$ in orthopyroxene (Smyth et al., 2007). These values are expressed as the maximum solubilities of water observed in experiments and, therefore, do not imply that these amounts of water are actually found in natural NAMs. For example, the water storage capacity of olivine under pressures and temperatures relevant to the deep UM is expected to be around 0.2–0.5 wt.% $H_2O$, and not as high as 1 wt.% (Férot and Bolfan-Casanova, 2012; Hirschmann et al., 2005; Mosenfelder, 2006).

Experiments have shown wadsleyite and ringwoodite to be potential hosts of massive quantities of water (up to ~3 wt.%), and the discovery of ringwoodite inclusion with ~1.4 wt.% $H_2O$ in a natural diamond (Pearson et al., 2014) confirmed the experimental predictions, corroborating the hypothesis of MTZ being at least partly hydrated. Furthermore, the occurrence of a polyphase inclusion in a natural diamond consisting of ringwoodite together with lower-mantle minerals and hydrous phases, whose origin was placed at the boundary between the MTZ and the lower mantle (660-km discontinuity), revealed that the peridotitic composition and hydrous conditions may extend across the MTZ and into the lower mantle (Gu et al., 2022).

Much of the more recent interest has been focused on investigating how NAMs respond to hydrogen incorporation, beyond quantifying the amounts of water they can store. Even if water is present in tiny quantities, it has significant effects on the physical properties of minerals and rocks of the mantle, and so upon its structure and dynamics.

### 1.4.1 Effects of water incorporation on the physical properties of NAMs

The presence of hydroxyl-bearing ($OH^-$) point defects in the crystal structure of NAMs has been shown to affect substantially their physical properties. These include atomic diffusivity (e.g., Costa and Chakraborty, 2008; Kubo et al., 2004), electrical conductivity (e.g., Poe et al., 2010; Yoshino et al., 2006), thermal conductivity (e.g., Chang et al., 2017), rheology (e.g., Jung and Karato, 2001; Mei and Kohlstedt, 2000a, 2000b) and melting (e.g., Inoue, 1994; Ni et al., 2016). The reader is referred to Zhang and Xia (2021) for a review of the influence of water on the physical properties of olivine and its high-pressure polymorphs wadsleyite and ringwoodite.

The diffusion rates of all ions increase dramatically under hydrous conditions because the incorporation of water rises the concentrations of vacancies or interstitial defects, to which the enhancements of diffusion rates are generally attributed. Electrical conductivity is very sensitive to water (and temperature) and is a suitable geophysical remote sensing technique for investigating the water distribution within Earth's interior. Experiments have shown that the electrical conductivity systematically increases with increasing water concentration, this dependence is taken as evidence of $H^+$ ions being the primary charge carriers under wet conditions. The thermal conductivity of mantle minerals is a critical parameter controlling the heat transfer within Earth's interior (for example, the homogenization of temperature heterogeneities deriving from the subduction of a cold slab), and experiments have shown that the thermal conductivity of olivine is reduced under hydrous conditions. Of particular importance to mantle convection is the strength of olivine and the other NAMs, which

systematically decrease as H concentration increases, the implication being that the viscosity of the mantle will vary as a function of the geochemical environment, and the low viscosity of the asthenosphere, where mantle convection and much of the associated deformation occur, is caused by the higher water concentration relative to the dry, highly viscous lithosphere. Water may also influence the viscosity of the mantle in terms of partial melting of mantle rocks, which is facilitated under hydrous (and carbonated) conditions and has been shown to reduce their viscosity.

Velocities of seismic waves are perhaps among the best constrained physical parameters of Earth's interior and, therefore, if the relation between seismic wave velocity and water content is known, variations in water contents in Earth's interior can be inferred from seismological observations. There are various mechanisms through which water affects seismic wave velocities, including (i) the change of the ionic bond strength induced by the incorporation of hydrogen, (ii) the enhancement of anelasticity of NAMs, in response to the higher mobilities of point defects, dislocations, and grain boundaries, (iii) the enhancement of seismic anisotropy, in response to the development of preferred orientation fabrics (e.g., Jacobsen, 2006; Karato, 2003, 1995). Although the enhancement of anelasticity has been shown to lower seismic wave velocities, the most obvious effect of water on seismic wave propagation is the reduction of seismic wave velocities due to the softening of the chemical bonding induced by hydrogen. In this context, it is necessary to know quantitatively the effects of water on the elastic moduli of mantle minerals, which are related to seismic velocities (cf. section 1.3), and their pressure and temperature derivatives for a more direct comparison with seismological observations. Extensive experimental work has been conducted to investigate the influence of water incorporation on sound wave velocities using high-frequency techniques, such as Brillouin spectroscopy (e.g., Buchen et al., 2018; Fan et al., 2019; Hou et al., 2022; Jacobsen et al., 2008; Mans et al., 2019; Mao et al., 2010, 2008a). High-pressure Brillouin studies provide very accurate $K_S$, $G$, and pressure derivatives $K'$'s and $G'$ compared to X-ray diffraction, where $K'_T$ is a second-order fitting parameter and no information about the shear modulus $G$ and its derivative $G'$ can be provided.

In general terms, the elastic moduli $K$ and $G$ (as well as the elastic constants $c_{ij}$) of hydrous NAMs decrease with increasing water content while, on the other hand, the pressure derivatives of the elastic moduli $K'$ and $G'$ show an opposite trend due to the higher compressibility of the lattice vacancies (Jacobsen, 2006). The effects of hydration on thermal expansion coefficients have been less explored because hydrous NAMs decompose or dehydrate when not under confining pressure. Results showed that water has either a negligible or slightly positive effect on the volume thermal expansivity of olivine and its

high-pressure polymorphs (Inoue et al., 2004; Ye et al., 2009). Despite all the studies carried out in these last two decades, the magnitude of the water effect on seismic velocities is still debated. The reason why is that the difference between anhydrous and hydrous velocities is progressively lifted at higher pressures, due to the larger pressure derivatives of hydrous samples compared to those of the corresponding anhydrous phases. The effect of water on the sound wave velocities of mantle minerals has potentially major implications for petrological models of the Earth's mantle. Seismic discontinuities in the Earth's mantle (especially those bounding the MTZ between 410 and 670 km depth) can be directly correlated with the proportions of the transforming minerals at the discontinuity. Attempts to constrain the bulk olivine content in the UM by comparing sound wave velocities contrasts of olivine and wadsleyite calculated from mineral physics information to seismically observed velocity contrasts at the 410-km discontinuity concluded that a pyrolitic mantle composition cannot explain the detected velocity jumps (e.g., Thio et al., 2016; Wang et al., 2014), which can be matched with a deep UM being less enriched in olivine than the pyrolite model. However, based on the reduction of the sound wave velocities of wadsleyite due to the incorporation of water (Mao et al., 2008a, 2008b), it was proposed that water dissolved in olivine and wadsleyite may reconcile the pyrolite model with seismological observations. Overall, several studies showed that the effects of water on the sound wave velocities in mantle minerals, when evaluated at relevant mantle conditions, are minor or negligible for water contents of less than ~0.1 wt.%. Therefore, to determine whether lateral variations of seismic velocities within the UM and/or the MTZ are a suitable proxy to infer the hydration state of these mantle domains and whether a hydrated pyrolitic transition zone may be invoked, it is important to consider the numerous experimental data on water solubility in NAMs (e.g., Férot and Bolfan-Casanova, 2012; Rauch and Keppler, 2002; Withers et al., 1998) and to study synthetic samples with a realistic water content expected under relevant mantle conditions. In this context, Chapter 5 will present the first assessment of the full elastic tensor of Fo90 olivine with ~0.20 wt.% $H_2O$, obtained by simultaneous high-pressure Brillouin and single-crystal X-ray diffraction experiments, and will investigate the difference between anhydrous and hydrous velocities of Fo90 under relevant mantle conditions.

# References


Abramson, E.H., Brown, J.M., Slutsky, L.J., 1999. Applications of impulsive stimulated scattering in the Earth and planetary sciences. Annu. Rev. Phys. Chem. 50, 279–313.

Agee, C.B., 1998. Phase transformations and seismic structure in the upper mantle and transition zone, in: Ultrahigh Pressure Mineralogy. De Gruyter, pp. 165–204.

Akaogi, M., Ito, E., Navrotsky, A., 1989. Olivine-modified spinel-spinel transitions in the system Mg 2 SiO 4 -Fe 2 SiO 4 : Calorimetric measurements, thermochemical calculation, and geophysical application. J. Geophys. Res. Solid Earth 94, 15671–15685.

Anderson, D.L., 2006. Speculations on the nature and cause of mantle heterogeneity. Tectonophysics 416, 7–22.

Anderson, D.L., 1995. Lithosphere, asthenosphere, and perisphere. Rev. Geophys. 33, 125.

Anderson, O.L., 1995. Equations of state of solids for geophysics and ceramic science, Oxford Monographs on Geology and Geophysics.

Angel, R.J., 2000. Equations of State. Rev. Mineral. Geochemistry 41, 35–59.

Angel, R.J., Mazzucchelli, M.L., Alvaro, M., Nimis, P., Nestola, F., 2014a. Geobarometry from host-inclusion systems : The role of elastic relaxation. Am. Mineral. 99, 2146–2149.

Angel, R.J., Alvaro, M., Gonzalez-Platas, J., 2014b. EosFit7c and a Fortran module (library) for equation of state calculations. Zeitschrift für Krist. - Cryst. Mater. 229, 405–419.

Angel, R.J., Alvaro, M., Nestola, F., 2018. 40 years of mineral elasticity: a critical review and a new parameterisation of equations of state for mantle olivines and diamond inclusions. Phys. Chem. Miner. 45, 95–113.

Angel, R.J., Jackson, J.M., Reichmann, H.J., Speziale, S., 2009. Elasticity measurements on minerals: a review. Eur. J. Mineral. 21, 525–550.

Arai, S., 1994. Characterization of spinel peridotites by olivine-spinel compositional relationships: Review and interpretation. Chem. Geol. 113, 191–204.

Aulbach, S., Griffin, W.L., Pearson, N.J., O'Reilly, S.Y., 2013. Nature and timing of metasomatism in the stratified mantle lithosphere beneath the central Slave craton (Canada). Chem. Geol. 352, 153–169. https://doi.org/10.1016/j.chemgeo.2013.05.037

Bass, J.D., 2007. Theory and Practice – Techniques for Measuring High P/T Elasticity, in: Treatise on Geophysics. Elsevier, pp. 269–291.

Bass, J.D., Anderson, D.L., 1984. Composition of the upper mantle: Geophysical tests of two petrological models. Geophys. Res. Lett. 11, 229–232.

Bass, J.D., Parise, J.B., 2008. Deep Earth and Recent Developments in Mineral Physics. Elements 4, 157–163.

Bass, J.D., Sinogeikin, S. V., Li, B., 2008. Elastic Properties of Minerals: A Key for Understanding the Composition and Temperature of Earth's Interior. Elements 4, 165–170.

Bell, D.R., Rossman, G.R., 1992. Water in Earth's Mantle: The Role of Nominally Anhydrous Minerals. Science (80-. ). 255, 1391–1397.

Bénard, A., Woodland, A.B., Arculus, R.J., Nebel, O., McAlpine, S.R.B., 2018. Variation in sub-arc mantle oxygen fugacity during partial melting recorded in refractory peridotite xenoliths from the West Bismarck Arc. Chem. Geol. 486, 16–30.

Beran, A., Libowitzky, E., 2006. Water in natural mantle minerals II: Olivine, garnet and accessory minerals, in: Reviews in Mineralogy and Geochemistry 62: Water in Nominally Anhydrous Minerals. pp. 169–192.

Boffa Ballaran, T., Kurnosov, A., Trots, D., 2013. Single-crystal X-ray diffraction at extreme conditions: a review. High Press. Res. 33, 453–465.

Bolfan-Casanova, N., 2005. Water in the Earth's mantle. Mineral. Mag. 69, 229–257.

Bonadiman, C., Hao, Y., Coltorti, M., Dallai, L., Faccini, B., Huang, Y.X., 2009. Water contents of pyroxenes in intraplate lithospheric mantle. Eur. J. Mineral. 21, 637–647.

Braun, M.G., Kelemen, P.B., 2002. Dunite distribution in the Oman Ophiolite: Implications for melt flux through porous dunite conduits. Geochemistry, Geophys. Geosystems 3, 1–21.

Buchen, J., 2021. Seismic Wave Velocities in Earth's Mantle from Mineral Elasticity, in: Mantle Convection and Surface Expressions. pp. 51–95.
Buchen, J., Marquardt, H., Speziale, S., Kawazoe, T., Boffa Ballaran, T., Kurnosov, A., 2018. High-pressure single-crystal elasticity of wadsleyite and the seismic signature of water in the shallow transition zone. Earth Planet. Sci. Lett. 498, 77–87.
Burkel, E., 2000. Phonon spectroscopy by inelastic x-ray scattering. Reports Prog. Phys. 63, 171–232.
Cammarano, F., Goes, S., Deuss, A., Giardini, D., 2005. Is a pyrolitic adiabatic mantle compatible with seismic data? Earth Planet. Sci. Lett. 232, 227–243. https://doi.org/10.1016/j.epsl.2005.01.031
Carlson, R.W., Pearson, D.G., James, D.E., 2005. Physical, chemical, and chronological characteristics of continental mantle. Rev. Geophys. 43, 1–24.
Casetta, F., Rizzo, A.L., Faccini, B., Ntaflos, T., Abart, R., Lanzafame, G., Faccincani, L., Mancini, L., Giacomoni, P.P., Coltorti, M., 2022. CO2 storage in the Antarctica Sub-Continental Lithospheric Mantle as revealed by intra- and inter-granular fluids. Lithos 416–417, 106643.
Chang, Y.-Y., Hsieh, W.-P., Tan, E., Chen, J., 2017. Hydration-reduced lattice thermal conductivity of olivine in Earth's upper mantle. Proc. Natl. Acad. Sci. 114, 4078–4081.
Coltorti, M., Bonadiman, C., Casetta, F., Faccini, B., Giacomoni, P.P., Pelorosso, B., Perinelli, C., 2021. Nature and evolution of the northern Victoria Land lithospheric mantle (Antarctica) as revealed by ultramafic xenoliths. Geol. Soc. London, Mem. 56, M56-2020–11.
Coltorti, M., Bonadiman, C., Hinton, R.W., Siena, F., Upton, B.G.J., 1999. Carbonatite Metasomatism of the Oceanic Upper Mantle: Evidence from Clinopyroxenes and Glasses in Ultramafic Xenoliths of Grande Comore, Indian Ocean. J. Petrol. 40, 133–165.
Connolly, J.A.D., 2009. The geodynamic equation of state: What and how. Geochemistry, Geophys. Geosystems 10, Q10014.
Costa, F., Chakraborty, S., 2008. The effect of water on Si and O diffusion rates in olivine and implications for transport properties and processes in the upper mantle. Phys. Earth Planet. Inter. 166, 11–29.
Cottaar, S., Heister, T., Rose, I., Unterborn, C., 2014. BurnMan: A lower mantle mineral physics toolkit. Geochemistry, Geophys. Geosystems 15, 1164–1179.
Criniti, G., Kurnosov, A., Boffa Ballaran, T., Frost, D.J., 2021. Single-Crystal Elasticity of MgSiO 3 Bridgmanite to Mid-Lower Mantle Pressure. J. Geophys. Res. Solid Earth 126.
Dawson, J.B., 2002. Metasomatism and Partial Melting in Upper-Mantle Peridotite Xenoliths from the Lashaine Volcano, Northern Tanzania. J. Petrol. 43, 1749–1777.
Demouchy, S., Jacobsen, S.D., Gaillard, F., Stern, C.R., 2006. Rapid magma ascent recorded by water diffusion profiles in mantle olivine. Geology 34, 429.
Dziewonski, A.M., Anderson, D.L., 1981. Preliminary reference Earth model. Phys. Earth Planet. Inter. 25, 297–356.
Faccini, B., Rizzo, A.L., Bonadiman, C., Ntaflos, T., Seghedi, I., Grégoire, M., Ferretti, G., Coltorti, M., 2020. Subduction-related melt refertilisation and alkaline metasomatism in the Eastern Transylvanian Basin lithospheric mantle: Evidence from mineral chemistry and noble gases in fluid inclusions. Lithos 364–365, 105516.
Fan, D., Xu, J., Lu, C., Tkachev, S.N., Li, B., Ye, Z., Huang, S., Prakapenka, V.B., Zhou, W., 2019. Elasticity of single-crystal low water content hydrous pyrope at high-pressure and high-temperature conditions. Am. Mineral. 104, 1022–1031.
Férot, A., Bolfan-Casanova, N., 2012. Water storage capacity in olivine and pyroxene to 14GPa: Implications for the water content of the Earth's upper mantle and nature of seismic discontinuities. Earth Planet. Sci. Lett. 349–350, 218–230.
Fischer, K.M., Ford, H.A., Abt, D.L., Rychert, C.A., 2010. The Lithosphere-Asthenosphere Boundary. Annu. Rev. Earth Planet. Sci. 38, 551–575.

Frost, D.J., 2008. The Upper Mantle and Transition Zone. Elements 4, 171–176.
Frost, D.J., McCammon, C.A., 2008. The Redox State of earth's mantle. Annu. Rev. Earth Planet. Sci. 36, 389–420.
Fumagalli, P., Klemme, S., 2015. Mineralogy of the Earth: Phase Transitions and Mineralogy of the Upper Mantle, in: Treatise on Geophysics. Elsevier, pp. 7–31.
Ghiorso, M.S., Sack, R.O., 1995. Chemical mass transfer in magmatic processes IV. A revised and internally consistent thermodynamic model for the interpolation and extrapolation of liquid-solid equilibria in magmatic systems at elevated temperatures and pressures. Contrib. to Mineral. Petrol. 119, 197–212.
Gu, T., Pamato, M.G., Novella, D., Alvaro, M., Fournelle, J., Brenker, F.E., Wang, W., Nestola, F., 2022. Hydrous peridotitic fragments of Earth's mantle 660 km discontinuity sampled by a diamond. Nat. Geosci. 15, 950–954.
Gurney, J.J., Helmstaedt, H.H., Richardson, S.H., Shirey, S.B., 2010. Diamonds through Time. Econ. Geol. 105, 689–712.
Hacker, B.R., Abers, G.A., 2004. Subduction Factory 3: An Excel worksheet and macro for calculating the densities, seismic wave speeds, and H 2 O contents of minerals and rocks at pressure and temperature. Geochemistry, Geophys. Geosystems 5, n/a-n/a.
Harte, B., 2010. Diamond formation in the deep mantle: the record of mineral inclusions and their distribution in relation to mantle dehydration zones. Mineral. Mag. 74, 189–215.
Hasterok, D., Chapman, D.S., 2011. Heat production and geotherms for the continental lithosphere. Earth Planet. Sci. Lett. 307, 59–70.
Hill, R., 1963. Elastic properties of reinforced solids: Some theoretical principles. J. Mech. Phys. Solids 11, 357–372.
Hirschmann, M., Kohlstedt, D., 2012. Water in Earth's mantle. Phys. Today 65, 40–45.
Hirschmann, M.M., Aubaud, C., Withers, A.C., 2005. Storage capacity of H2O in nominally anhydrous minerals in the upper mantle. Earth Planet. Sci. Lett. 236, 167–181.
Hou, M., Zhou, W.-Y., Hao, M., Hua, F.T.-S., Kung, J., Zhang, D., Dera, P.K., Zhang, J.S., 2022. Effect of structural water on the elasticity of orthopyroxene. Am. Mineral. 107, 703–708.
Inoue, T., 1994. Effect of water on melting phase relations and melt composition in the system Mg2SiO4-MgSiO3-H2O up to 15 GPa. Phys. Earth Planet. Inter. 85, 237–263.
Inoue, T., Tanimoto, Y., Irifune, T., Suzuki, T., Fukui, H., Ohtaka, O., 2004. Thermal expansion of wadsleyite, ringwoodite, hydrous wadsleyite and hydrous ringwoodite. Phys. Earth Planet. Inter. 143–144, 279–290.
Ionov, D.A., Doucet, L.S., Ashchepkov, I. V, 2010. Composition of the Lithospheric Mantle in the Siberian Craton: New Constraints from Fresh Peridotites in the Udachnaya-East Kimberlite. J. Petrol. 51, 2177–2210.
Isaak, D.G., Carnes, J.D., Anderson, O.L., Cynn, H., Hake, E., 1998. Elasticity of TiO 2 rutile to 1800 K. Phys. Chem. Miner. 26, 31–43.
Jacobsen, S.D., 2006. Effect of water on the equation of state of nominally anhydrous minerals, in: Reviews in Mineralogy and Geochemistry 62: Water in Nominally Anhydrous Minerals. pp. 321–342.
Jacobsen, S.D., Jiang, F., Mao, Z., Duffy, T.S., Smyth, J.R., Holl, C.M., Frost, D.J., 2008. Effects of hydration on the elastic properties of olivine. Geophys. Res. Lett. 35, L14303.
Jung, H., Karato, S.-I., 2001. Effects of water on dynamically recrystallized grain-size of olivine. J. Struct. Geol. 23, 1337–1344.
Kaminsky, F., 2012. Mineralogy of the lower mantle : A review of ' super-deep' mineral inclusions in diamond. Earth Sci. Rev. 110, 127–147.
Karato, S., 2003. Mapping water content in the upper mantle, in: Geophysical Monograph Series. pp. 135–152.
Karato, S., 1995. Effects of Water on Seismic Wave Velocities in the Upper Mantle. Proc. Japan Acad. Ser. B 71, 61–66.

Katsura, T., Ito, E., 1989. The system Mg 2 SiO 4 -Fe 2 SiO 4 at high pressures and temperatures: Precise determination of stabilities of olivine, modified spinel, and spinel. J. Geophys. Res. Solid Earth 94, 15663–15670.
Katsura, T., Yamada, H., Nishikawa, O., Song, M., Kubo, A., Shinmei, T., Yokoshi, S., Aizawa, Y., Yoshino, T., Walter, M.J., Ito, E., Funakoshi, K., 2004. Olivine-wadsleyite transition in the system (Mg,Fe) 2 SiO 4. J. Geophys. Res. Solid Earth 109, 1–12.
Kennett, B.L.N., Engdahl, E.R., Buland, R., 1995. Constraints on seismic velocities in the Earth from traveltimes. Geophys. J. Int. 122, 108–124.
Klotz, S., Chervin, J.-C., Munsch, P., Le Marchand, G., 2009. Hydrostatic limits of 11 pressure transmitting media. J. Phys. D. Appl. Phys. 42, 075413.
Kohlstedt, D.L., Mackwell, S.J., 1998. Diffusion of hydrogen and intrinsic point defects in olivine. Zeitschrift fur Phys. Chemie 207, 147–162.
Kubo, T., Shimojuku, A., Ohtani, E., 2004. Mg-Fe interdiffusion rates in wadsleyite and the diffusivity jump at the 410-km discontinuity. Phys. Chem. Miner. 31, 456–464.
Kurnosov, A., Marquardt, H., Frost, D.J., Ballaran, T.B., Ziberna, L., 2017. Evidence for a Fe3+-rich pyrolitic lower mantle from (Al,Fe)-bearing bridgmanite elasticity data. Nature 543, 543–546.
Li, B., Liebermann, R.C., 2014. Study of the Earth's interior using measurements of sound velocities in minerals by ultrasonic interferometry. Phys. Earth Planet. Inter. 233, 135–153.
Luth, R.W., Stachel, T., 2014. The buffering capacity of lithospheric mantle: implications for diamond formation. Contrib. to Mineral. Petrol. 168, 1083.
Mans, W., Zhang, J.S., Hao, M., Smyth, J.R., Zhang, D., Finkelstein, G.J., Dera, P., 2019. Hydrogen Effect on the Sound Velocities of Upper Mantle Omphacite. Minerals 9, 690.
Mao, Z., Jacobsen, S.D., Jiang, F., Smyth, J.R., Holl, C.M., Duffy, T.S., 2008a. Elasticity of hydrous wadsleyite to 12 GPa: Implications for Earth's transition zone. Geophys. Res. Lett. 35, L21305.
Mao, Z., Jacobsen, S.D., Jiang, F., Smyth, J.R., Holl, C.M., Frost, D.J., Duffy, T.S., 2010. Velocity crossover between hydrous and anhydrous forsterite at high pressures. Earth Planet. Sci. Lett. 293, 250–258.
Mao, Z., Jacobsen, S.D., Jiang, F.M., Smyth, J.R., Holl, C.M., Frost, D.J., Duffy, T.S., 2008b. Single-crystal elasticity of wadsleyites, β-Mg2SiO4, containing 0.37–1.66 wt.% H2O. Earth Planet. Sci. Lett. 268, 540–549.
Mao, Z., Li, X., 2016. Effect of hydration on the elasticity of mantle minerals and its geophysical implications. Sci. China Earth Sci. 59, 873–888.
Mazzucchelli, M., Rivalenti, G., Brunelli, D., Zanetti, A., Boari, E., 2009. Formation of Highly Refractory Dunite by Focused Percolation of Pyroxenite-Derived Melt in the Balmuccia Peridotite Massif (Italy). J. Petrol. 50, 1205–1233.
McDonough, W.F., Rudnick, R.L., 1998. Mineralogy and composition of the upper mantle, in: Reviews in Mineralogy, Vol. 37. pp. 139–164.
Mei, S., Kohlstedt, D.L., 2000a. Influence of water on plastic deformation of olivine aggregates: 1. Diffusion creep regime. J. Geophys. Res. Solid Earth 105, 21457–21469.
Mei, S., Kohlstedt, D.L., 2000b. Influence of water on plastic deformation of olivine aggregates: 2. Dislocation creep regime. J. Geophys. Res. Solid Earth 105, 21471–21481.
Melchiorre, M., Faccini, B., Grégoire, M., Benoit, M., Casetta, F., Coltorti, M., 2020. Melting and metasomatism/refertilisation processes in the Patagonian sub-continental lithospheric mantle: A review. Lithos 354–355, 105324.
Meyer, H.O.A., 1987. Inclusions in diamond, in: Mantle Xenoliths. John Wiley & Sons, pp. 501–523.
Michael, P.J., 1988. The concentration, behavior and storage of H2O in the suboceanic upper mantle: Implications for mantle metasomatism. Geochim. Cosmochim. Acta 52, 555–566.
Milani, S., Nestola, F., Angel, R.J., Nimis, P., Harris, J.W., 2016. Crystallographic orientations of olivine inclusions in diamonds. Lithos 265, 312–316.

Mosenfelder, J.L., 2006. Hydrogen incorporation in olivine from 2-12 GPa. Am. Mineral. 91, 285–294.
Nestola, F., Jacob, D.E., Pamato, M.G., Pasqualetto, L., Oliveira, B., Greene, S., Perritt, S., Chinn, I., Milani, S., 2019. Protogenetic garnet inclusions and the age of diamonds. Geology 47, 431–434.
Nestola, F., Jung, H., Taylor, L.A., 2017. Mineral inclusions in diamonds may be synchronous but not syngenetic. Nat. Commun. 8, 1–6.
Nestola, F., Korolev, N., Kopylova, M., Rotiroti, N., Pearson, D.G., Pamato, M.G., Alvaro, M., Peruzzo, L., Gurney, J.J., Moore, A.E., Davidson, J., 2018. CaSiO3 perovskite in diamond indicates the recycling of oceanic crust into the lower mantle. Nature 555, 237–241.
Nestola, F., Nimis, P., Angel, R.J., Milani, S., Bruno, M., Prencipe, M., Harris, J.W., 2014. Olivine with diamond-imposed morphology included in diamonds. Syngenesis or protogenesis? Int. Geol. Rev. 56, 1658–1667.
Ni, H., Zhang, L., Guo, X., 2016. Water and partial melting of Earth's mantle. Sci. China Earth Sci. 59, 720–730.
Niu, Y., Langmuir, C.H., Kinzler, R.J., 1997. The origin of abyssal peridotites: A new perspective. Earth Planet. Sci. Lett. 152, 251–265.
Nye, J.F., 1985. Physical properties of crystals: their representation by tensors and matrices. Oxford university press.
O'Reilly, S.Y., Griffin, W.L., 2013. Mantle Metasomatism, in: Lecture Notes in Earth System Sciences. pp. 471–533.
Pamato, M.G., Novella, D., Jacob, D.E., Oliveira, B., Pearson, D.G., Greene, S., Afonso, J.C., Favero, M., Stachel, T., Alvaro, M., Nestola, F., 2021. Protogenetic sulfide inclusions in diamonds date the diamond formation event using Re-Os isotopes. Geology 49, 941–945.
Pasqualetto, L., Nestola, F., Jacob, D.E., Pamato, M.G., Oliveira, B., Perritt, S., Chinn, I., Nimis, P., Milani, S., Harris, J.W., 2022. Protogenetic clinopyroxene inclusions in diamond and Nd diffusion modeling—Implications for diamond dating. Geology 50, 1038–1042.
Pearson, D.G., Brenker, F.E., Nestola, F., Mcneill, J., Nasdala, L., Hutchison, M.T., Matveev, S., Mather, K., Silversmit, G., Schmitz, S., Vekemans, B., Vincze, L., 2014. Hydrous mantle transition zone indicated by ringwoodite included within diamond. Nature 507, 221–224.
Pearson, D.G., Canil, D., Shirey, S.B., 2003. Mantle Samples Included in Volcanic Rocks: Xenoliths and Diamonds, in: Treatise on Geochemistry. Elsevier, pp. 171–275.
Peslier, A.H., 2010. A review of water contents of nominally anhydrous natural minerals in the mantles of Earth, Mars and the Moon. J. Volcanol. Geotherm. Res. 197, 239–258.
Peslier, A.H., Woodland, A.B., Wolff, J.A., 2008. Fast kimberlite ascent rates estimated from hydrogen diffusion profiles in xenolithic mantle olivines from southern Africa. Geochim. Cosmochim. Acta 72, 2711–2722.
Poe, B.T., Romano, C., Nestola, F., Smyth, J.R., 2010. Electrical conductivity anisotropy of dry and hydrous olivine at 8GPa. Phys. Earth Planet. Inter. 181, 103–111.
Presnall, D.C., Gudfinnsson, G.H., Walter, M.J., 2002. Generation of mid-ocean ridge basalts at pressures from 1 to 7 GPa. Geochim. Cosmochim. Acta 66, 2073–2090.
Rauch, M., Keppler, H., 2002. Water solubility in orthopyroxene. Contrib. to Mineral. Petrol. 143, 525–536.
Richardson, S.H., Gurney, J.J., Erlank, A.J., Harris, J.W., 1984. Origin of diamonds in old enriched mantle. Nature 310, 198–202.
Ringwood, A.E., 1975. Composition and Petrology of the Earth's Mantle, Mac Graw-Hill Book Company.
Rivalenti, G., Mazzucchelli, M., Zanetti, A., Vannucci, R., Bollinger, C., Hémond, C., Bertotto, G.W., 2007. Xenoliths from Cerro de los Chenques (Patagonia): An example of slab-related metasomatism in the backarc lithospheric mantle. Lithos 99, 45–67.

Rizzo, A.L., Faccini, B., Casetta, F., Faccincani, L., Ntaflos, T., Italiano, F., Coltorti, M., 2021. Melting and metasomatism in West Eifel and Siebengebirge Sub-Continental Lithospheric Mantle: Evidence from concentrations of volatiles in fluid inclusions and petrology of ultramafic xenoliths. Chem. Geol. 581, 120400.
Rizzo, A.L., Pelorosso, B., Coltorti, M., Ntaflos, T., Bonadiman, C., Matusiak-Małek, M., Italiano, F., Bergonzoni, G., 2018. Geochemistry of noble gases and co2 in fluid inclusions from lithospheric mantle beneath wilcza góra (Lower silesia, southwest Poland). Front. Earth Sci. 6, 215.
Schaeffer, A.J., Lebedev, S., 2015. Global Heterogeneity of the Lithosphere and Underlying Mantle: A Seismological Appraisal Based on Multimode Surface-Wave Dispersion Analysis, Shear-Velocity Tomography, and Tectonic Regionalization, in: The Earth's Heterogeneous Mantle. Springer International Publishing, Cham, pp. 3–46.
Shirey, S.B., Cartigny, P., Frost, D.J., Keshav, S., Nestola, F., Nimis, P., Pearson, D.G., Sobolev, N., Walter, M.J., 2013. Diamonds and the Geology of Mantle Carbon, in: Reviews in Mineralogy and Geochemistry. pp. 355–421.
Shirey, S.B., Richardson, S.H., 2011. Start of the Wilson Cycle at 3 Ga Shown by Diamonds from Subcontinental Mantle. Science (80-. ). 333, 434–437.
Skogby, H., 2006. Water in Natural Mantle Minerals I: Pyroxenes. Rev. Mineral. Geochemistry 62, 155–167.
Smyth, J.R., Frost, D.J., Nestola, F., Holl, C.M., Bromiley, G., 2006. Olivine hydration in the deep upper mantle: Effects of temperature and silica activity. Geophys. Res. Lett. 33, L15301.
Smyth, J.R., Mierdel, K., Keppler, H., Langenhorst, F., Dubrovinsky, L., Nestola, F., 2007. Crystal chemistry of hydration in aluminous orthopyroxene. Am. Mineral. 92, 973–976.
Speziale, S., Marquardt, H., Duffy, T.S., 2014. Brillouin Scattering and its Application in Geosciences, in: Reviews in Mineralogy and Geochemistry. pp. 543–603.
Stachel, T., Aulbach, S., Harris, J.W., 2022. Mineral Inclusions in Lithospheric Diamonds. Rev. Mineral. Geochemistry 88, 307–391.
Stachel, T., Brey, G.P., Harris, J.W., 2005. Inclusions in Sublithospheric Diamonds: Glimpses of Deep Earth. Elements 1, 73–78.
Stachel, T., Harris, J.W., 2008. The origin of cratonic diamonds — Constraints from mineral inclusions. Ore Geol. Rev. 34, 5–32.
Stachel, T., Luth, R.W., 2015. Diamond formation - Where, when and how? Lithos 220–223, 200–220.
Stixrude, L., Lithgow-Bertelloni, C., 2012. Geophysics of Chemical Heterogeneity in the Mantle. Annu. Rev. Earth Planet. Sci. 40, 569–595.
Stixrude, L., Lithgow-Bertelloni, C., 2005. Thermodynamics of mantle minerals - I. Physical properties. Geophys. J. Int. 162, 610–632.
Sturhahn, W., 2004. Nuclear resonant spectroscopy. J. Phys. Condens. Matter 16, S497–S530.
Su, W., Woodward, R.L., Dziewonski, A.M., 1994. Degree 12 model of shear velocity heterogeneity in the mantle. J. Geophys. Res. 99, 6945.
Thio, V., Cobden, L., Trampert, J., 2016. Seismic signature of a hydrous mantle transition zone. Phys. Earth Planet. Inter. 250, 46–63.
Walter, M., 1998. Melting of Garnet Peridotite and the Origin of Komatiite and Depleted Lithosphere. J. Petrol. 39, 29–60.
Walter, M.J., Kohn, S.C., Araujo, D., Bulanova, G.P., Smith, C.B., Gaillou, E., Wang, J., Steele, A., Shirey, S.B., 2011. Deep Mantle Cycling of Oceanic Crust: Evidence from Diamonds and Their Mineral Inclusions. Science (80-. ). 334, 54–58.
Wang, J., Bass, J.D., Kastura, T., 2014. Elastic properties of iron-bearing wadsleyite to 17.7GPa: Implications for mantle mineral models. Phys. Earth Planet. Inter. 228, 92–96.

Watt, J.P., Davies, G.F., O'Connell, R.J., 1976. The elastic properties of composite materials. Rev. Geophys. 14, 541.
Withers, A.C., Wood, B.J., Carroll, M.R., 1998. The OH content of pyrope at high pressure. Chem. Geol. 147, 161–171.
Xia, Q.-K., Hao, Y., Li, P., Deloule, E., Coltorti, M., Dallai, L., Yang, X., Feng, M., 2010. Low water content of the Cenozoic lithospheric mantle beneath the eastern part of the North China Craton. J. Geophys. Res. 115, B07207.
Ye, Y., Schwering, R.A., Smyth, J.R., 2009. Effects of hydration on thermal expansion of forsterite, wadsleyite, and ringwoodite at ambient pressure. Am. Mineral. 94, 899–904.
Yoshino, T., Matsuzaki, T., Yamashita, S., Katsura, T., 2006. Hydrous olivine unable to account for conductivity anomaly at the top of the asthenosphere. Nature 443, 973–976.
Zhang, B.-H., Xia, Q.-K., 2021. Influence of water on the physical properties of olivine, wadsleyite, and ringwoodite. Eur. J. Mineral. 33, 39–75.

# 2. Methods

This chapter aims to provide a short introductory read to the principles and use of synchrotron Mössbauer spectroscopy, single-crystal X-ray diffraction, and Brillouin spectroscopy. Specific information relating to the experimental strategies will be found in the following chapters, which also include brief descriptions of the materials used.

## 2.1 Synchrotron Mössbauer spectroscopy

The technique of Mössbauer spectroscopy has recently gained renewed visibility in the fields of geosciences. Given that investigations of the 14.4 keV transition in $^{57}$Fe (which makes up ~2.2 % of natural Fe atoms) comprises the majority of mineralogical Mössbauer studies, this section will be focused on Fe, the widespread distribution and multivalence of which are of great importance in geological studies (e.g., McCammon, 2004).

The Mössbauer effect is the recoil-free emission and absorption of gamma ($\gamma$) rays by specific nuclei in a solid. The basic principle is that $\gamma$ rays emitted by a radioactive (i.e., decaying) source – $A^{\text{excited state}} \rightarrow A^{\text{ground state}} + \gamma$ – should be able to initiate the inverse process of nuclear resonant absorption in an absorber composed of atoms of the same type as those of the radioactive source – $A^{\text{ground state}} + \gamma \rightarrow A^{\text{excited state}}$. For a free, isolated nucleus in an excited nuclear state $E_e$ (such as a radiogenic isotope), the emission of a $\gamma$ photon related to the decay to the ground nuclear state $E_0$ is associated with a recoil momentum, which causes some of the energy liberated in the nuclear transition to be lost as recoil energy $E_R$. On the other hand, the transition occurs without a net recoil momentum for nuclei bounded into crystalline structures, so that the $\gamma$ photons carry away the entire energy $E_0$ which can be then absorbed by nuclei of the same type in a resonant capture process (Mössbauer, 1962).

Mössbauer spectroscopy probes small variations in the energy levels of atomic nuclei in response to the nuclear electronic environments around the nuclei. The slight modifications in the exact value of the energy difference between nuclear energy levels of the specific nuclei in a sample are defined as *hyperfine interactions* and reveal their local structural environments, such as valence state and site geometry. Thus, if the energy of the incident $\gamma$ photons matches exactly the correct quantized transition energy of specific nuclei, they can be absorbed and can cause nuclear transitions from the ground state to the excited state. In practice, the energy of the incident $\gamma$ photons can be Doppler fine-tuned by an amount of $\Delta E = E_\gamma(v/c)$ by moving the emitting source with a relative velocity towards and away from the fixed absorbing sample and then, if $\gamma$ photons transmitted through the sample excite nuclear transitions, absorption peaks will be detected in the resulting spectrum (Figure 2.1). The

exact value of the energy difference between nuclear energy levels depends on the interactions of the nuclear charge with the electric and magnetic field produced by the immediate environment of the nucleus. Therefore, different sets of peaks correspond to Fe nuclei in a specific environment in the sample, depending on several factors, including the number of electrons ($Fe^0$, $Fe^{2+}$, $Fe^{3+}$), the number of coordinating anions, the symmetry of the site, the presence/absence of magnetic ordering, etc.

The centre shift (CS) (or isomer shift, IS) is largely sensitive to the *s*-valence electron density at the nuclei in the absorber (i.e., the oxidation state) and is created due to the difference in electron density at the nuclear sites in the source and absorber atoms, which leads to a shift (an offset from zero velocity in the transmission spectrum) in Mössbauer transition energies. The quadrupole splitting (QS) is largely sensitive to the surrounding atomic environment, and therefore to site geometries and oxidation state, as it probes the interaction of the nuclear quadrupole moment with the electric field gradient (EFG) around the nucleus caused by a non-cubic charge distribution, which causes a split into two nuclear energy sublevels. Having a magnetic moment, the energy levels of $^{57}Fe$ nuclei can be perturbed in the case of magnetically ordered materials, or under an external magnetic field, the effect being a split into six nuclear energy sublevels, a measure of which is given by the magnetic hyperfine field (BHF) (Figure 2.1; e.g., Dyar et al., 2006; McCammon, 2004).

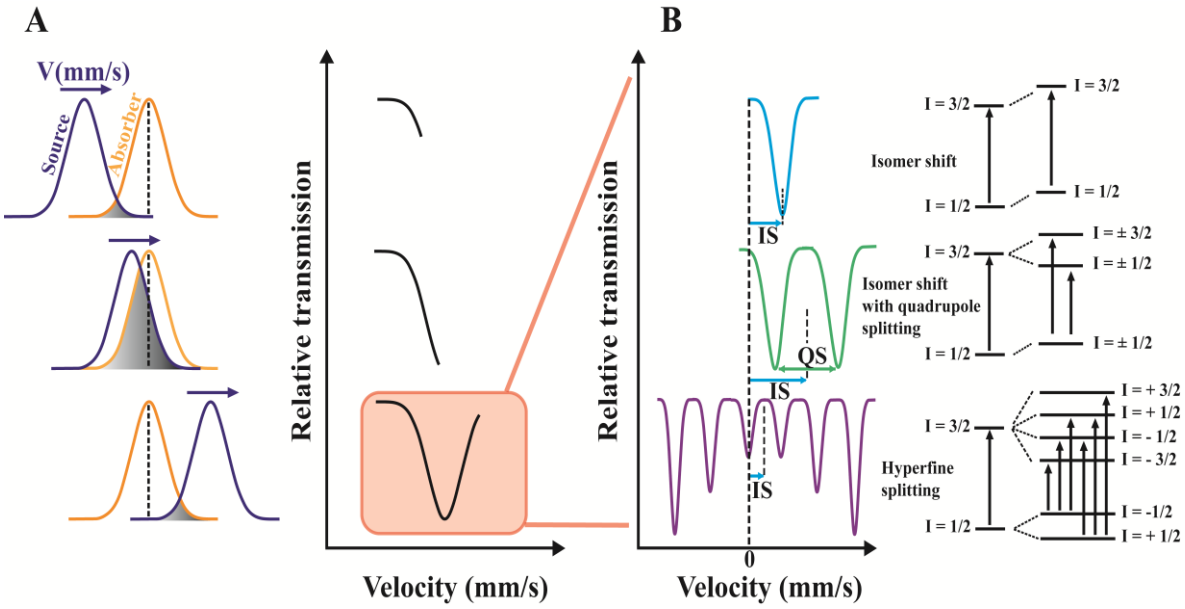


**Figure 2.1.** (a) The emitting source is moved towards and away from the fixed absorbing sample to tune the incident energy and the emission spectrum changes from having no overlap with the absorbing spectrum to maximum overlap and back again to no overlap. The transmitted photons are measured in function of the source velocity. (b) When the source and absorber atoms are in different local environments, their nuclear energy levels are different, and the absorber energy levels may be shifted and split apart (adapted from Dyar et al., 2006).

Conventional Mössbauer sources use the 270-day half-life decay of $^{57}$Co to the 136.3 keV-level of $^{57}$Fe, which then in most cases decays to an intermediate 14.4-keV state and then to the ground state, with emission of the characteristic 14.4-keV $\gamma$ radiation which is used to probe $^{57}$Fe in the sample (e.g., Dyar et al., 2006). However, source radiation can also be generated by a particle accelerator, such as a synchrotron facility. The recently developed $^{57}$Fe Synchrotron Mössbauer Source (SMS) for energy-domain Mössbauer spectroscopy at the nuclear resonance beamline ID18 (Rüffer and Chumakov, 1996) at the European Synchrotron (ESRF) combines the advantages of synchrotron radiation and Mössbauer Spectroscopy. The SMS exploits a nuclear resonant monochromator employing pure nuclear reflections of an iron borate ($^{57}FeBO_3$) crystal. The source provides $^{57}$Fe resonant radiation at 14.4 keV within a bandwidth of 15 neV which is tuneable in energy over a range of about ± 0.6 μeV (i.e., ± 12mm s$^{-1}$). In contrast to radioactive sources, the beam of hard X-ray radiation emitted by the SMS is almost fully resonant and linearly polarized, has high brilliance and can be focused down to micrometric spot size (Potapkin et al., 2012), and even below (upgrade of the ESRF to a 4$^{th}$-generation synchrotron source, ESRF-EBS). The small cross-section of the beam and its high intensity allow for much more rapid collection times than conventional sources. Compared to a conventional Mössbauer apparatus, the setup of the SMS includes two additional elements, besides the iron borate crystal: the High-Resolution Monochromator (HRM), which decreases the heat load on the iron borate crystal, and the deflector, which rotates the beam on the iron borate crystal in the vertical plane so that the beam emitted by the crystal is directed almost horizontally (Figure 2.2). This setup allows measurements of high signal-to-noise ratio and well-resolved energy domain spectra on the timescale of only a few hours, as well as in situ measurements of Fe-bearing inclusions in diamonds (Nestola et al., 2016).

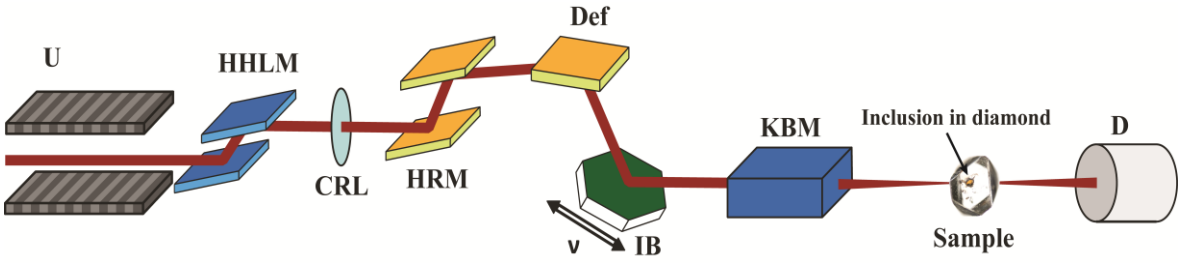


**Figure 2.2.** Simplified scheme of the synchrotron Mössbauer source at ID18, ESRF, based on the (333) pure nuclear reflection. U (undulator), HHLM (high-heat-load monochromator), CRL (compound refractive lens), HRM (high-resolution monochromator), Def (Si (311) deflector), IB (iron borate crystal mounted on the Mössbauer transducer), KBM (Kirkpatrick-Baez mirrors), D (detector) (after Potapkin et al., 2012, courtesy of G. Criniti).

## 2.2 Single-crystal X-ray diffraction

Crystalline materials are characterized by a periodic, three-dimensional distribution of atoms in space and therefore may act as three-dimensional diffraction gratings for electromagnetic waves, as well as particles (e.g., electrons and neutrons), provided that the radiation has a comparable wavelength to interatomic distances in the crystal structure. As X-rays with wavelengths in the order of 1 Å fulfil this requirement, X-ray diffraction has become a routine technique for obtaining structural information of crystalline materials, such as unit-cell parameters and atomic structures.

Diffraction is based on Bragg's Law:

$$n\lambda = 2d_{hkl}sin\theta \tag{2.1}$$

which describes the relationship between the wavelength $\lambda$ of the incident radiation, the interplanar distance $d$ of crystalline materials, and the scattering angle $\theta$. Bragg's Law illustrates the geometrical conditions in which monochromatic X-rays scattered by two successive *hkl* planes have constructive interference, i.e., when the paths of the incident and scattered radiation are shifted by an integer $n$ multiple of the wavelength $\lambda$, which is the condition for diffraction. In an X-ray diffraction experiment, the geometry of the crystal lattice is converted into diffraction angles $2\theta$ of diffracted X-ray beams, each of which is indexed according to Miller indices *hkl* corresponding to scattering from a lattice plane (*hkl*), and the order of diffraction (or constructive interference) is conventionally set to $n = 1$. For orthorhombic crystal symmetry, for example, the spacing of a given family of planes relates to the lattice parameters as:

$$\frac{1}{d_{hkl}^2} = \frac{h^2}{a^2} + \frac{k^2}{b^2} + \frac{l^2}{c^2} \tag{2.2}$$

where $a$, $b$, and $c$ are the unit-cell edge lengths. If the orientation of the crystal is changed with respect to the incident radiation, different diffraction directions of the crystal lattice can be probed. The lattice parameters can be refined using a least-squares method by measuring a sufficiently large number of diffraction angles, and hence the lattice spacings of the corresponding planes.

Single-crystal diffraction measurements are carried out using X-ray diffractometers, where X-rays, generated either by X-ray tubes, rotating anodes, or microfocus sources, are waved through filters and monochromators to isolate the $K\alpha 1$ and $K\alpha 2$ components from the

bremsstrahlung and other emission lines, collimated to reduce the angular divergence of the beam and focused to the sample. In Eulerian four-circle diffractometers (Figure 2.3), the diffraction plane contains the incident X-rays, the sample (mounted onto a goniometer head), and either a point or area detector for determining the position and intensity of reflections. The four goniometer circles $\omega$, $\chi$, $\varphi$ and $2\theta$ are all capable of independent rotations and are used to rotate the sample so that different *hkl* planes are brought into diffraction and the diffracted beams are detected by the detector. The $\omega$-circle rotates the $\chi$-circle, on which is carried the $\varphi$-circle. Finally, the detector arm moves in the diffraction plane and its angle of deviation from the line of the direct beam is twice the Bragg angle, $2\theta$ (e.g., Angel et al., 2000).

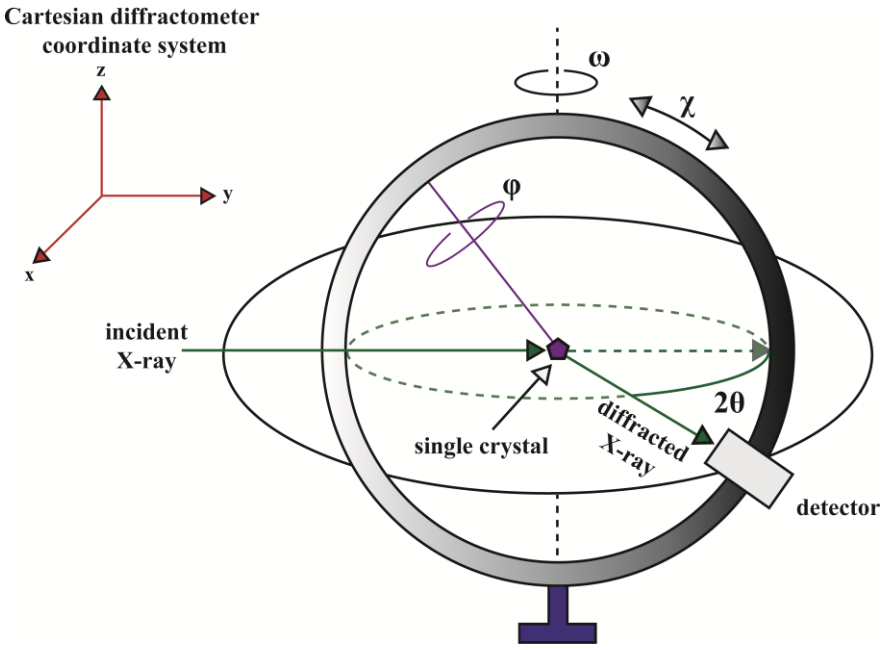


**Figure 2.3.** Simplified sketch of an Eulerian four-circle single-crystal diffractometer. The crystal can be automatically rotated around the three different axes $\omega$, $\chi$, and $\varphi$; the detector moves on the $2\theta$ rotation. When all circles are at their zero positions, the detector lies in the position of the undiffracted direct beam ($2\theta = 0$), the plane of the $\chi$ circle is perpendicular to the direct beam ($\omega = 0$), the $\varphi$-axis is perpendicular to the diffraction plane ($\chi = 0$). The axes of the Cartesian coordinate system of the diffractometer are also shown.

These geometrical conventions and relations are relevant for defining the crystal orientation with respect to the diffractometer angles, which are determined through the orientation matrix (UB). In more precise terms, the UB matrix relates the reciprocal axes of the crystal with the Cartesian coordinate system of the diffractometer. Given the UB matrix, it is possible to calculate the diffractometer angles ($2\theta$, $\chi$, $\varphi$, $\omega$) necessary to bring a reflection *hkl* into the diffraction position and the diffracted beam to the detector, which is of particular importance for high-pressure Brillouin spectroscopy experiments (see Chapter 5).

Single-crystal X-ray diffraction measurements at high pressure using diamond anvil cells (Figure 2.4) have become standard in the fields of mineral physics and material sciences (e.g., Angel et al., 2000; Boffa Ballaran et al., 2013).

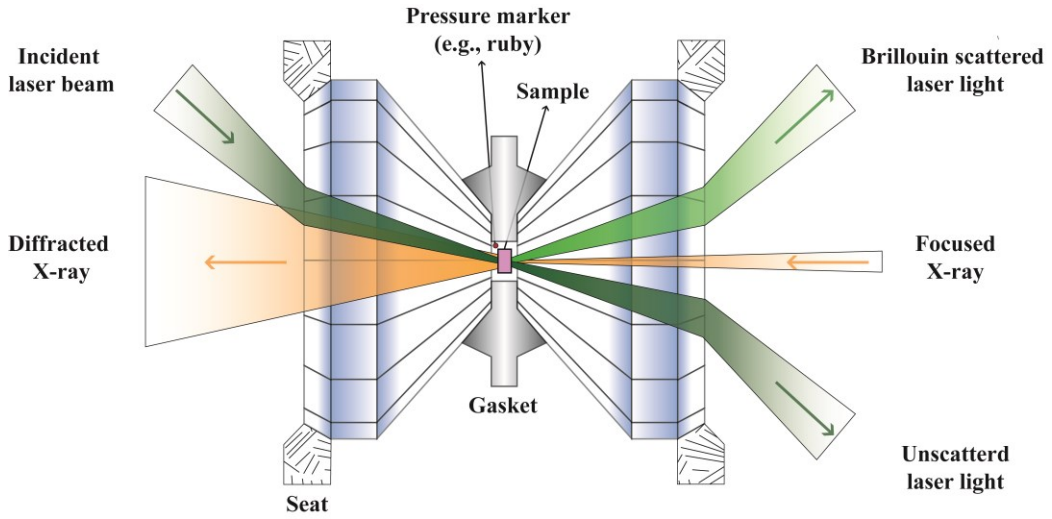


**Figure 2.4.** Schematic drawing showing the components of a diamond anvil cell. The sample is between the two opposed diamond anvils, within a hole in the gasket (sample chamber). X-rays pass through the transparent diamonds and are diffracted by the sample. Simultaneous measurements of X-ray diffraction and light-scattering experiments (green laser beam, Brillouin spectroscopy) can be conducted. Adapted from Bass et al. (2008)

DACs are probably the most commonly used devices in high-pressure research. The transparency of diamonds to X-rays and visible light allows several physical properties on samples held at high pressures inside DACs to be determined (e.g., Jayaraman, 1983). The basic principle of the DACs is very simple, pressure is generated by compressing the sample placed between two small, flat, parallel 'culet' surfaces at the tips of two opposed gem-quality diamond anvils. The diamond culets have diameters in the order of 0.1–1 mm and, therefore, because Pressure = Force / Area, a relatively small force applied on the diamonds may produce very high pressures such as those of Earth's core or greater. The two opposed diamonds compress the sample hosted in a sample chamber consisting of a hole in the gasket, i.e., a thin metal foil where a hole is drilled at the centre of the indentation made by the two anvils. The sample chamber also contains a soft, hydrostatic, pressure-transmitting medium, such as He or Ne (e.g., Klotz et al., 2009), and a pressure calibrant, such as a small ruby sphere. The fluorescence wavelengths of ruby are strongly pressure-dependent, and this property can be used to determine the pressure in the sample chamber (e.g., Shen et al., 2020). There are also alternative pressure calibrants, such as MgO and Au, the lattice parameters of which are commonly used to calculate pressure. The versatility of DACs is ideally suited for use in many types of elasticity measurements, such as Brillouin

spectroscopy. Both high-pressure X-ray diffraction and Brillouin spectroscopy require DACs with a large opening angle so that the cell can be tilted while X-rays or laser beams are still passing through the sample. The BX90 diamond anvil cell (Kantor et al., 2012) was designed with a 90° external opening angle and is well suited for these kinds of experiments.

### 2.2.1 Structure refinements

While the determination of unit-cell parameters is based only on the position of reflections, analysis of the intensity of the reflections is required to determine the atomic coordinates. The diffraction pattern of a mineral contains several hundred unique reflections, each of which is indexed with specific Miller indices *hkl* corresponding to scattering from a lattice plane. Each diffracted beam is a wave with a characteristic amplitude and phase. These quantities are combined in the structure factor, $F(hkl)$. The structure factor can be written as the sum of the individual waves diffracted by each of the atoms in the unit cell for the conditions specified by the Bragg equation:

$$F(hkl) = \sum_j f_j \, exp\left(2\pi i\left(hx_j + ky_j + lz_j\right)\right) \tag{2.3}$$

where $x_j$, $y_j$, and $z_j$ are the positional coordinates of the $j$-th atom and $f_j$ is the scattering factor of the $j$-th atom. The amplitude $|F(hkl)|$ of the diffracted beam is termed structure amplitude, while its intensity is proportional to the squared structure amplitude $|F(hkl)|^2$. Therefore, the atomic positions in the unit cell and the atomic scattering factors influence the phase, amplitude, and intensity of the diffracted beam.

The intensity $|F(hkl)|^2$ of the diffracted beams is measured experimentally, and the atomic scattering factors can be calculated from the physical properties of the atom species, but the phase, which depends on the atomic positions, cannot be determined by direct experimental observation (the so-called phase problem). If the phases are inferred, then the atomic positional coordinates can be calculated from Equation (2.3). The phase problem constitutes the major obstacle to constructing an initial structural model and is addressed through experimental and theoretical procedures, including trial and error methods, the Patterson synthesis, direct methods, charge flipping methods, etc. (see Hammond, 2015).

Direct methods have become the standard technique for solving the phase problem, which is eluded by assigning arbitrary phases to a set of reflections with known amplitudes and by Fourier-transforming the amplitudes and phases of the diffracted beams to produce the initial electron density map, consisting of peaks of high electron density (the resolved atoms)

surrounded by low electron density areas. The way from the first rough solution to the final accurate model is called structure refinement. The structure refinement is an iterative procedure that consists of least-squares minimization between the experimental structure factors ($F_{obs}$) and those calculated ($F_{calc}$) by varying the adjustable parameters of the structural model, to improve the agreement between the structural model and the experimental diffraction intensities. These normally include correct assignments of atoms to residual in the electron density map (Fourier difference map, $1F_{obs} - 1F_{calc}$), where heavier elements are assigned to higher electron density peaks and vice versa. An indication of atom species is provided by distances between atoms and residuals, as atomic bonds are closely related to ionic radii, whose values are well known and tabulated (Shannon, 1976). Other common steps include refining atomic positions, switching from isotropic to anisotropic displacement parameters (atomic thermal motions can be constrained to be equal in all three directions, i.e., spherical, or not, i.e., ellipsoidal), refining site occupancies (which, in the absence of disorder, are fixed to unity, i.e., the atomic sites are fully occupied) and/or splitting them between two different elements (for example, in the case of Mg-Fe isomorphous replacement), employing ionized atomic scattering curves (scattering factors considerably vary between the neutral and charged atoms) (e.g., Angel and Nestola, 2016; Nestola et al., 2011).

The final structure solution is presented with statistical parameters. The *R*int is an intrinsic datum, giving the percent variation between the observed intensities for symmetry equivalent reflections, where ideal measurements would have *R*int = 0:

$$Rint = \frac{\sum | F_{obs}^2 - \langle F_{obs}^2 \rangle |}{\sum F_{obs}^2} \quad (2.4)$$

The *R*-value (*R*1 in SHELXL) gives the percent variation between the calculated and observed model; ideal solutions would have *R*1 = 0, but values < 5% are considered good solutions.

$$R1 = \frac{\sum \big| |F_{obs}| - |F_{calc}| \big|}{\sum |F_{obs}|} \quad (2.5)$$

The *GooF* (goodness of fit) factor considers the calculated and observed model, a weighting factor *w*, the number of independent reflections ($N_R$), and the number of refined parameters ($N_P$). For a properly adjusted weighting scheme, *GooF* is ~1:

$$GooF = \left[\frac{\sum w(F_{obs}^2 - F_{calc}^2)^2}{(N_R - N_P)}\right]^{1/2} \quad (2.6)$$

In summary, a successful structure refinement leads to a complete list of atoms and atomic positions in the unit cell, site occupancy factors, atomic displacement parameters, bond lengths, bond angles, and other additional computable quantities.

## 2.3 Brillouin spectroscopy

Brillouin scattering is a very sensitive technique widely used to determine the sound wave velocities and full elastic tensors of transparent samples by measuring the scattering of an incident laser light due to interaction with thermally excited sound waves (acoustic phonons) propagating in the material under study (Cummins and Schoen, 1972). In Brillouin scattering measurements, a small fraction of the laser light interacts inelastically with the collective acoustic vibrations, leading to a frequency shift (Brillouin shift, $\Delta\omega_i$) relative to the frequency of the incident light $\omega$ (Figure 2.5a). In some of these interactions, the incoming laser light excites new vibrations and some of its energy is transferred to the vibrations (Stokes event, negative frequency shifts). In other cases, energy is transferred from the acoustic mode to the incident light, and this is associated with an increase in the frequency of the light scattered by the sample (anti-Stokes events, positive frequency shifts). Most crystalline materials are elastically anisotropic, meaning that propagating acoustic waves have different velocities in different crystallographic directions, and it is important to control the scattering angle and phonon direction for single crystals.

The frequency of the scattered light is then measured by a high-resolution Fabry-Pérot interferometer (Figure 2.5b), because frequency shifts are very small (typically of the order of 1 $cm^{-1}$, that is in the GHz frequency range) and the spectral lines are very close to the unshifted (Rayleigh scattering) incident light frequency (e.g., Angel et al., 2009; Speziale et al., 2014).

Brillouin scattering frequency shifts $\Delta\omega_i$ from the central Rayleigh peak depend on the scattering geometry ($\theta$, angle between the incident and scattered light beams), the wavelength of the incident laser light, the refractive index $n$ of the sample, and the phonon velocities in the sample along the particular crystallographic direction; the relationship between these parameters is defined as:

$$v_i = \frac{\Delta\omega_i \lambda}{2n sin\left(\frac{\theta}{2}\right)} \tag{2.6}$$

where $v_i$ describes the acoustic waves, either the longitudinal $v_P$ or one of the two shear waves $v_{S1}$ and $v_{S2}$ having different polarizations. In elastically isotropic solids (perfect polycrystalline aggregates, or glasses, the two $v_S$ have the same frequency and appear as one peak in the spectrum (Figure 2.5c).

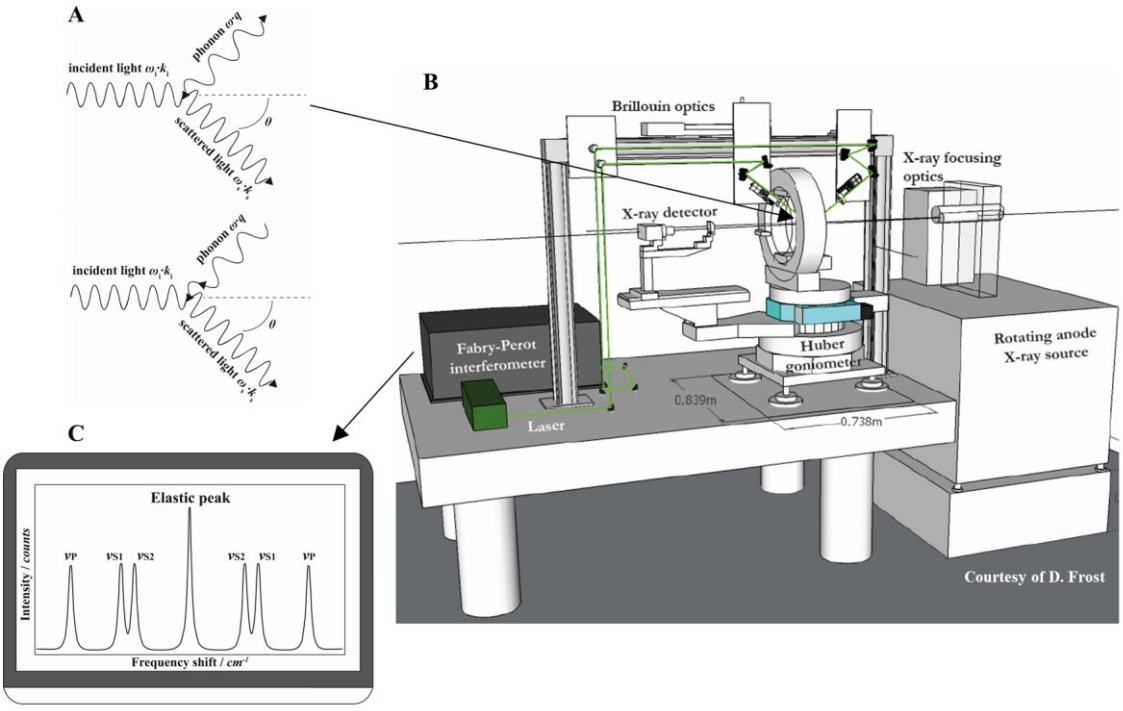


**Figure 2.5.** (a) Schematic representation of the two types of inelastic interaction between incident light and the vibrational modes in a crystal, represented by phonons. In each case, a quantum of energy $h\omega$ (where $h$ is Planck's constant) is exchanged. In Stokes events, the energy is transferred to the phonon, and the energy (or frequency) of the scattered radiation is reduced. In anti-Stokes events, the energy is transferred from the phonon to the radiation, which is increased in energy (or frequency). (b) Schematic view of the Brillouin spectroscopy and X-ray diffraction systems installed at the Bayerisches Geoinstitut, University of Bayreuth. (c) Simplified Brillouin scattering spectrum of an elastically anisotropic medium, containing a strong, unshifted peak corresponding to the elastically scattered light peak (Rayleigh peak), and three sets of peaks (symmetric with respect to the unshifted line) due to Brillouin scattering, where $v_{S1}$ and $v_{S2}$ peaks correspond to the slow and the fast shear acoustic modes, respectively, and $v_P$ to the longitudinal acoustic mode. (a) and (c) adapted from Angel et al. (2009) and Speziale et al. (2014), (b) courtesy of D. Frost.

In general, acoustic wave velocities in crystals are different in different crystallographic directions. The velocities of acoustic phonons propagating in a sample are related to the density and adiabatic single-crystal elastic moduli through Christoffel's equation:

$$\left|c_{ijkl}q_jq_l - \rho v_i^2\delta_{ik}\right| = 0 \quad (2.7)$$

where $c_{ijkl}$ are the elastic stiffness coefficients in tensorial notation (e.g., Nye, 1985), $q_j$ and $q_l$ are direction cosines, $\rho$ is the density, $v_i$ are the sound wave velocities and $\delta_{ik}$ is the Kronecker delta.

Because Brillouin shifts depend on the refractive index of the media through which light passes, experimental strategies have been established to solve the complications introduced by high-pressure Brillouin scattering experiments in DAC, where the incident light passes through the diamond anvils and the pressure medium, beyond the sample under study, each having different refractive indexes.

However, the introduction of the symmetric forward scattering geometry (Speziale et al., 2014; Whitfield et al., 1976), where the sample must be a plate with two surfaces parallel to those of the diamond anvils and the incident and scattered beam paths are symmetrical, allowed the velocities of the acoustic waves to be independent of the refractive indexes of the sample, diamonds, and pressure medium. Therefore, the refractive index $n$ cancels out from Equation (2.6), and the scattering angle $\theta$ is replaced by the external scattering angle $\theta$*, determined by the directions of the incident and scattered wavevectors outside the sample environment.

Brillouin scattering is usually combined with X-ray diffraction measurements to determine lattice parameters (and density) and the orientation of the sample, which are both important parameters for accurate assessment of elastic stiffness coefficients $c_{ij}$ (e.g., Buchen, 2021; Sinogeikin et al., 2006). Moreover, simultaneous velocity and density measurements give the additional benefit of having an absolute pressure scale, independent of secondary external pressure markers.

# References


Angel, R.J., Downs, R.T., Finger, L.W., 2000. High-Temperature-High- Pressure Diffractometry. Rev. Mineral. Geochemistry 41, 559–597.

Angel, R.J., Jackson, J.M., Reichmann, H.J., Speziale, S., 2009. Elasticity measurements on minerals: a review. Eur. J. Mineral. 21, 525–550.

Angel, R.J., Nestola, F., 2016. A century of mineral structures: How well do we know them? Am. Mineral. 101, 1036–1045.

Bass, J.D., Sinogeikin, S. V., Li, B., 2008. Elastic Properties of Minerals: A Key for Understanding the Composition and Temperature of Earth's Interior. Elements 4, 165–170.

Boffa Ballaran, T., Kurnosov, A., Trots, D., 2013. Single-crystal X-ray diffraction at extreme conditions: a review. High Press. Res. 33, 453–465.

Buchen, J., 2021. Seismic Wave Velocities in Earth's Mantle from Mineral Elasticity, in: Mantle Convection and Surface Expressions. pp. 51–95.

Dyar, M.D., Agresti, D.G., Schaefer, M.W., Grant, C.A., Sklute, E.C., 2006. MÖSSBAUER SPECTROSCOPY OF EARTH AND PLANETARY MATERIALS. Annu. Rev. Earth Planet. Sci. 34, 83–125.

Hammond, C., 2015. Fourier analysis in diffraction and image formation, in: The Basics of Crystallography and Diffraction. Oxford University Press, pp. 329–356.

Jayaraman, A., 1983. Diamond anvil cell and high-pressure physical investigations. Rev. Mod. Phys. 55, 65–108.

Kantor, I., Prakapenka, V., Kantor, A., Dera, P., Kurnosov, A., Sinogeikin, S., Dubrovinskaia, N., Dubrovinsky, L., 2012. BX90: A new diamond anvil cell design for X-ray diffraction and optical measurements. Rev. Sci. Instrum. 83, 125102.

Klotz, S., Chervin, J.-C., Munsch, P., Le Marchand, G., 2009. Hydrostatic limits of 11 pressure transmitting media. J. Phys. D. Appl. Phys. 42, 075413.

McCammon, C.A., 2004. Mössbauer spectroscopy: Applications, in: Spectroscopic Methods in Mineralogy. Mineralogical Society of Great Britain and Ireland, pp. 369–398.

Mössbauer, R.L., 1962. Recoilless Nuclear Resonance Absorption of Gamma Radiation. Science (80-. ). 137, 731–738.

Nestola, F., Cerantola, V., Milani, S., Anzolini, C., McCammon, C., Novella, D., Kupenko, I., Chumakov, A., Rüffer, R., Harris, J.W., 2016. Synchrotron Mössbauer Source technique for in situ measurement of iron-bearing inclusions in natural diamonds. Lithos 265, 328–333.

Nestola, F., Nimis, P., Ziberna, L., Longo, M., Marzoli, A., Harris, J.W., Manghnani, M.H., Fedortchouk, Y., 2011. First crystal-structure determination of olivine in diamond: Composition and implications for provenance in the Earth's mantle. Earth Planet. Sci. Lett. 305, 249–255.

Nye, J.F., 1985. Physical properties of crystals: their representation by tensors and matrices. Oxford university press.

Potapkin, V., Chumakov, A., Smirnov, G., Celse, J., Rüffer, R., McCammon, C.A., Dubrovinsky, L., 2012. The 57Fe Synchrotron Mössbauer Source at the ESRF. J. Synchrotron Radiat. 19, 559–569.

Rüffer, R., Chumakov, A.I., 1996. Nuclear-resonance beamline at ESRF. Hyperfine Interact. 97–98, 586–604.

Shannon, R.D., 1976. Revised Effective Ionic Radii and Systematic Studies of Interatomic Distances in Halides and Chaleogenides. Acta Crystallogr. A 32, 751–767.

Shen, G., Wang, Y., Dewaele, A., Wu, C., Fratanduono, D.E., Eggert, J., Klotz, S., Dziubek, K.F., Loubeyre, P., Fat'yanov, O. V., Asimow, P.D., Mashimo, T., Wentzcovitch, R.M.M., 2020. Toward an international practical pressure scale: A proposal for an IPPS ruby gauge (IPPS-Ruby2020). High Press. Res. 40, 299–314.

Sinogeikin, S., Bass, J., Prakapenka, V., Lakshtanov, D., Shen, G., Sanchez-Valle, C., Rivers, M., 2006. Brillouin spectrometer interfaced with synchrotron radiation for simultaneous x-ray density and acoustic velocity measurements. Rev. Sci. Instrum. 77, 103905.
Speziale, S., Marquardt, H., Duffy, T.S., 2014. Brillouin Scattering and its Application in Geosciences, in: Reviews in Mineralogy and Geochemistry. pp. 543–603.
Whitfield, C.H., Brody, E.M., Bassett, W.A., 1976. Elastic moduli of NaCl by Brillouin scattering at high pressure in a diamond anvil cell. Rev. Sci. Instrum. 47, 942–947.

# 3. Relatively oxidized conditions for diamond formation at Udachnaya (Siberia)

Luca FACCINCANI [1,✉], Valerio CERANTOLA [2,3], Fabrizio NESTOLA [4], Paolo NIMIS [4], Luca ZIBERNA [5,6], Leonardo PASQUALETTO [4], Aleksandr I. CHUMAKOV [3], Jeffrey W. HARRIS [7], Massimo COLTORTI [1]

[1] Department of Physics and Earth Sciences, University of Ferrara, Via Saragat 1, 44121 Ferrara, Italy
[2] Department of Earth and Environmental Sciences, Università degli Studi di Milano-Bicocca, Piazza della Scienza 4, 20126 Milan, Italy
[3] ESRF – The European Synchrotron, CS40220, 38043 Grenoble Cedex 9, France
[4] Department of Geosciences, University of Padua, Via Gradenigo 6, 35131 Padua, Italy
[5] Department of Mathematics and Geoscience, University of Trieste, Via Weiss 2, 34128 Trieste, Italy
[6] Bayerisches Geoinstitut, University of Bayreuth, Universitätsstraße 30, 95440 Bayreuth, Germany
[7] School of Geographical and Earth Sciences, University of Glasgow, G12 8QQ Glasgow, UK
✉ luca.faccincani@unife.it

This chapter has been published as:
Faccincani et al. (2022) *European Journal of Mineralogy*, **34**, 549–561.

## Abstract

Thanks to the physical strength of diamonds and their relatively unreactive chemical nature, their mineral inclusions may remain exceptionally preserved from alteration processes and chemical exchanges with surrounding minerals, fluids and/or melts following diamond formation. Cr-bearing spinels are relatively common inclusions found in peridotitic diamonds and important oxybarometers providing information about the oxygen fugacity ($fO_2$) of their source mantle rocks. Here, we investigated a magnesiochromite-olivine touching pair in a diamond from the Udachnaya kimberlite (Siberia) by in situ single-crystal X-ray diffraction and energy-domain synchrotron Mössbauer spectroscopy, aiming to constrain the physical-chemical conditions of diamond formation and to explore the redox state of this portion of the Siberian craton when the diamond was formed.

The $P$–$T$–$fO_2$ entrapment conditions of the inclusion pair, determined by thermo-/oxybarometric analyses, are ~5.7(0.4) GPa and ~1015(50) °C (although entrapment at higher $T$ and re-equilibration during subsequent mantle storage are also possible) and $fO_2$ near the enstatite-magnesite-olivine-diamond (EMOD) buffer. The determined $fO_2$ is similar to, or slightly more oxidized than, those of xenoliths from Udachnaya, but whilst the xenoliths last equilibrated with the surrounding mantle just prior to their entrainment in the

kimberlite at ~360 Ma, the last equilibration of the inclusion pair is much older, occurring at 3.5–3.1, ~2 or ~1.8 Ga before final encapsulation in its host diamond. Hence, the similarity between xenoliths and inclusion $fO_2$ values indicates that the modern redox state of this portion of the Siberian lithosphere was likely attained relatively early after its formation and may have persisted for billions of years after diamond formation, at least at the local scale. Moreover, the oxygen fugacity determination for the inclusion pair provides direct evidence of diamond formation near the EMOD buffer and is consistent with recent models suggesting relatively oxidized, water-rich CHO fluids as the most likely parents for lithospheric diamonds.

**Keywords:** inclusions in diamond, oxygen fugacity, Siberian craton, Udachnaya kimberlite, diamond formation, lithospheric mantle

# 3.1 Introduction

Virtually all mineral inclusions in diamond (98%) formed beneath cratons at depths between about 130 and 230 km (i.e., lithospheric), with the remainder forming in the asthenosphere, transition zone or lower mantle (i.e., sub-lithospheric) (e.g., Kaminsky et al., 2001; Stachel and Harris, 2008; Shirey et al., 2013; Stachel et al., 2022). Once trapped in their diamond hosts, these inclusions remain uncorrupted over geological time and represent key geological samples from otherwise inaccessible regions of our planet. Furthermore, these minerals can reveal the physical-chemical environment in which their host diamonds were formed (Bulanova et al., 2010; Stachel and Luth, 2015; Jean et al., 2016; Nimis et al., 2016; Nestola et al., 2018).

Cr-bearing spinels $(Mg, Fe^{2+})(Cr, Al, Fe^{3+})_2O_4$ (mainly magnesiochromites, hereafter mchr in the singular) are among the more common inclusions found in the peridotitic suite of lithospheric diamonds (e.g., Sobolev, 1977; Meyer, 1987; Stachel and Harris, 2008) as well as a recurrent accessory phase in ultramafic rocks. Despite their accessory nature (Cr-bearing spinels are disseminated in quantities of less than 3% in on- and off-craton peridotite xenoliths; Pearson et al., 2003), they are important petrogenetic and oxybarometric indicators, providing information about the physico-chemical conditions under which their host rocks formed (e.g., O'Neill and Wall, 1987; Ballhaus et al., 1991; Barnes and Roeder, 2001; Miller et al., 2016). Oxygen fugacity, $fO_2$, is the thermodynamic variable that allows quantification of the chemical potential of oxygen in reactions where at least one element changes its oxidation state between the reagents and products. In mantle peridotites, $fO_2$ is

estimated from the compositions of coexisting Fe-rich minerals, such as olivine, orthopyroxene, spinel and garnet. Essentially, $fO_2$ reflects Earth's mantle oxidation state, which can control the speciation of carbon in fluids or melts and governs the stability of carbon-bearing phases, such as diamond and carbonate minerals (e.g., Frost and McCammon, 2008; Stagno et al., 2013).

Here, we provide the first oxygen fugacity estimate for a mchr-olivine touching inclusion pair still trapped in a diamond (Oli-CHR1) from the Udachnaya kimberlite (Siberia, Russia). The diamond, previously investigated by Nestola et al. (2014) and Nimis et al. (2016, 2019), was recovered from the run-of-mine production, the vast majority of which is from kimberlite and most unlikely from any rare accompanying xenoliths. The colourless diamond is octahedral in shape with most faces showing bevelled edges. As seen in Figure 3.1, mchr dominates the inclusion pair, which is situated in a peripheral position in the diamond.

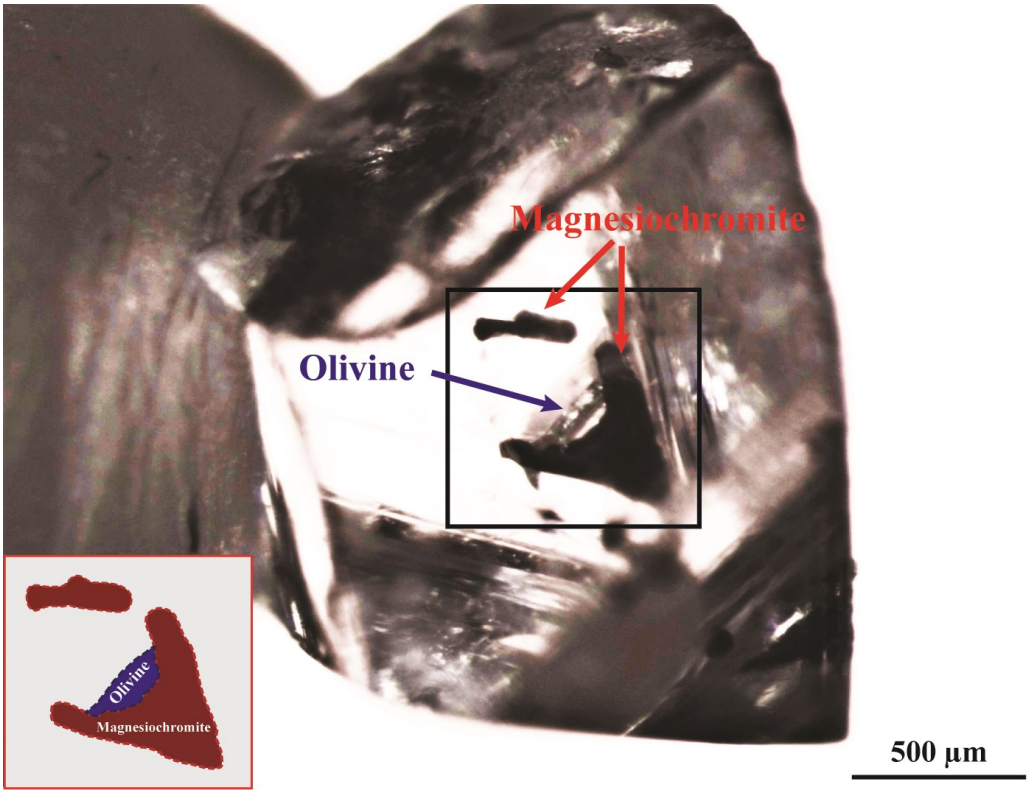


**Figure 3.1.** Close-up photograph of the Oli-CHR1 diamond shows the studied mchr-olivine inclusion pair (see also the simplified sketch of the inclusion pair, bottom left corner) and a separate elongated mchr inclusion. The larger crystal is principally cuboctahedral in shape, and both mchr inclusions are deep cherry red. The colourless olivine inclusion is attached to the larger mchr crystal, as shown. Photograph from Fabrizio Nestola's lab.

Thermo-/oxybarometric analysis of the inclusion pair determined the $P$–$T$–$fO_2$ conditions at the time of its entrapment in the host diamond, and from this result, the physical conditions under which the crystallization of Oli-CHR1 diamond occurred could be inferred, and

additionally information about the redox state of this portion of the Siberian craton at the time of diamond formation could be provided. Our knowledge of the redox and thermal state of the mantle under Udachnaya largely relies on data obtained from mantle xenoliths in the kimberlite (Ionov et al., 2010; Goncharov et al., 2012; Yaxley et al., 2012; Doucet et al., 2013; Miller et al., 2016; Liu et al., 2022). These data are supposed to constrain the physical-chemical conditions of the cratonic mantle at the time of kimberlite eruption (360 ± 7 Ma, Kinny et al., 1997), but do not generally probe the redox state of the Siberian craton at an early stage of its geological history. Despite the age of our diamond being unknown, previous geochronological work on Udachnaya diamonds has suggested two major peaks of diamond formation, dated to 3.5–3.1 Ga and ~2 Ga (Richardson and Harris, 1997; Pearson et al., 1999a, 1999b), although slightly younger ages, 1.8(5) Ga, were also obtained (Wiggers de Vries et al., 2013). Therefore, the $fO_2$ recorded by inclusions in Udachnaya diamonds allows the earlier redox state of the source mantle to be evaluated. By comparing $fO_2$ for this inclusion pair with those of xenoliths from the same depth (ca. 180 km), we will place constraints on the redox state evolution of the Siberian cratonic lithosphere from diamond formation to kimberlite eruption. The determined $fO_2$ for our inclusion pair also establishes a direct link to the redox conditions for diamond formation in the lithospheric mantle, and will be compared with theoretical predictions based on thermodynamic modelling of CHO fluids (Luth and Stachel, 2014).

## 3.2 Experimental approach

In this work, an in situ characterization of the inclusion chemical composition was carried out by using non-destructive techniques. The sample (see Figure 3.1) was analysed by (i) energy-domain synchrotron Mössbauer spectroscopy (SMS) and (ii) single-crystal X-ray diffraction (SCXRD).

### 3.2.1 Synchrotron Mössbauer spectroscopy

The SMS measurements were conducted at the nuclear resonance beamline ID18 (Rüffer and Chumakov, 1996) at the European Synchrotron Radiation Facility (ESRF), Grenoble, during operation in multibunch mode (7/8 + 1 filling). This source provides $^{57}$Fe resonant radiation at 14.4 keV within a bandwidth of 15 neV which is tuneable in energy over a range of ± 0.6 μeV (i.e. ± 12 mm $s^{-1}$) (Potapkin et al., 2012). The X-ray beam emitted by the SMS was focused to a 16 vertical x 15 horizontal μm spot size using Kirkpatrick-Baez mirrors. Before and after sample measurement, the SMS linewidth was controlled using a

$K_2Mg^{57}Fe(CN)_6$ reference single-line absorber. The velocity scale (± 5 mm $s^{-1}$) was calibrated relative to a 25μm thick natural α-Fe foil. For locating the inclusion in the X-ray beam, the dedicated experimental protocol described in Nestola et al. (2016) was followed. The acquired spectrum was fitted with a full transmission integral and a normalized Lorentzian-squared source line shape, using the software package MossA (Prescher et al., 2012). A linear function was applied to model the background.

### 3.2.2 Single-crystal X-ray diffraction

The SCXRD measurements for both minerals were conducted at the Department of Geosciences, University of Padua, with a Rigaku Oxford Diffraction SuperNova diffractometer, equipped with a Mo-target X-ray micro-source operating at 50 kV and 0.8 mA, and a PILATUS 200 K Dectris hybrid pixel array detector (HPAD). The sample-to-detector distance was 68 mm, and the X-ray beam size was 0.12 mm. Data reduction was performed using the CrysAlisPro software (Rigaku Oxford Diffraction, version 40.64.67a), which allows the integration of the measured intensities and applies corrections for Lorentz-polarization effects. Unit-cell parameters along with information related to data collection and refinement details (see below) are reported in Table 3.1.

**Table 3.1.** Unit-cell parameters, data collection information and refinement details for the touching olivine and mchr inclusion in the studied diamond. Note the remarkable agreement factors of the determined crystal structures of both the olivine ($R1\%$ = 3.2 %) and mchr ($R1\%$ = 2.1 %) inclusions.

| | **Olivine** | **mchr** |
|---|---|---|
| **a (Å)** | 4.7615(2) | 8.33274(6) |
| **b (Å)** | 10.2003(3) | |
| **c (Å)** | 5.9934(2) | |
| **V (Å$^3$)** | 291.092(18) | 578.580(12) |
| **Space group** | *Pbnm* | *Fd-3m* |
| **Measured reflections** | 49005 | 24470 |
| **Unique reflections** | 1627 | 180 |
| **Reflections with Fo > 4σ(Fo)** | 1432 | 180 |
| ***R*1 %** | 3.2 | 2.1 |
| ***GooF* (goodness of fit)** | 1.07 | 1.22 |

## 3.3 Results

### 3.3.1 Synchrotron Mössbauer spectroscopy

The resulting spectral model for the mchr (Figure 3.2) shows three doublets with equal relative peak widths and areas: two are assigned to tetrahedrally coordinated $Fe^{2+}$ and the

remaining one to octahedrally coordinated $Fe^{3+}$. This result indicates a typically ordered distribution of $Fe^{2+}$ and $Fe^{3+}$ in the chromite, consistent with current crystal-chemical models (see Li et al., 2002). The spectral model for the olivine (e.g., Canil and O'Neill, 1996) includes two doublets related to the two octahedrally coordinated $Fe^{2+}$ in the non-equivalent M1 and M2 sites, there being negligible or no $Fe^{3+}$ content. However, only one doublet with equal relative peak widths and areas can be used to fit the olivine spectrum (e.g., Dyar et al., 2006) (Figure 3.2).

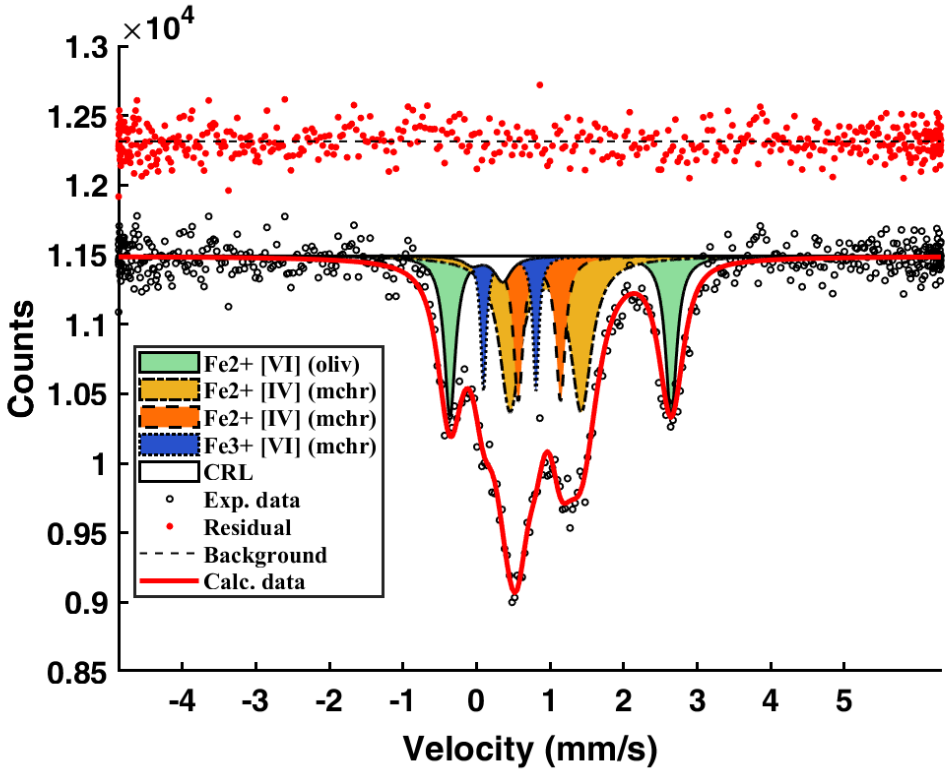


**Figure 3.2.** Energy-domain SMS spectrum of the studied mchr-olivine inclusion pair showing the contribution of both crystals. $Fe^{2+}$ [VI] (oliv) denotes octahedrally coordinated $Fe^{2+}$ in olivine; $Fe^{2+}$ [IV] (mchr) denotes tetrahedrally coordinated $Fe^{2+}$ in mchr; $Fe^{3+}$ [VI] (mchr) denotes octahedrally coordinated $Fe^{3+}$ in mchr; CRL denotes compound refractive lens; Exp. data denotes experimental data; Calc. data denotes calculated data. Total absorption ~22 %.

Also shown in Figure 3.2 is the low-velocity component represented by the compound refractive lens (CRL), which is used to decrease the divergence of the beam incident to the synchrotron Mössbauer source (Potapkin et al., 2012). As it contains some iron, CRL hyperfine parameters (known from independent measurements) are accounted for in the SMS spectrum. Hyperfine parameters obtained for each specific iron structural site are reported in Table 3.2.

**Table 3.2.** Hyperfine parameters determined from the fitting of the SMS spectrum. CS (mm $s^{-1}$) denotes centre shift; QS (mm $s^{-1}$) denotes quadrupole splitting; FWHM denotes full width half maximum; $Fe^{2+}$ [VI] denotes octahedrally coordinated $Fe^{2+}$; $Fe^{2+}$ [IV] denotes tetrahedrally coordinated $Fe^{2+}$; $Fe^{3+}$ [VI] denotes octahedrally coordinated $Fe^{3+}$; CRL denotes compound refractive lens.

| Phase | Component | CS (mm/s) | QS (mm/s) | Area (%) | FWHM | $Fe^{3+}/\sum Fe$ |
|---|---|---|---|---|---|---|
| **Olivine** | $Fe^{2+}$ [VI] | 1.14(1) | 3.01(3) | 24(6) | 0.18(5) | - |
| | $Fe^{2+}$ [IV] | 0.94(3) | 0.97(10) | 43(10) | 0.34(9) | |
| **Mchr** | $Fe^{2+}$ [IV] | 0.85(4) | 0.57(8) | 18(13) | 0.2(1) | 0.15(2) |
| | $Fe^{3+}$ [VI] | 0.45(4) | 0.71(6) | 11(5) | 0.1(1) | |
| **CRL** | - | 0.15 | 0.41 | 4 | 0.27 | |

## 3.3.2 Single-crystal X-ray diffraction

Structure refinement was performed using the SHELX program in the WinGX package (Farrugia, 2012; Sheldrick, 2015) in the *Fd-3m* space group for mchr and *Pbnm* space group for olivine, starting from published atomic coordinates (Nestola et al., 2019, 2011). CIF files with full refinement details are available in the Supplement. Ionic scattering curves were taken from the International Tables for X-ray Crystallography (Wilson, 1995), and anisotropic thermal parameters were refined for all atoms following Angel and Nestola (2016). The cationic distribution at the two different crystallographic sites for each inclusion was indirectly retrieved by refining the site occupancy factor of these sites (see Nestola et al., 2011, for a detailed review).

For olivine, this yielded the chemical composition $(Mg^{2+}_{0.925(2)}Fe^{2+}_{0.075(2)})_2SiO_4$, corresponding to $Fo_{92.5}$. Possible contributions from Ca, Ni, Ti, Mn, Na, Cr and K were not considered, as these elements altogether typically account for ca. 0.01 atoms per unit formula (a.p.f.u.) in mantle olivines. For example, based on 831 reviewed samples of olivine inclusions in diamonds, Stachel and Harris (2008) showed the typical content of Ni was ca. 0.007 a.p.f.u., and the total content of other minor elements amounted to a negligible average of 0.007 a.p.f.u. The chemical composition determined is well within the compositional field for olivine inclusions in diamond from Russian (Yakutian) kimberlites ($Fo_{91}$ to $Fo_{94}$; Sobolev et al., 2009).

The mchr has a more complex crystal chemistry than olivine and is expected to host $Mg^{2+}$ and $Fe^{2+}$ in the tetrahedral site and $Cr^{3+}$, $Al^{3+}$, $Fe^{3+}$ and, among others, traces of $Ti^{4+}$ in the octahedral site. In this study, the cation distribution at the tetrahedral site was retrieved by refining the site occupancy factor, but for the octahedral site, the $Fe^{3+}$ content was calculated from the synchrotron Mössbauer $Fe^{3+}/\sum Fe$ ratio. The $Ti^{4+}$ content was fixed to 0.004 a.p.f.u,

which corresponds to the average of 815 reviewed samples of mchr inclusions in diamonds (Stachel and Harris, 2008); this value well defines an average $Ti^{4+}$ content of mchr specifically from Yakutian diamonds (Sobolev et al., 2004). Finally, $Cr^{3+}$ and $Al^{3+}$ were calculated by refining the site occupancy factor. These calculations yielded the formula $(Mg^{2+}_{0.58(1)}Fe^{2+}_{0.42(1)})(Cr^{3+}_{1.75(3)}Al^{3+}_{0.17(3)}Fe^{3+}_{0.074(12)}Ti^{4+}_{0.004(7)})O_4$. If $Ti^{4+}$ is varied within 1 standard deviation, according to Stachel and Harris (2008), the corresponding variations in $Cr^{3+}$ and $Al^{3+}$ contents are less than 0.005 a.p.f.u. (i.e., largely within their uncertainty). Even though minor elements other than $Ti^{4+}$ were not considered, the calculated chemical composition is well within the compositional field of mchr from Yakutian diamonds reported in Sobolev et al. (2004). Cation distribution for the different crystallographic sites for both inclusions are reported in Table 3.3.

**Table 3.3.** Cation distribution at each crystallographic site for the touching olivine and mchr inclusion in the studied diamond.

| **Mg and Fe cation distribution at olivine M2 and M1 sites** | | **$Fe^{3+}/\sum Fe$ of mchr** | **Mg, Fe, Cr, Al and Ti cation distribution at mchr IV and VI sites** | | |
|---|---|---|---|---|---|
| **M2 site** | **M1 site** | | **IV site** | **VI site** | |
| $Mg^{2+}$ = 0.930(3) | $Mg^{2+}$ = 0.921(3) | 0.15(2) | $Mg^{2+}$ = 0.58(1) | $Cr^{3+}$ = 1.75(3) | $Fe^{3+}$ = 0.074(12) |
| $Fe^{2+}$ = 0.070(2) | $Fe^{2+}$ = 0.079(2) | | $Fe^{2+}$ = 0.42(1) | $Al^{3+}$ = 0.17(3) | $Ti^{4+}$ = 0.004(7) |

# 3.4 Discussion

## 3.4.1 Thermobarometric analysis of the inclusion pair and thermal state of the mantle

The strong dependence of $fO_2$ on temperature and pressure means that thermobarometric data are required to convert $Fe^{3+}/\sum Fe$ ratios and mineral chemical compositions into $fO_2$ values. Whilst several thermometers are available for temperature estimates of mantle samples (e.g., Brey and Kohler, 1990; Ryan et al., 1996; Taylor, 1998; Nimis and Grutter, 2010), comparatively few barometers are available for assessing pressures. This disparity is further exacerbated in mineral assemblages involving spinel, for which geobarometers are particularly limited.

In this study, the Ballhaus et al. (1991) olivine-spinel thermometer was used to calculate the last equilibration temperature of the mchr-olivine pair. Due to the slight dependence of this thermometer on pressure, values in the range 3.5 to 6 GPa were used as input for the thermometric calculations. Accordingly, the calculated temperatures varied between ca. 980

and 1020 °C (with an estimated error of ± 50 °C). These temperatures do not necessarily indicate the conditions of diamond formation, because touching inclusions may re-equilibrate during long-term mantle storage (e.g., Phillips et al., 2004; Stachel and Harris, 2008; Stachel and Luth, 2015; Viljoen et al., 2018).

With the present inclusion pair, an estimate of the entrapment pressure cannot be directly made from its chemical composition because there are no suitable geobarometers for coexisting olivine and mchr. However, assuming negligible vertical movement of the diamond in the rigid cratonic lithosphere, an approximate estimate of the entrapment pressure can be obtained by projecting thermometric estimates for the inclusion pair onto the local xenolith geotherm (Korolev et al., 2018; Nimis et al., 2020). Studies of mantle xenoliths from the Udachnaya kimberlite (Ionov et al., 2010; Goncharov et al., 2012; Yaxley et al., 2012; Doucet et al., 2013; Miller et al., 2016; Liu et al., 2022) indicate a deep lithospheric root (~230 km), but show a relatively large range of geothermal gradients, spanning between the 35 and 40 mW/m$^2$ model conductive geotherms of Hasterok and Chapman (2011) (see Figure 3.3). To account for this geotherm range, Griffin et al. (1996) suggested that the mantle beneath Udachnaya initially experienced cold conditions as testified by ca. 35 mW/m$^2$-equilibrated xenoliths (Figure 3.3), but was later affected by thermal perturbations which raised the temperature of the mantle locally, especially in the deeper parts. Griffin et al. (1996) and earlier researchers (Pokhilenko et al., 1991, 1993) also noted a correlation between xenolith grain size and thermal conditions, with the fine-grained and sheared peridotite xenoliths recording higher temperatures (a feature which is commonly observed also in other cratons, e.g., Woodland and Koch, 2003), whereas the coarse-grained and megacrystalline peridotite xenoliths largely recorded lower *T* values falling close to a ca. 35 mW/m$^2$ conductive geotherm. Liu et al. (2022) showed that heating and deformation in the deep lithospheric portion were variable, not strictly concurrent, and likely controlled by local, small-scale processes. Pokhilenko et al. (1991, 1993) proposed that megacrystalline peridotite xenoliths constituted the principal host rocks of Siberian diamonds and, by extension, that the formation and storage of diamonds occurred under cold conditions consistent with a 35 mW/m$^2$ conductive geotherm. Further evidence for an old, cold conductive geotherm was provided by Nestola et al. (2019), who estimated, based on elastic geobarometry and nitrogen thermometry, the *P–T* formation conditions for a mchr-bearing diamond from Udachnaya to be 6.5(0.2) GPa and 1125(32)–1140(33) °C. These conditions fall right on the 35-mW/m$^2$ geotherm (Figure 3.3), consistent with the establishment of a cold geothermal gradient over the whole Udachnaya lithosphere at the time of diamond formation. Considering the ages of diamonds at Udachnaya (3.5–3.1 Ga, ~2 and ~1.8 Ga,

Richardson and Harris, 1997; Pearson et al., 1999a, 1999b; Wiggers de Vries et al., 2013), these cold conditions persisted for billions of years in some portions of the Udachnaya lithosphere, particularly in the 140–190 km depth interval (Liu et al., 2022). Based on these lines of evidence, our diamond Oli-CHR1 also most likely formed and equilibrated under conditions close to a 35 mW/m$^2$ geotherm. Projection of the thermometric estimates for diamond Oli-CHR1 on this geotherm (Figure 3.3) yields formation conditions of $P$ ~5.7(0.4) GPa and $T$ ~1015(50) °C, that are within the largely unperturbed depth interval (Liu et al., 2022). These results are fairly consistent with thermodynamic modelling in multicomponent, natural peridotitic systems (Ziberna et al., 2013), which predicts that in very depleted (highly refractory) harzburgite with bulk Cr# = 0.32 and along a 35 mW/m$^2$ geotherm, spinel is stable up to 5.5 GPa and 1000 °C, where it reaches a Cr#$_{spinel}$ of ca. 0.9, similar to that of mchr in the Oli-CHR1 diamond.

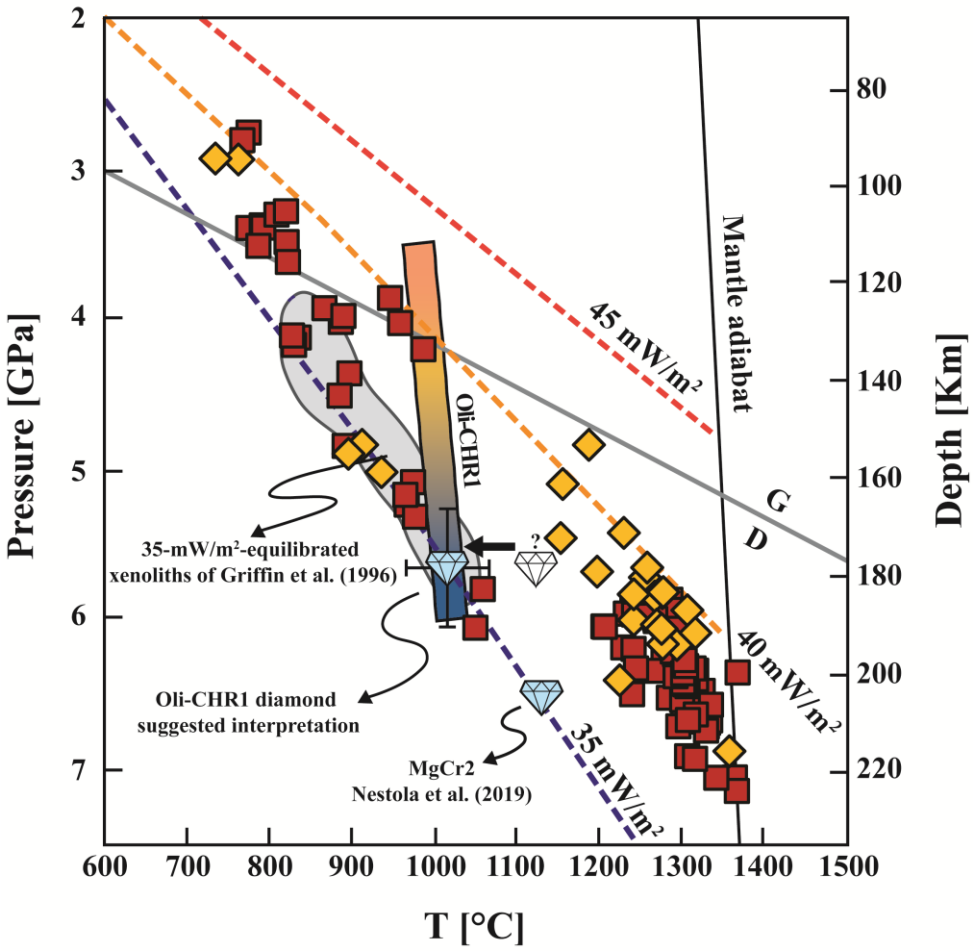


**Figure 3.3.** Pressure-temperature diagram showing the distribution of well-equilibrated mantle xenoliths from Udachnaya kimberlite (data source: Tables S1-S2). Red squares indicate the most recent *P–T* data from Liu et al. (2022), which include a new suite of garnet peridotite xenoliths as well as literature data (see Table S1); these data are based on a carefully selected set of well-equilibrated samples and robust thermobarometers. Yellow rhombi show the data from Goncharov et al. (2012) and Yaxley et al. (2012), for which robust *P–T* estimates were re-determined following

(*Continued*) Liu et al. (2022) (see Table S2). *P–T* conditions for the MgCr2 diamond-mchr pair from Nestola et al. (2019) and 35 mW/m$^2$-equilibrated xenoliths from Griffin et al. (1996, and references therein) are also reported. The gradient bar indicates the *P–T* equilibration curve (see text) for the studied mchr-olivine inclusion pair; the diamond marker shows the suggested interpretation for our Oli-CHR1 diamond (see text), although entrapment at higher (~100 °C) T and re-equilibration during mantle storage cannot be excluded a priori. The 35, 40, and 45 mW/m$^2$ conductive geotherms for the lithospheric mantle and the 1300 °C mantle adiabat are from Hasterok and Chapman (2011), the graphite-diamond (G-D) transition is from Day (2012).

Therefore, we propose that the inclusion pair did not experience any significant thermal perturbations and did not re-equilibrate after incorporation (Figure 3.3), hence it records the *P–T* conditions of the ambient cratonic mantle at the time of its entrapment by the host diamond. Although the evidence presented above and the data reported in the literature suggest that this is the most reasonable scenario, we are aware that available age constraints suggest multi-stage diamond formation beneath Udachnaya. Consequently, if Oli-CHR1 and the diamond investigated by Nestola et al. (2019) have different ages, this implies that they may not necessarily have formed under the same geothermal gradient. An important aspect linked to different diamond ages is secular cooling of the cratonic lithosphere, which is supported both by thermal models for the formation of the cratonic roots (e.g., Michaut et al., 2009) and by the temporal change in reconstructed geotherms from xenoliths found in Proterozoic kimberlites (Grütter, 2009). Further corroborating evidence for secular lithosphere cooling has been found in comparative studies of non-touching and touching inclusions (e.g., Phillips et al., 2004; Stachel et al., 2022). Such data show that touching inclusions generally record lower average temperatures (~100 °C less) than non-touching inclusions, and this is attributed to re-equilibration in a cooling mantle until the time of eruption. However, in other cases no discrepancy exists, suggesting that diamonds formed when the lithospheric mantle had already attained a thermal regime comparable to or even colder than that existing at the time of emplacement of the host kimberlite or lamproite (Nimis, 2002). Considering all these uncertainties, we will also address a scenario in which our inclusion pair was trapped at a ~100 °C higher temperature, i.e., ~1115 °C, and eventually re-equilibrated to ~1015 °C during long-term mantle storage (Figure 3.3). To provide any meaningful inference, such as calculating the $fO_2$ for the inclusion pair (see next section), the chemical compositions of olivine and mchr, and specifically their Fe/(Fe + Mg) ratios, have to be recalculated to 1115 °C. This can be done by means of the Ballhaus et al. (1991) olivine-spinel exchange thermometer, using a trial-and-error procedure. Considering that the olivine inclusion is much smaller than the mchr inclusion, the Mg-$Fe^{2+}$ exchange between the two inclusions would have mostly modified the olivine composition, while that

of the mchr would have remained approximately constant. Accordingly, the back-calculated compositions yield $\chi$Mg ~0.909 and $\chi$Fe ~0.091 in olivine and $\chi$Mg ~0.582 and $\chi Fe^{2+}$ ~0.418 in mchr. With respect to the entrapment pressure, we will assume it to be 5.7(1.0) GPa, the larger uncertainty being related to the uncertainties in the geothermal gradient.

### 3.4.2 $fO_2$ analysis of the inclusion pair and oxidation state of the mantle

Oxygen fugacity in cratonic mantle has been mostly explored using xenoliths from the Kaapvaal craton in South Africa (Woodland and Koch, 2003; Creighton et al., 2009; Lazarov et al., 2009), the Slave craton in northern Canada (McCammon and Kopylova, 2004; Creighton et al., 2010) and the Siberian craton (e.g., Ashchepkov et al., 2014, 2016). These studies showed that $fO_2$ is close to the fayalite-magnetite-quartz (FMQ) buffer at the top of the lithospheric mantle and progressively decreases with increasing depth. These data also showed that $fO_2$ exhibits important lateral variations, which are commonly attributed to either melt extraction or oxidation/reduction induced by fluid or melt-driven metasomatism. Oxybarometric data for mantle peridotite xenoliths from the Udachnaya kimberlite (Goncharov et al., 2012; Yaxley et al., 2012; Miller et al., 2016; Table S2 in the Supplement) also show this global trend with progressively lower $\Delta\log fO_2$ (FMQ) values ($\Delta$FMQ $\simeq$ –1 to $\simeq$ –3, excluding outliers) with increasing depths (Figure 3.4). Most of the xenoliths equilibrated at $P$ > 3.5 GPa, i.e., beyond the graphite-diamond (G-D) transition, and at oxygen fugacity conditions more reduced than the enstatite-magnesite-olivine-diamond (EMOD) buffer. The EMOD buffer marks the highest oxygen fugacity at which diamonds could form and be preserved within carbonated peridotite assemblages. For calculating $\Delta\log fO_2$ (FMQ) values for our inclusion pair, the two available calibrations are from Ballhaus et al. (1991) (hereafter, B91) and Nikolaev et al. (2016) (hereafter, N16), both sharing the same formalism. The N16 calibration is a revision of the B91 oxybarometer based on independent experimental data and inherits much from the previous work. Here, $\Delta\log fO_2$ (FMQ) values for our inclusion pair were calculated using both the B91 and the N16 calibrations. Results for our preferred model, i.e., entrapment of the pair at $P$ ~5.7(0.4) GPa and $T$ ~1015(50) °C without re-equilibration after incorporation, gave $\Delta\log fO_2$ (FMQ) values of –1.4(0.8) and –1.0(0.5), respectively, whereas we obtained –1.7(0.8) and –1.6(0.5) for the scenario in which the inclusions were trapped at higher $T$, ~1115(50) °C, and $P$ ~5.7(1.0) GPa (Figure 3.4). The uncertainties in the calculated $fO_2$ values reported here are the nominal uncertainties for the two calibrations used. However, we are aware that our estimated chemical compositions derived from X-ray diffraction site occupancies are certainly affected by larger uncertainties than those obtained through standard electron microprobe analysis.

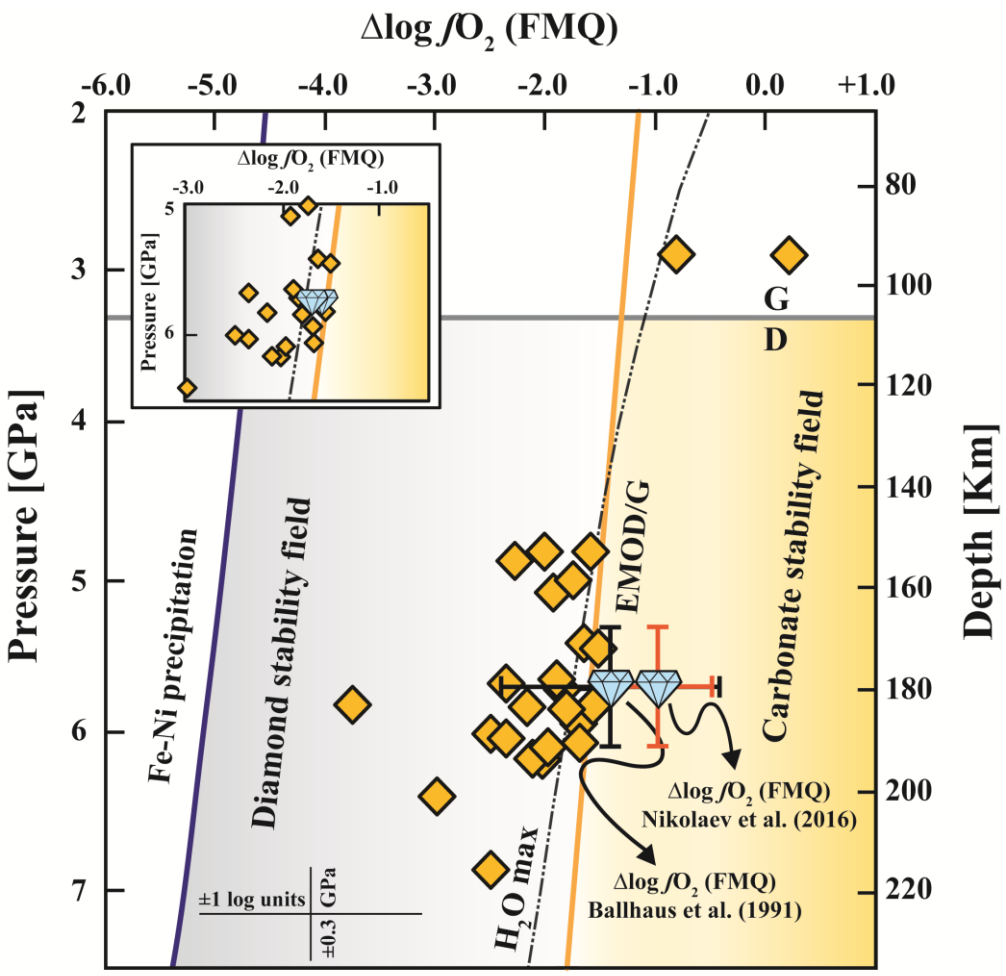


**Figure 3.4.** Δlog $fO_2$ (FMQ) – pressure diagram showing the distribution of well-equilibrated xenoliths from Udachnaya (yellow rhombi) (data source: Table S2) and the calculated Δlog $fO_2$ (FMQ) value for the studied inclusion pair (diamond). Δlog $fO_2$ (FMQ) values and associated uncertainties for mantle xenoliths were calculated with the Miller et al. (2016) oxybarometer (see Table S2); typical uncertainties are shown for reference. Inset: the same data but assuming that the inclusion was trapped at ~100 °C higher $T$ and then re-equilibrated during long-term mantle storage. Δlog $fO_2$ (FMQ) values calculated for the inclusion pair suggest diamond formation at relatively oxidized conditions near the EMOD buffer, both for the scenarios in which the inclusion did not re-equilibrate after incorporation or was trapped at higher $T$. EMOD/G buffer is calculated for a 35 mW/m$^2$ geotherm from the thermodynamic dataset of Holland and Powell (2011) (see Luth and Stachel, 2014, their Appendix 1), the Fe-Ni precipitation curve is from O'Neill and Wall (1987), the graphite-diamond (G-D) transition is from Day (2012) based on a 35mW/m$^2$ geotherm, the water maximum curve (labelled '$H_2O$ max') is calculated for a 35 mW/m$^2$ geotherm using the using the GFluid model of Zhang and Duan (2010).

To evaluate the uncertainties in the calculated $fO_2$ values which solely derive from the input parameters (i.e., statistical errors in site occupancy factors refined from SCXRD and in the $Fe^{3+}/\sum Fe$ ratio obtained from the SMS, and estimated errors in thermobarometry), we applied a Gaussian error propagation function taking into account all possible error sources. In the case of entrapment of the pair at $P$ ~5.7(0.4) GPa and $T$ ~1015(50) °C, error propagation for both calibrations yielded ± 0.3 log units. Of all error sources, the most critical

one appears to be the uncertainty in the $Fe^{3+}/\sum Fe$ ratio of mchr, which already propagates ca. ± 0.3 log units on the final $fO_2$ estimate for both calibrations. If the input $T$ is changed by ± 50 °C and $P$ by ± 0.4 GPa (i.e., the $P$–$T$ estimate is moved within uncertainties along the 35 mW/m$^2$ geotherm), the $fO_2$ change is only ± 0.1 log units for the B91 calibration and ± 0.2 log units for the N16 calibration. In the case of post entrapment re-equilibration, an allowance for a larger pressure uncertainty (± 1 GPa, due to the uncertainties in the geothermal gradient) has to be made and then taken into account with all the other possible error sources. This yielded ± 0.4 log units for both calibrations. The small total uncertainty (± 0.3–0.4 log units) deriving from all possible uncertainties in the input parameters is well within the nominal uncertainty in the two oxybarometer calibrations (i.e., ± 0.8 log units for B91 and ± 0.5 log units for N16). Additional errors probably derive from the extrapolation of both oxybarometers outside their calibration ranges (i.e., 0.3–2.7 GPa for B91 and 0.0001–2.5 GPa for N16), but these errors are difficult to estimate. Although we recognize that the extrapolation of the B91 and N16 oxybarometers at higher pressures will likely introduce further errors, the most critical issue in both cases was claimed to be the application of the corresponding formulation to some specific settings. In the case of the B91 oxybarometer, the authors advised caution when applying it to orthopyroxene-undersaturated systems, or where $Cr^{2+}$ may partially substitute in spinel, while its application to a suite of high-pressure spinels from the Archean cratonic lithosphere gave logical results (Ballhaus, 1993). Ballhaus et al. (1991) have already pointed out that the correction for orthopyroxene-undersaturated rocks rarely exceeds –0.2 log units, which falls largely within the error of the model, while significant $Cr^{2+}$ substitution in spinel may only occur at relatively low oxygen fugacity. In the case of the N16 oxybarometer, the authors warranted caution when applying their oxybarometer to intrusive cumulus rocks, which however is not relevant in our case.

Figure 3.4 also shows that the EMOD line, calculated for a 35 mW/m$^2$ geotherm, varies between about ΔFMQ –1.2 and –1.8 in the pressure interval 2–7 GPa. While $\Delta\log fO_2$ (FMQ) (B91) values of –1.4(0.8) and –1.7(0.8) are close to that of the EMOD line and fall, within error, in the diamond stability field, only the $\Delta\log fO_2$ (FMQ) (N16) of –1.6(0.5) is compatible with diamond (scenario of post-entrapment re-equilibration for the inclusion), while –1.0(0.5) is more oxidized than the EMOD line values. Nonetheless, considering all possible uncertainties, both the B91 and the N16 estimates point to relatively oxidized redox conditions comparable to, or slightly more oxidized than, those of xenoliths from the same depth (Figure 3.4, Table S2 in the Supplement), regardless of the assumed scenario. The calculated $\Delta\log fO_2$ (FMQ) values for our inclusion pair are also found to be good indicators

of the $fO_2$ conditions of diamond formation. In fact, resetting of $fO_2$ in mantle rocks may be effective and fast, given the very limited oxygen buffering capacity of depleted cratonic peridotites (Luth and Stachel, 2014; Stachel and Luth, 2015). How efficiently the $fO_2$ of inclusions in diamond is reset during entrapment processes will depend on the time needed for diamond formation. Although the time required for a diamond to form in Earth's mantle is poorly known, evidence from natural diamonds and diamond growth studies suggest that this time may be geologically long. For example, monocrystalline diamonds reveal episodic growth and resorption features, indicating the presence of fluid over several millions of years (Gress et al., 2018). Experimental studies show that diamonds may grow efficiently in the presence of water and within the timescale of the experiments (e.g., Sokol and Pal'yanov, 2008; Sokol et al., 2009; Bureau et al., 2016), which were however conducted at temperatures well above those of the subcratonic lithosphere. Hence, although the time spans required for individual growth episodes and, therefore, for encapsulation of an inclusion are shorter, they are likely to be sufficiently long to allow $fO_2$ resetting of the inclusion during its incorporation in the growing diamond. Based on this evidence, the inclusion pair shall record $fO_2$ conditions of diamond formation, regardless of its syngenetic or protogenetic origin (cf. Nestola et al., 2014; Nimis et al., 2019). Hence, both the B91 and the N16 estimates suggest relatively oxidized conditions for diamond formation, probably falling near the upper limit for diamond stability in peridotite.

### 3.4.3 Implications for the redox state evolution and diamond formation

Archean and early Proterozoic cratons are stable regions of continental rocks with basement ages of at least 2.5 Ga (e.g., de Wit and Hart, 1993), which preserve the oldest bodies of Earth's lithosphere and contain an extensive record of its ancient history. In this context, mantle xenoliths and inclusion-bearing diamonds hosted in kimberlites are the only known direct samples of the basal lithosphere, which can deliver rare information on the nature of the lithospheric mantle and a unique perspective on the processes, conditions and evolution of the craton (Pearson and Wittig, 2014).

While the paleo-redox state of the convecting mantle has been investigated by many researchers (e.g., Canil, 2002; Li and Lee, 2004; Aulbach and Stagno, 2016; Nicklas et al., 2019; O'Neill and Aulbach, 2022; Gao et al., 2022), suggesting a statistically significant secular increase in the mantle $fO_2$ across the Archean-Proterozoic boundary, the oxygen fugacity evolution of the cratonic lithosphere has been less explored. It is well accepted that the cratonic mantle has formed by extensive melt extraction during the Archean, which left highly refractory and reducing residua because of the incompatibility of $Fe^{3+}$ during melting

(Frost and McCammon, 2008). This was later followed by percolation of oxidizing melts/fluids that metasomatized most of the lithospheric mantle and increased its $fO_2$ over time (e.g., Foley, 2011; Foley and Fischer, 2017). However, gauging the timing of these process is difficult because cratonic xenoliths remained open systems until the time of their entrainment in the host kimberlite. In contrast, once formed, diamonds are chemically inert containers for inclusions, which are protected from alteration/re-equilibration processes with the surrounding mantle. Therefore, the concurrent occurrence of both inclusions in diamonds, with presumably old ages, and xenoliths from the same locality allows the redox state evolution of the cratonic mantle to be unravelled.

The oxygen fugacities recorded by mantle xenoliths from Udachnaya constrain the physical-chemical conditions of the cratonic mantle at the time of xenolith entrainment in the host kimberlite (360 ± 7 Ma, Kinny et al., 1997). In contrast, the inclusion pair last equilibrated with the surrounding mantle before being encapsulated in its host diamond. Although the age of our diamond is unknown, diamonds from Udachnaya have been dated to 3.5–3.1 Ga, ~2 and ~1.8 Ga (Richardson and Harris, 1997; Pearson et al., 1999a, 1999b; Wiggers de Vries et al., 2013), which means that the inclusion of our diamond reflects an earlier state of the cratonic lithosphere. Considering this difference in time, the similarity between $\Delta\log fO_2$ (FMQ) values for mantle xenoliths from the Udachnaya kimberlite and the inclusion pair studied in this work (Figure 3.4) describes a scenario in which the modern redox state of the cratonic lithosphere below Udachnaya would have likely been attained relatively early after its formation. Although the cratonic mantle has been the sink for metasomatic fluids/melts which could certainly change its redox conditions (e.g., Foley, 2011), our determination suggests that the modern redox state of this portion of the Siberian craton, once set, may have persisted for billions of years, at least at the local scale. This also agrees with evidence from multicomponent carbon isotope modelling data coupled with the prominent mode in $\delta^{13}C$ values for diamonds worldwide at about –5 ± 1‰, which indicate that this range can be accounted for by a variation in $fO_2$ of only 0.4 log units (Howell et al., 2020; Stachel et al., 2017), implying a near-constant $fO_2$ through time for the mantle from which these fluids derived. Corroborating evidence was also recently observed from a comparative study of worldwide inclusions in eclogitic diamonds and eclogite xenoliths showing no systematic changes in the $fO_2$ of the cratonic eclogite reservoir subsequent to diamond formation (Aulbach and Stachel, 2022), although the extrapolation of these findings to the dominant peridotite lithology should be treated with care, in the context of its poorer oxygen buffering capacity (Luth and Stachel, 2014).

It was also recently proposed that due to the very limited oxygen buffering capacity of depleted cratonic peridotites, diamond formation in peridotites is unlikely related to rock-buffered redox reactions (Luth and Stachel, 2014; Stachel and Luth, 2015; Stachel et al., 2017). These works indicate that small amounts of $O_2$ (less than 200 ppm) are required to shift a peridotite from the IW (iron-wüstite) to the EMOD buffer, implying that peridotites have virtually no ability to act as a source or sink for $O_2$ and that their oxidation state can be employed as a faithful indicator of the redox state of the last interacting metasomatic fluid. This may also apply to inclusions in diamonds, as their $fO_2$ is probably efficiently reset during entrapment processes (see above). Based on the poor redox buffering capacity of cratonic peridotites, Luth and Stachel (2014) have suggested that isochemical precipitation of carbon from CHO fluids under subsolidus mantle conditions may provide an efficient mode for diamond formation, especially in refractory (harzburgitic-dunitic) substrates. This would occur in response to either isobaric cooling or combined cooling and decompression as the fluid migrates upwards along a cratonic geothermal gradient. According to these models, this process can be particularly efficient if the fluid speciation is close to the water maximum, $O/(O+H)_{mol}$ ~0.33, implying that low carbon concentrations in the fluid and high fluid/rock ratios are needed to grow diamonds. This takes place at ΔFMQ between about –1 and –2, conditions which lie very close to the EMOD buffer along a cold geotherm (Luth and Stachel, 2014) and are remarkably consistent with the relatively oxidized conditions estimated for our inclusion pair (Figure 3.4). Evidence from experimental work (e.g., Sokol and Pal'yanov, 2008; Sokol et al., 2009; Bureau et al., 2016) also indicates that CHO-fluid-bearing systems at $fO_2$ near the water maximum promote efficient diamond growth. Nimis et al. (2020) further explored the efficiency of diamond formation processes versus depth by combining CHO-fluid modelling with various *P–T* paths for the ascending fluid. Their results further confirm that conditions comparable to the Udachnaya cold geotherm at 5.7 GPa at the water maximum would have good potential for diamond formation. The $fO_2$ estimate for our inclusion pair provides direct evidence of diamond formation under relatively oxidized conditions near the EMOD buffer, i.e., under conditions in which CHO fluids are water-rich.

We are aware that the existence of diamonds with inclusions of methane (e.g., Thomassot et al., 2007; Smit et al., 2016), carbonate or $CO_2$ ( Schrauder and Navon, 1993; Wang et al., 1996) demonstrates that diamond formation may occur over a wide range of oxygen fugacities, in keeping with the record of deep-seated xenoliths (e.g., Yaxley et al., 2017). Although independent evidence from mantle xenoliths and carbon isotope data suggests that very reducing conditions and $CH_4$-rich parent media are not the norm for diamonds (Luth

and Stachel, 2014; Stachel et al., 2017), more data on inclusions in diamonds similar to those provided in this work are required to determine the systematics of $fO_2$ conditions at which diamonds form. These data should ideally be combined with diamond age estimates to unravel the long-term redox state evolution of the cratonic lithospheric mantle.

## 3.5 Summary and conclusions

In this study, we presented the first oxygen fugacity determination of a mchr-olivine touching inclusion pair still trapped in its host diamond from the Paleozoic Udachnaya kimberlite. Thermobarometric analyses and the measured $Fe^{3+}/\Sigma Fe$ ratio in mchr indicate the $P$–$T$–$fO_2$ conditions of the inclusion pair at the time of the entrapment to be ~5.7(0.4) GPa and ~1015(50) °C (although entrapment at higher $T$ and re-equilibration during subsequent mantle storage cannot be excluded) and $fO_2$ near the EMOD buffer. The estimated redox conditions are similar to, or slightly more oxidized than, those of xenoliths from the same depth. However, while the xenoliths last equilibrated with the surrounding mantle before their entrainment in the kimberlite at ~360 Ma, the inclusion pair retains the signature of a mantle as old as 3.5–3.1 Ga, ~2 or ~1.8 Ga, i.e., the known peaks of diamond formation at Udachnaya, corresponding to the time at which the mchr-olivine pair became trapped in its host diamond. Based on the similarity between xenoliths and inclusion $fO_2$ values, we propose that the modern redox state of this portion of the Siberian lithosphere was attained relatively early after its formation and may have persisted for billions of years, at least at the local scale, until the time of kimberlite eruption.

Moreover, the oxygen fugacity determination for our inclusion pair provides the first direct evidence for diamond formation under relatively oxidized conditions. These conditions are consistent with recent models of diamond formation suggesting water-rich CHO fluids as the most likely parents for lithospheric diamonds (Luth and Stachel, 2014).

## Author contribution

LF contributed in terms of conceptualization, methodology, data evaluation and modelling, writing-original draft, writing-review & editing; VC contributed in terms of conceptualization, methodology, writing-review & editing; FN contributed in terms of conceptualization, methodology, writing-review & editing, supervision; PN contributed in terms of data evaluation and modelling, writing-review & editing, supervision; LZ contributed in terms of methodology, writing-review & editing; LP contributed in terms of

writing-review & editing; AC: methodology; JH contributed in terms of resources, writing-review & editing, supervision; MC: writing-review & editing, supervision.

## Acknowledgments

The European Synchrotron Radiation Facility (ESRF) is gratefully acknowledged for the provision of beam time at the ID18 nuclear resonance beamline. Luca Faccincani wishes to thank the beamline staff of ID18 and the ESRF for its traineeship programme for undergraduate students and financial support and acknowledges the Istituto Nazionale di Geofisica e Vulcanologia (INGV) for funding his PhD project (XXXV cycle) with thematic 'Links between rheology, mineralogy and composition of the Earth's mantle'. Luca Ziberna acknowledges the support of the Alexander von Humboldt Foundation. The authors are grateful to Sonja Aulbach and Alexander Sokol for their constructive and fruitful comments, which improved an earlier version of the manuscript. Elisabetta Rampone and Roland Stalder are acknowledged for their careful editorial handling and guidance.

## Financial support

This research has been supported by an ERC Starting Grant (grant no. 307322) to Fabrizio Nestola.

## Appendix A. Supplementary data

The supplement related to this article is available online at https://doi.org/10.5194/jn-10-1-2022-supplement.

## References

Angel, R.J., Nestola, F., 2016. A century of mineral structures: How well do we know them? Am. Mineral. 101, 1036–1045.

Ashchepkov, I.V., Kuligin, S.S., Vladykin, N.V., Downes, H., Vavilov, M.A., Nigmatulina, E.N., Babushkina, S.A., Tychkov, N.S., Khmelnikova, O.S., 2016. Comparison of mantle lithosphere beneath early Triassic kimberlite fields in Siberian craton reconstructed from deep-seated xenocrysts. Geosci. Front. 7, 639–662.

Ashchepkov, I.V., Vladykin, N.N., Ntaflos, T., Kostrovitsky, S.I., Prokopiev, S.A., Downes, H., Smelov, A.P., Agashev, A.M., Logvinova, A.M., Kuligin, S.S., Tychkov, N.S., Salikhov, R.F., Stegnitsky, Y.B., Alymova, N.V., Vavilov, M.A., Minin, V.A., Babushkina, S.A., Ovchinnikov, Y.I., Karpenko, M.A., Tolstov, A.V., Shmarov, G.P., 2014. Layering of the lithospheric mantle beneath the Siberian Craton: Modeling using thermobarometry of mantle xenolith and xenocrysts. Tectonophysics 634, 55–75.

Aulbach, S., Stachel, T., 2022. Evidence for oxygen-conserving diamond formation in redox-buffered subducted oceanic crust sampled as eclogite. Nat. Commun. 13, 1924.
Aulbach, S., Stagno, V., 2016. Evidence for a reducing Archean ambient mantle and its effects on the carbon cycle. Geology 44, 751–754
Ballhaus, C., Berry, R.F., Green, D.H., 1991. High pressure experimental calibration of the olivine-orthopyroxene-spinel oxygen geobarometer: implications for the oxidation state of the upper mantle. Contrib. to Mineral. Petrol. 107, 27–40.
Ballhaus, C., 1993. Redox states of lithospheric and asthenospheric upper mantle, Contrib. Mineral. Petr., 114, 331–348.
Barnes, S.J., Roeder, P.L., 2001. The Range of Spinel Compositions in Terrestrial Mafic and Ultramafic Rocks. J. Petrol. 42, 2279–2302.
Brey, G.P., Kohler, T., 1990. Geothermobarometry in Four-phase Lherzolites II. New Thermobarometers, and Practical Assessment of Existing Thermobarometers. J. Petrol. 31, 1353–1378.
Bulanova, G.P., Walter, M.J., Smith, C.B., Kohn, S.C., Armstrong, L.S., Blundy, J., Gobbo, L., 2010. Mineral inclusions in sublithospheric diamonds from Collier 4 kimberlite pipe, Juina, Brazil: subducted protoliths, carbonated melts and primary kimberlite magmatism. Contrib. to Mineral. Petrol. 160, 489–510.
Bureau, H., Frost, D.J., Bolfan-Casanova, N., Leroy, C., Esteve, I., Cordier, P., 2016. Diamond growth in mantle fluids. Lithos 265, 4–15.
Canil, D., 2002. Vanadium in peridotites, mantle redox and tectonic environments: Archean to present. Earth Planet. Sci. Lett. 195, 75–90.
CANIL, D., O'NEILL, H.S.C., 1996. Distribution of Ferric Iron in some Upper-Mantle Assemblages. J. Petrol. 37, 609–635.
Creighton, S., Stachel, T., Eichenberg, D., Luth, R.W., 2010. Oxidation state of the lithospheric mantle beneath Diavik diamond mine, central Slave craton, NWT, Canada. Contrib. to Mineral. Petrol. 159, 645–657.
Creighton, S., Stachel, T., Matveev, S., Höfer, H., McCammon, C., Luth, R.W., 2009. Oxidation of the Kaapvaal lithospheric mantle driven by metasomatism. Contrib. to Mineral. Petrol. 157, 491–504.
Day, H.W., 2012. A revised diamond-graphite transition curve. Am. Mineral. 97, 52–62.
de Wit, M.J., Hart, R.A., 1993. Earth's earliest continental lithosphere, hydrothermal flux and crustal recycling. Lithos 30, 309–335.
Doucet, L.S., Ionov, D.A., Golovin, A. V, 2013. The origin of coarse garnet peridotites in cratonic lithosphere: new data on xenoliths from the Udachnaya kimberlite, central Siberia. Contrib. to Mineral. Petrol. 165, 1225–1242.
Dyar, M.D., Agresti, D.G., Schaefer, M.W., Grant, C.A., Sklute, E.C., 2006. MÖSSBAUER SPECTROSCOPY OF EARTH AND PLANETARY MATERIALS. Annu. Rev. Earth Planet. Sci. 34, 83–125.
Farrugia, L.J., 2012. WinGX and ORTEP for Windows : an update. J. Appl. Crystallogr. 45, 849–854.
Foley, S.F., 2011. A Reappraisal of Redox Melting in the Earth's Mantle as a Function of Tectonic Setting and Time. J. Petrol. 52, 1363–1391.
Foley, S.F., Fischer, T.P., 2017. An essential role for continental rifts and lithosphere in the deep carbon cycle. Nat. Geosci. 10, 897–902.
Frost, D.J., McCammon, C.A., 2008. The Redox State of Earth's Mantle. Annu. Rev. Earth Planet. Sci. 36, 389–420.
Gao, L., Liu, S., Cawood, P.A., Hu, F., Wang, J., Sun, G., Hu, Y., 2022. Oxidation of Archean upper mantle caused by crustal recycling. Nat. Commun. 13, 3283.
Goncharov, A.G., Ionov, D.A., Doucet, L.S., Pokhilenko, L.N., 2012. Thermal state, oxygen fugacity and C-O-H fluid speciation in cratonic lithospheric mantle: New data on peridotite xenoliths from the Udachnaya kimberlite, Siberia. Earth Planet. Sci. Lett. 357–358, 99–110.

Gress, M.U., Howell, D., Chinn, I.L., Speich, L., Kohn, S.C., van den Heuvel, Q., Schulten, E., Pals, A.S.M., Davies, G.R., 2018. Episodic diamond growth beneath the Kaapvaal Craton at Jwaneng Mine, Botswana. Mineral. Petrol. 112, 219–229.
Griffin, W.L., Kaminsky, F.V., Ryan, C.G., O'Reilly, S.Y., Win, T.T., Ilupin, I.P., 1996. Thermal state and composition of the lithospheric mantle beneath the Daldyn kimberlite field, Yakutia. Tectonophysics 262, 19–33.
Grütter, H.S., 2009. Pyroxene xenocryst geotherms: Techniques and application. Lithos 112, 1167–1178.
Hasterok, D., Chapman, D.S., 2011. Heat production and geotherms for the continental lithosphere. Earth Planet. Sci. Lett. 307, 59–70.
Holland, T.J.B., Powell, R., 2011. An improved and extended internally consistent thermodynamic dataset for phases of petrological interest, involving a new equation of state for solids. J. Metamorph. Geol. 29, 333–383.
Howell, D., Stachel, T., Stern, R.A., Pearson, D.G., Nestola, F., Hardman, M.F., Harris, J.W., Jaques, A.L., Shirey, S.B., Cartigny, P., Smit, K.V., Aulbach, S., Brenker, F.E., Jacob, D.E., Thomassot, E., Walter, M.J., Navon, O., 2020. Deep carbon through time: Earth's diamond record and its implications for carbon cycling and fluid speciation in the mantle. Geochim. Cosmochim. Acta 275, 99–122.
Ionov, D.A., Doucet, L.S., Ashchepkov, I. V, 2010. Composition of the Lithospheric Mantle in the Siberian Craton: New Constraints from Fresh Peridotites in the Udachnaya-East Kimberlite. J. Petrol. 51, 2177–2210.
Jean, M.M., Taylor, L.A., Howarth, G.H., Peslier, A.H., Fedele, L., Bodnar, R.J., Guan, Y., Doucet, L.S., Ionov, D.A., Logvinova, A.M., Golovin, A.V., Sobolev, N.V., 2016. Olivine inclusions in Siberian diamonds and mantle xenoliths: Contrasting water and trace-element contents. Lithos 265, 31–41.
Kaminsky, F., Zakharchenko, O., Davies, R., Griffin, W., Khachatryan-Blinova, G., Shiryaev, A., 2001. Superdeep diamonds from the Juina area, Mato Grosso State, Brazil. Contrib. to Mineral. Petrol. 140, 734–753.
Kinny, P.D., Griffin, B., Heaman, L.M., Brakhfogel, F.F., Spetsius, Z. V, 1997. SHRIMP U-Pb ages of perovskite from Yakutian kimberlites. Geol. I Geofiz. 38, 91–99.
Korolev, N.M., Kopylova, M., Bussweiler, Y., Pearson, D.G., Gurney, J., Davidson, J., 2018. The uniquely high-temperature character of Cullinan diamonds: A signature of the Bushveld mantle plume? Lithos 304–307, 362–373.
Lazarov, M., Woodland, A.B., Brey, G.P., 2009. Thermal state and redox conditions of the Kaapvaal mantle: A study of xenoliths from the Finsch mine, South Africa. Lithos 112, 913–923.
Li, Z.-X.A., Lee, C.-T.A., 2004. The constancy of upper mantle fO2 through time inferred from V/Sc ratios in basalts. Earth Planet. Sci. Lett. 228, 483–493.
Li, Z., Ping, J.Y., Jin, M.Z., Liu, M.L., 2002. Distribution of Fe2+ and Fe3+ and next-nearest neighbour effects in natural chromites: comparison between results of QSD and Lorentzian doublet analysis. Phys. Chem. Miner. 29, 485–494.
Liu, Z., Ionov, D.A., Nimis, P., Xu, Y., He, P., Golovin, A. V., 2022. Thermal and compositional anomalies in a detailed xenolith-based lithospheric mantle profile of the Siberian craton and the origin of seismic midlithosphere discontinuities. Geology 50, 891–896.
Luth, R.W., Stachel, T., 2014. The buffering capacity of lithospheric mantle: implications for diamond formation. Contrib. to Mineral. Petrol. 168, 1083.
McCammon, C., Kopylova, M.G., 2004. A redox profile of the Slave mantle and oxygen fugacity control in the cratonic mantle. Contrib. to Mineral. Petrol. 148, 55–68.
Meyer, H.O.A., 1987. Inclusions in diamond, in: Mantle Xenoliths. John Wiley & Sons, pp. 501–523.

Michaut, C., Jaupart, C., Mareschal, J.-C., 2009. Thermal evolution of cratonic roots. Lithos 109, 47–60.
Miller, W.G.R., Holland, T.J.B., Gibson, S.A., 2016. Garnet and Spinel Oxybarometers: New Internally Consistent Multi-equilibria Models with Applications to the Oxidation State of the Lithospheric Mantle. J. Petrol. 57, 1199–1222.
Nestola, F., Cerantola, V., Milani, S., Anzolini, C., McCammon, C., Novella, D., Kupenko, I., Chumakov, A., Rüffer, R., Harris, J.W., 2016. Synchrotron Mössbauer Source technique for in situ measurement of iron-bearing inclusions in natural diamonds. Lithos 265, 328–333.
Nestola, F., Korolev, N., Kopylova, M., Rotiroti, N., Pearson, D.G., Pamato, M.G., Alvaro, M., Peruzzo, L., Gurney, J.J., Moore, A.E., Davidson, J., 2018. CaSiO3 perovskite in diamond indicates the recycling of oceanic crust into the lower mantle. Nature 555, 237–241.
Nestola, F., Nimis, P., Angel, R.J., Milani, S., Bruno, M., Prencipe, M., Harris, J.W., 2014. Olivine with diamond-imposed morphology included in diamonds. Syngenesis or protogenesis? Int. Geol. Rev. 56, 1658–1667.
Nestola, F., Nimis, P., Ziberna, L., Longo, M., Marzoli, A., Harris, J.W., Manghnani, M.H., Fedortchouk, Y., 2011. First crystal-structure determination of olivine in diamond: Composition and implications for provenance in the Earth's mantle. Earth Planet. Sci. Lett. 305, 249–255.
Nestola, F., Zaffiro, G., Mazzucchelli, M.L., Nimis, P., Andreozzi, G.B., Periotto, B., Princivalle, F., Lenaz, D., Secco, L., Pasqualetto, L., Logvinova, A.M., Sobolev, N. V, Lorenzetti, A., Harris, J.W., 2019. Diamond-inclusion system recording old deep lithosphere conditions at Udachnaya (Siberia). Sci. Rep. 9, 12586.
Nicklas, R.W., Puchtel, I.S., Ash, R.D., Piccoli, P.M., Hanski, E., Nisbet, E.G., Waterton, P., Pearson, D.G., Anbar, A.D., 2019. Secular mantle oxidation across the Archean-Proterozoic boundary: Evidence from V partitioning in komatiites and picrites. Geochim. Cosmochim. Acta 250, 49–75.
Nikolaev, G. S., Ariskin, A. A., Barmina, G. S., Nazarov, M. A., and Almeev, R. R., 2016. Test of the Ballhaus–Berry–Green Ol–Opx–Sp oxybarometer and calibration of a new equation for estimating the redox state of melts saturated with olivine and spinel, Geochem. Int., 54, 301–320.
Nimis, P., 2002. The pressures and temperatures of formation of diamond based on thermobarometry of chromian diopside inclusions. Can. Mineral. 40, 871–884.
Nimis, P., Alvaro, M., Nestola, F., Angel, R.J., Marquardt, K., Rustioni, G., Harris, J.W., Marone, F., 2016. First evidence of hydrous silicic fluid films around solid inclusions in gem-quality diamonds. Lithos 260, 384–389.
Nimis, P., Angel, R.J., Alvaro, M., Nestola, F., Harris, J.W., Casati, N., Marone, F., 2019. Crystallographic orientations of magnesiochromite inclusions in diamonds: what do they tell us? Contrib. to Mineral. Petrol. 174, 29.
Nimis, P., Grütter, H., 2010. Internally consistent geothermometers for garnet peridotites and pyroxenites. Contrib. to Mineral. Petrol. 159, 411–427.
Nimis, P., Preston, R., Perritt, S.H., Chinn, I.L., 2020. Diamond's depth distribution systematics. Lithos 376–377, 105729.
O'Neill, C., Aulbach, S., 2022. Destabilization of deep oxidized mantle drove the Great Oxidation Event. Sci. Adv. 8, 1–6.
O'Neill, H.S.C., Wall, V.J., 1987. The Olivine--Orthopyroxene--Spinel Oxygen Geobarometer, the Nickel Precipitation Curve, and the Oxygen Fugacity of the Earth's Upper Mantle. J. Petrol. 28, 1169–1191.
Pearson, D.., Shirey, S.., Bulanova, G.., Carlson, R.., Milledge, H.., 1999. Re-Os isotope measurements of single sulfide inclusions in a Siberian diamond and its nitrogen aggregation systematics. Geochim. Cosmochim. Acta 63, 703–711.

Pearson, D.G., Canil, D., Shirey, S.B., 2003. Mantle Samples Included in Volcanic Rocks: Xenoliths and Diamonds, in: Treatise on Geochemistry. Elsevier, pp. 171–275.
Pearson, D.G., Shirey, S.B., Bulanova, G.P., Carlson, R.W., Milledge, H.J., 1999. Dating and paragenetic distinction of diamonds using the Re-Os isotope system; application to some Siberian diamonds, in: Proceedings of the 7th International Kimberlite Conference. pp. 637–643.
Pearson, D.G., Wittig, N., 2014. The Formation and Evolution of Cratonic Mantle Lithosphere – Evidence from Mantle Xenoliths, in: Treatise on Geochemistry. Elsevier, pp. 255–292.
Phillips, D., Harris, J.W., Viljoen, K.S., 2004. Mineral chemistry and thermobarometry of inclusions from De Beers Pool diamonds, Kimberley, South Africa. Lithos 77, 155–179.
Pokhilenko, N.P., Pearson, D.G., Boyd, F.R., Sobolev, N. V, 1991. Megacrystalline dunites and peridotites: hosts for Siberian diamonds. Carnegie Inst. Washingt. Yearb. 90, 11–18.
Pokhilenko, N.P., Sobolev, N. V, Boyd, F.R., Pearson, D.G., Shimizu, N., 1993. Megacrystalline pyrope peridotites in the lithosphere of the Siberian platform: mineralogy, geochemical peculiarities and the problem of their origin. Russ. Geol. Geophys. 34, 56–67.
Potapkin, V., Chumakov, A., Smirnov, G., Celse, J., Rüffer, R., McCammon, C.A., Dubrovinsky, L., 2012. The 57Fe Synchrotron Mössbauer Source at the ESRF. J. Synchrotron Radiat. 19, 559–569.
Prescher, C., McCammon, C.A., Dubrovinsky, L., 2012. MossA : a program for analyzing energy-domain Mössbauer spectra from conventional and synchrotron sources. J. Appl. Crystallogr. 45, 329–331.
Richardson, S.H., Harris, J.W., 1997. Antiquity of peridotitic diamonds from the Siberian craton. Earth Planet. Sci. Lett. 151, 271–277.
Rüffer, R., Chumakov, A.I., 1996. Nuclear-resonance beamline at ESRF. Hyperfine Interact. 97–98, 586–604.
Ryan, C.G., Griffin, W.L., Pearson, N.J., 1996. Garnet geotherms: Pressure-temperature data from Cr-pyrope garnet xenocrysts in volcanic rocks. J. Geophys. Res. Solid Earth 101, 5611–5625.
Schrauder, M., Navon, O., 1993. Solid carbon dioxide in a natural diamond. Nature 365, 42–44.
Sheldrick, G.M., 2015. Crystal structure refinement with SHELXL. Acta Crystallogr. Sect. C Struct. Chem. 71, 3–8.
Shirey, S.B., Cartigny, P., Frost, D.J., Keshav, S., Nestola, F., Nimis, P., Pearson, D.G., Sobolev, N., Walter, M.J., 2013. Diamonds and the Geology of Mantle Carbon, in: Reviews in Mineralogy and Geochemistry. pp. 355–421.
Smit, K. V, Shirey, S.B., Stern, R.A., Steele, A., Wang, W., 2016. Diamond growth from C–H–N–O recycled fluids in the lithosphere: Evidence from CH 4 micro-inclusions and δ 13 C– δ 15 N–N content in Marange mixed-habit diamonds. Lithos 265, 68–81.
Sobolev, N.V., 1977. Deep-seated inclusions in kimberlites and the problem of the composition of the upper mantle. American Geophysical Union.
Sobolev, N.V., Logvinova, A.M., Zedgenizov, D.A., Pokhilenko, N.P., Malygina, E.V., Kuzmin, D.V., Sobolev, A.V., 2009. Petrogenetic significance of minor elements in olivines from diamonds and peridotite xenoliths from kimberlites of Yakutia. Lithos 112, 701–713.
Sobolev, N.V., Logvinova, A.M., Zedgenizov, D.A., Seryotkin, Y.V., Yefimova, E.S., Floss, C., Taylor, L.A., 2004. Mineral inclusions in microdiamonds and macrodiamonds from kimberlites of Yakutia: a comparative study. Lithos 77, 225–242.
Sokol, A.G., Pal'yanov, Y.N., 2008. Diamond formation in the system MgO–SiO2–H2O–C at 7.5 GPa and 1,600°C. Contrib. to Mineral. Petrol. 155, 33–43.
Sokol, A.G., Palyanova, G.A., Palyanov, Y.N., Tomilenko, A.A., Melenevsky, V.N., 2009. Fluid regime and diamond formation in the reduced mantle: Experimental constraints. Geochim. Cosmochim. Acta 73, 5820–5834.

Stachel, T., Aulbach, S., Harris, J.W., 2022. Mineral Inclusions in Lithospheric Diamonds. Rev. Mineral. Geochemistry 88, 307–391.
Stachel, T., Chacko, T., Luth, R.W., 2017. Carbon isotope fractionation during diamond growth in depleted peridotite: Counterintuitive insights from modelling water-maximum CHO fluids as multi-component systems. Earth Planet. Sci. Lett. 473, 44–51.
Stachel, T., Harris, J.W., 2008. The origin of cratonic diamonds — Constraints from mineral inclusions. Ore Geol. Rev. 34, 5–32.
Stachel, T., Luth, R.W., 2015. Diamond formation - Where, when and how? Lithos 220–223, 200–220.
Stagno, V., Ojwang, D.O., McCammon, C.A., Frost, D.J., 2013. The oxidation state of the mantle and the extraction of carbon from Earth's interior. Nature 493, 84–88.
Taylor, W.R., 1998. An experimental test of some geothermometer and geobaro-meter formulations for upper mantle peridotites with application to the ther-mobarometry of fertile lherzolite and garnet websterite. Neues Jahrb. für Mineral. - Abhandlungen 172, 381–408.
Thomassot, E., Cartigny, P., Harris, J.W., Fanusviljoen, K., 2007. Methane-related diamond crystallization in the Earth's mantle: Stable isotope evidences from a single diamond-bearing xenolith. Earth Planet. Sci. Lett. 257, 362–371.
Viljoen, K.S., Perritt, S.H., Chinn, I.L., 2018. An unusual suite of eclogitic, websteritic and transitional websteritic-lherzolitic diamonds from the Voorspoed kimberlite in South Africa: Mineral inclusions and infrared characteristics. Lithos 320–321, 416–434.
Wang, A., Pasteris, J.D., Meyer, H.O.A., Dele-Duboi, M.L., 1996. Magnesite-bearing inclusion assemblage in natural diamond. Earth Planet. Sci. Lett. 141, 293–306.
Wiggers de Vries, D.F., Pearson, D.G., Bulanova, G.P., Smelov, A.P., Pavlushin, A.D., Davies, G.R., 2013. Re–Os dating of sulphide inclusions zonally distributed in single Yakutian diamonds: Evidence for multiple episodes of Proterozoic formation and protracted timescales of diamond growth. Geochim. Cosmochim. Acta 120, 363–394.
Wilson, A.J.C., 1995. International Tables for Crystallography, Vol. C, Mathematical, Physical and Chemical Tables, Kluwer Academic Publishers, Dordrecht.
Woodland, A.., Koch, M., 2003. Variation in oxygen fugacity with depth in the upper mantle beneath the Kaapvaal craton, Southern Africa. Earth Planet. Sci. Lett. 214, 295–310.
Yaxley, G.M., Berry, A.J., Kamenetsky, V.S., Woodland, A.B., Golovin, A. V, 2012. An oxygen fugacity profile through the Siberian Craton — Fe K-edge XANES determinations of Fe3+/∑Fe in garnets in peridotite xenoliths from the Udachnaya East kimberlite. Lithos 140–141, 142–151.
Yaxley, G.M., Berry, A.J., Rosenthal, A., Woodland, A.B., Paterson, D., 2017. Redox preconditioning deep cratonic lithosphere for kimberlite genesis – evidence from the central Slave Craton. Sci. Rep. 7, 30.
Zhang, C., Duan, Z., 2010. GFluid: An Excel spreadsheet for investigating C–O–H fluid composition under high temperatures and pressures. Comput. Geosci. 36, 569–572.
Ziberna, L., Klemme, S., Nimis, P., 2013. Garnet and spinel in fertile and depleted mantle: insights from thermodynamic modelling. Contrib. to Mineral. Petrol. 166, 411–421.

# 4. EoS of mantle minerals coupled with composition and thermal state of the lithosphere: Inferring the density structure of peridotitic systems

Luca FACCINCANI [1,✉], Barbara FACCINI [1], Federico CASETTA [1,2], Maurizio MAZZUCCHELLI [3], Fabrizio NESTOLA [4], Massimo COLTORTI [1,5]

[1] Department of Physics and Earth Sciences, University of Ferrara, Via Saragat 1, 44121 Ferrara, Italy
[2] Department of Lithospheric Research, University of Vienna, Althanstraße 14, 1090 Vienna, Austria
[3] Department of Chemical and Geological Sciences, University of Modena and Reggio Emilia, Via Campi 103, 41125 Modena, Italy
[4] Department of Geosciences, University of Padua, Via Gradenigo 6, 35131 Padua, Italy
[5] Istituto Nazionale di Geofisica e Vulcanologia (INGV) Sezione di Palermo, Via Ugo la Malfa 153, 90146 Palermo, Italy
✉ luca.faccincani@unife.it

This chapter has been published as:
Faccincani et al. (2021) *Lithos*, **404–405**, 106483.

## Abstract

Unravelling the physical state and properties of mantle rocks is crucial for understanding both plate tectonics, seismic activity, and volcanism. In this context, the knowledge of accurate elastic parameters of constituent mineral phases, and their variations with pressure (*P*) and temperature (*T*), is an essential requirement, that coupled with the thermal state of the lithosphere can provide a better understanding of its petrophysics and thermochemical structure.

In this paper, we present an assessment of the thermoelastic parameters [in the form of *P–V–T–K* Equations of State (EoS)] of orthopyroxene, clinopyroxene, spinel and garnet based on X-Ray diffraction data and direct elastic measurements available in literature. The newly developed EoS are appropriate to describe the elastic behaviour of these phases under the most relevant *P–T* conditions and bulk compositions of the Earth's mantle. In combination with the published EoS for mantle olivine and magnesiochromite, these EoS are suitable to calculate the physical properties of mantle peridotites and their variation with *P* and *T*.

Thanks to these EoS, we can evaluate how the variations in bulk composition and thermal regimes affect the density structure of the lithospheric mantle. Accordingly, the density structure of fertile and depleted peridotitic systems was calculated along the 35, 45 and 60 mW $m^{-2}$ geothermal gradients at *P* comprised between 1 and 8 GPa. Under very cold

geothermal gradients, the density of both fertile and depleted peridotitic systems progressively increases with depth, whereas under relatively hot conditions a first downwards decrease from 1 to ca 3 GPa is observed, followed by an increase downward. In mantle sections characterized by intermediate geotherms (45 mW $m^{-2}$), the behaviour of the two systems differs up to ca 4 GPa, as the density of the depleted system remains nearly constant down to this depth whereas it moderately increases in the fertile system.

The results of our simplified parameterisation, in agreement with classical thermodynamic modelling, indicate that the density structure of the lithospheric mantle is predominantly controlled by the *P–T* gradient variations, with some compositional control mostly arising at cold-intermediate thermal conditions. Integrated by geophysical and thermodynamic modelling, the newly developed and selected EoS could provide an alternative strategy to infer the elastic properties of mineral phases and peridotite rocks, under the most relevant *P–T* conditions and compositions of the Earth's mantle, without requiring sets of end-member properties and solution models.

**Keywords**: Equations of State, Mantle minerals, Upper mantle density structure, Fertile and depleted peridotites, Cold-hot geotherms

## 4.1 Introduction

Understanding the density structure of the upper mantle is critical to our comprehension of the tectonic and magmatic evolution of the lithosphere (e.g., Braun, 2010; Capitanio et al., 2007; Simon and Podladchikov, 2008; Thybo and Artemieva, 2013) and crucial to address complex geodynamic phaenomena (e.g., mantle convection, plume upwelling, slab subduction, crustal movements). The density of the upper mantle ultimately depends on both its thermal and compositional structure, which can be derived from petrological-geochemical studies on exhumed mantle samples, i.e., xenoliths and tectonically exposed mantle sections, and from the interpretation of seismic data (and in general of geophysical observables, e.g., gravity anomalies, surface heat flow, etc.).

Thermobarometric, petrochemical and isotopic studies of xenoliths and exposed mantle sections can help in unveiling the compositional and thermal structure of their source mantle at the time of the eruption or emplacement (e.g., Coltorti et al., 2021; Mazzucchelli et al., 2009; Melchiorre et al., 2020; Pearson et al., 2003) but the structure of the lithosphere may only be defined at a local scale, as large portions remain inaccessible. Differently, seismic data are endowed with a more continuous spatial coverage, to such an extent that the mantle

may be imaged at a lithospheric scale; however, their conversion into models of the upper mantle is not straightforward (Afonso et al., 2013, and references therein). The interpretation of seismic data relies on appropriate combinations of the observed seismic wave velocities with either thermodynamic concepts and/or experimental data from mineral physics (e.g., Bass and Anderson, 1984) and needs to account for both compositional and thermal signatures in wave velocities. Uncertainties in data interpretation are further exacerbated since ultramafic rocks with different compositions can fit equally well wave velocities (e.g., Afonso et al., 2013).

In general, addressing the thermochemical structure of the mantle requires the calculation of mineral and rock physical properties (elastic moduli, thermal expansions, densities, etc.) at elevated pressure and temperature. Unequivocally, the knowledge of accurate elastic parameters of candidate mantle phases, and their variations with pressure and temperature, is required. In this context, the Equations of State (EoS) of mantle phases are undoubtedly the best proxy for unravelling the structure and dynamics of the Earth's mantle (e.g., Afonso et al., 2007; Stixrude and Lithgow-Bertelloni, 2005a) and its evolution through time, as they can define how volume, density or the elastic properties of minerals vary with pressure and/or temperature (e.g., Angel, 2000). For rocks, the elastic properties have to be inferred from those of their constituent minerals, at appropriate conditions (Connolly, 2009). This is commonly done by phase equilibria calculations based on thermodynamic data (Afonso et al., 2008; Connolly and Petrini, 2002; Stixrude and Lithgow-Bertelloni, 2011, 2005a) (see Connolly, 2009 for extensive considerations of phase equilibria calculations to geodynamic modelling), with aggregate properties calculated by any standard solid mixing theory (e.g., Abers and Hacker, 2016; Hacker and Abers, 2004, and references therein). As mass in aggregates is a simple sum of chemical component masses, the density of rocks can be then calculated from the density of constituent minerals according to their volume proportion.

Several studies attempted to evaluate the density distribution of the lithosphere, known to be vertically and laterally heterogeneous due to variable mineralogy (in terms of mineral and modal compositions), complex phase transitions and differing thermal regimes. It was showed that the increase of Mg/(Mg+Fe) during partial melting lowers the bulk density of the mantle (Schutt and Lesher 2006), but is not affecting phase transitions unlike Na content, which controls the spinel-plagioclase transition and may play an important role in areas of high heat flows and thin crust (Simon and Podladchikov, 2008). Further studies investigated the density structure of mantle sections either by combining data from petrology, mineral physics and geophysics (e.g., Fullea et al., 2014) or by classic thermodynamic calculations complemented for the most relevant Cr-bearing phases in the upper mantle (Ziberna and

Klemme, 2016). These studies showed some contrasting results as to whether the predominant control on the density variations of the lithosphere is due to the thermal state, bulk composition, or their interplay.

In this work, we set out to explore the density structure of the lithospheric mantle, and its variation with changes in bulk composition and thermal gradient, from the perspective of the EoS of its constituent minerals, following a simplified parameterisation. The first part presents an assessment of the thermoelastic parameters of orthopyroxene, clinopyroxene, spinel and garnet. To this aim, pre-existing literature data on compressibility, thermal expansion and elasticity of these phases were used to constrain their *P–V–T–K* (*P* = pressure, *V* = volume, *T* = temperature, *K* = bulk modulus) EoS in peridotitic systems (i.e., preferentially selecting data measured on crystals with chemical compositions comparable to those expected in the upper mantle). As already computed in recent detailed studies, *P–V–T–K* and *P–V–T* EoS for mantle olivine and magnesiochromite were selected from literature (Angel et al., 2018; Nestola et al., 2019b); two distinct EoS were used for mantle spinels to account for the variation of their elastic properties in response to varying Cr and Al contents (cf. Subsection 4.2.3). The second part of this work aims at investigating how the density structure of fertile and depleted lithospheric mantle sections is affected by different thermal regimes (35, 45 and 60 mW $m^{-2}$ geothermal gradients), following a simplified parameterisation that does not incorporate phase relations. Beyond exploring the density variations with this approach, we also provide a comparison with classic thermodynamic modelling (Perple_X; Ziberna and Klemme, 2016). This comparison allowed to assess that (i) the density profiles can be readily computed following our simplified parameterisation, (ii) the thermal gradient is the controlling variable when it comes to the density structure of the lithosphere and (iii) the newly developed and selected EoS consistently describe the elastic behaviour of the related phases under the most relevant *P–T* conditions and compositions of the Earth's mantle, without requiring sets of end-member properties and solution models.

## 4.2 Data selection and EoS fitting

There are two possible approaches to describe the *P–V–T* or *P–V–T–K* behaviour of solids: thermal-pressure models (Holland-Powell and Mie-Grüneisen-Debye thermal-pressure EoS) and isothermal-type models at high temperature (cf. Angel et al., 2018). For extensive considerations to these issues the reader is referred to Anderson (1995), Angel (2000) and Angel et al. (2018).

The thermoelastic properties for mantle olivine ($Fo_{90-92}$) have been extensively reviewed and the *P–V–T–K* EoS was recently published (Angel et al., 2018). Considering the *P–T* ranges of our investigation, we selected the third-order Birch-Murnaghan compressional EoS in combination with the isothermal-type model for all the computations.

The *P–V–T* EoS for mantle magnesiochromite was also recently published (Nestola et al., 2019b), parametrised as second-order Birch-Murnaghan compressional EoS in combination with the Holland-Powell thermal-pressure EoS; this formulation was used for the computations of magnesiochromite for the depleted peridotitic system. The selected thermoelastic parameters for mantle olivine and mantle magnesiochromite are reported in Table 4.1.

The thermoelastic behaviour of pyroxenes, spinel and garnet was here constrained based on X-Ray diffraction data (compressibility and thermal expansion) and elasticity measurements available in literature. The full EoS for these phases were solved with the EosFit7c program (Angel et al., 2014a) following the approach of Milani et al. (2017) to perform simultaneous fits of elastic moduli and cell parameters. For every phase, each individual data set of volumes was scaled to its own volume at room conditions prior to fitting the data together. Additionally, in order to compare X-Ray diffraction and elasticity measurements, $K_{SR}$ (adiabatic Reuss bulk moduli, from elasticity data) were converted into $K_{TR}$ (isothermal Reuss bulk moduli, from X-Ray diffraction data) according to the relationship $K_{SR} = (1 + \alpha_V \gamma T) K_{TR}$ where $\alpha_V$ is the volume thermal expansion (taken from the EoS itself, at the *P–T* of interest) and $\gamma$ is the Grüneisen parameter (taken from literature).

## 4.2.1 Orthopyroxene

Mantle orthopyroxenes (space group *Pbca*) are solid solutions between enstatite ($Mg_2Si_2O_6$) and ferrosilite ($Fe_2Si_2O_6$) end-members and typically contain few wt% of $Al_2O_3$ and some CaO as well (e.g., McDonough and Rudnick, 1998). A reanalysis of $K_{TR}$ and its pressure derivative $K'_{TR}$ of $Mg_2Si_2O_6$ based on different experiments (two compression, one Brillouin measurement and one ultrasonic measurement) (Angel and Jackson, 2002) yielded the best estimates of $K_{TR,0}$ and $K'_{TR,0}$, being respectively 105.8(5) GPa and 8.5(3). By comparison, measurements on aluminium-bearing natural orthopyroxenes showed higher bulk moduli and lower pressure derivatives (Chai et al., 1997; Hugh-Jones et al., 1997; Zhang and Bass, 2016, refit of their data) than that of $Mg_2Si_2O_6$. For these reasons, $Mg_2Si_2O_6$ enstatite cannot be considered a good representation of the elastic behaviour of the orthopyroxene component in the lithospheric upper mantle.

We selected data from five different experiments on mantle orthopyroxenes: two compressions (Hugh-Jones and Angel, 1997) [samples *N1* and *N2*]), two expansions (Yang and Ghose, 1994 [sample *Fs20*]; Scandolo et al., 2015 [sample *B22 N.60*]) and one high-pressure Brillouin measurement (Zhang and Bass, 2016a). We are not aware of any volume measurements on either mantle-composition orthopyroxene or enstatite made at low temperature; consequently, the Einstein temperature ($\theta_E$) could not be refined and was fixed at 510 K (Holland and Powell, 2011, corresponding to Fs20). The Grüneisen parameter (0.85, for Fs20) was taken from Yang and Ghose (1994) and assumed that it does not vary with temperature. With these constraints, we fitted simultaneously each individual data set with a third-order Birch-Murnaghan compressional EoS in combination with the isothermal-type model (parameterisation from Angel et al., 2018); the final refined EoS parameters (Table 4.1) fit all the data within the experimental uncertainties (Supplementary Material File 1, Figure S1). The final EoS for mantle orthopyroxene is provided in Supplementary Material File 2.

### 4.2.2 Clinopyroxene

Mantle clinopyroxenes (space group *C2/c*) are solid solutions between diopside ($CaMgSi_2O_6$) and hedenbergite ($CaFeSi_2O_6$) end-members and typically contain few wt% of $Al_2O_3$, some $Cr_2O_3$ as well as $Na_2O$ (e.g., McDonough and Rudnick, 1998).

A survey of the literature showed that $K_{TR,0}$ and $K'_{TR,0}$ values for $CaMgSi_2O_6$ diopside and near end-member compositions exhibit large variations; the same is for $K_{S,0}$ and $K'_{S,0}$ (see Xu et al., 2019 for a recent compilation of literature data).

We selected data from six different experiments on diopside and near end-member compositions: one compression (Li and Neuville, 2010 [room temperature data]), three expansions (Cameron et al., 1973 [sample *Diopside*]; Pandolfo et al., 2015 [sample *Di*]; Prencipe et al., 2000), one high-pressure Brillouin measurement (Sang and Bass, 2014) and one high-temperature RUS measurement (Isaak et al., 2006). The Grüneisen parameter (0.867) is taken from Isaak et al. (2006) and assumed that it does not vary with temperature. $K_{SR,0}$ for near end-member diopsides recalculated from $c_{ij}$ data of Sang and Bass (2014) and Isaak et al. (2006) are significantly different between each other (respectively, 111.2(7) GPa vs 113.4(9) GPa). To make the fit consistent between these two data sets, we excluded $K_{SR,0}$ of Sang and Bass (2014). We also excluded from the fit the data point of Sang and Bass (2014) at 14 GPa, which lies completely outside the trend (Supplementary Material File 1, Figure S2). With these constraints, we fitted simultaneously each individual data set with a third-order Birch-Murnaghan compressional EoS in combination with the isothermal-type

model (parameterisation from Angel et al., 2018); the final refined EoS parameters (Table 4.1) fit almost all the data within the experimental uncertainties (Supplementary Material File 1, Figure S2). The final EoS for mantle clinopyroxene is provided in Supplementary Material File 3.

Bearing in mind that the selected data sets correspond to near end-member and $CaMgSi_2O_6$ diopside, it must be considered carefully whether the final refined thermoelastic parameters are a good representation of the elastic behaviour of the clinopyroxene component in the lithospheric upper mantle. Indeed, clinopyroxenes with augitic compositions are a common species occurring in a wide variety of igneous rocks and can be occasionally found in ultrabasic rocks. Xu et al. (2017) and (2019) recently studied the thermoelastic behaviour of augite by synchrotron-based X-Ray diffraction combined with an externally heated diamond anvil cell. Their experiments yielded respectively $K_{TR,0}$ = 111(1) GPa, $K'_{TR,0}$ = 4.1(1) and $K_{TR,0}$ = 112(3) GPa, $K'_{TR,0}$ = 5.0(7). These results prove that clinopyroxenes with augitic compositions behave similarly to near end-member diopsides. Therefore, we are confident that our *P–V–T–K* EoS parameters can be applied to a wide range of mantle clinopyroxene compositions.

### 4.2.3 Spinel

Mantle spinels (space group *Fd-3m*) show extensive solid solution between end-members as they typically vary in composition between four components: spinel s.s. ($MgAl_2O_4$), hercynite ($FeAl_2O_4$), magnesiochromite ($MgCr_2O_4$) and chromite ($FeCr_2O_4$). The compositional variations in mantle spinels are mainly displayed in their Cr/(Cr + Al) and Mg/(Mg + Fe) molar ratios, which reflect the degree of melt depletion experienced by a peridotite. Indeed, spinels with high Al and low Cr contents characterize lherzolites, whereas low Al and high Cr contents distinguish harzburgitic spinels (e.g., McDonough and Rudnick, 1998).

The bulk modulus systematics for Mg-Fe-Cr-Al spinels have been recently analysed by Nestola et al. (2015, and references therein), who showed that: (i) the Cr-Al substitution considerably changes the $K_{TR,0}$ [192(1) vs 182.5(1.4) GPa for $MgAl_2O_4$ and $MgCr_2O_4$, respectively]; (ii) the Fe-Mg substitution does not substantially affect the bulk modulus for either Cr or Al spinels [193.9(1.7) vs 184.8(1.7) GPa for $FeAl_2O_4$ and $FeCr_2O_4$, respectively], with the $K'_{TR,0}$ similar for all four end-members. Thus, the $K_{TR,0}$ of Mg-Fe-Cr-Al spinels is roughly controlled by the Cr/Al ratio. Hence, two EoS are needed to properly describe the elastic behaviour of mantle spinels: one EoS for lherzolitic spinels and another

EoS (selected from Nestola et al., 2019, see above) for harzburgitic spinels (magnesiochromites).

To constrain the elastic behaviour of Al-rich lherzolitic spinels, we selected data from six different experiments: one compression (Nestola et al., 2007 [sample *disordered*]), three expansions (Carbonin et al., 2002 [sample *NAT*]; Grimes and Al-Ajaj, 1992; Martignago et al., 2003 [sample *H-Cr*]), one high-pressure Brillouin measurement (Speziale et al., 2016) and one high-temperature RPR measurement (Suzuki et al., 2000). The Grüneisen parameter (1.17) was taken from Suzuki et al. (2000) and assumed that it does not vary with temperature. Because the quoted uncertainties of $K_{SR}$ from Suzuki et al. (2000) are substantially smaller than those expected from elasticity measurements (e.g. 1 to 3 GPa), we under-weighted the experimental data (1% esd was assumed for all data). With these constraints, we fitted simultaneously each individual data set with a third-order Birch-Murnaghan compressional EoS in combination with the Holland-Powell thermal-pressure EoS; the final refined EoS parameters (Table 4.1) fit almost all the data within the experimental uncertainties (Supplementary Material File 1, Figure S3). The final EoS for mantle spinel is provided in Supplementary Material File 4. Considering the bulk modulus systematics for Mg-Fe-Cr-Al spinels, we are confident that our *P–V–T–K* EoS parameters can be applied to a wide range of Al-rich spinel compositions.

### 4.2.4 Garnet

Mantle garnets (space group *Ia-3d*, general formula $X_3Y_2Si_3O_{12}$) are multicomponent substitutional solid solutions since different cations can be mutually exchanged at the X (Mg, Fe, Ca, Mn divalent cations) and Y (Al, Fe, Cr trivalent cations) sites. Compositionally, the most significant components of peridotitic garnets are $Mg_3Al_2Si_3O_{12}$ pyrope (ca 75%), $Ca_3Al_2Si_3O_{12}$ grossular (ca 10%) and $Fe_3Al_2Si_3O_{12}$ almandine (ca 15%) (e.g., Wood et al., 2013).

The effect of Mg-Fe substitution for the pyrope-almandine solid solution was recently analysed by Lu et al. (2013) and Milani et al. (2015). Milani et al. (2015) determined $K_{TR,0}$ = 163.7(1.7) GPa for pyrope, $K_{TR,0}$ = 167.2(1.7) GPa for an intermediate $Py_{60}Alm_{40}$ and $K_{TR,0}$ = 172.6(1.5) GPa for almandine, with similar $K'_{TR,0}$ for all three garnets, claiming that Fe substituting for Mg linearly increases $K_{TR,0}$ but does not affect $K'_{TR,0}$. However, compared to the sources reviewed by Milani et al. (2015), the determined $K_{TR,0}$ values are notably lower than expected whereas $K'_{TR,0}$ are slightly higher and this can be ascribed to the well-known trade-off between fit values for $K_{TR,0}$ and $K'_{TR,0}$. Lu et al. (2013) measured the elasticity of a Fe-bearing pyrope by high *P–T* Brillouin spectroscopy, determining $K_{SR,0}$ = 168.2(1.8) and

**Table 4.1.** Thermoelastic parameters selected from literature ([1] Angel et al., 2018; [2] Nestola et al., 2019) and derived from the fitting of *P–V–T–K* data for mantle phases. BM3-Isothermal = Third-order Birch-Murnaghan compressional EoS in combination with the isothermal-type model (parameterisation from Angel et al., 2018); BM3-HP = Third-order Birch-Murnaghan compressional EoS in combination with the Holland-Powell thermal-pressure EoS; BM2-HP = Second-order Birch Murnaghan compressional EoS in combination with the Holland-Powell thermal-pressure EoS.

| | **Olivine [1]** | **Orthopyroxene** | **Clinopyroxene** | **Spinel** | **Magnesiochromite [2]** | **Garnet** |
|---|---|---|---|---|---|---|
| | ***BM3 - Isothermal*** | ***BM3 - Isothermal*** | ***BM3 - Isothermal*** | ***BM3 - HP*** | ***BM2 - HP*** | ***BM3 - HP*** |
| $K_{TR,0}$ **(GPa)** | 126.4(2) | 111.8(7) | 112.8(3) | 194.8(2) | 183.3(5) | 168.63(20) |
| $K'_{TR,0}$ | 4.51(5) | 7.39(19) | 4.95(9) | 4.64(7) | 4 *fixed* | 5.11(9) |
| $K''_{TR,0}$ | –0.0368 *implied* | –0.1681 *implied* | –0.0509 *implied* | –0.0254 *implied* | –0.0212 *implied* | –0.0369 *implied* |
| $\alpha_{V0}$ **(K$^{-1}$)** | 2.666(9) x $10^{-5}$ | 2.591(18) x $10^{-5}$ | 2.67(7) x $10^{-5}$ | 1.86(2) x $10^{-5}$ | 1.66(2) x $10^{-5}$ | 2.392(9) x $10^{-5}$ |
| $\theta_E$ **(K)** | 484(6) | 510 *fixed* | 343(58) | 714(15) | 683(16) | 450(6) |
| $\delta_T$ | 5.77(7) | 9.0(6) | 4.84(17) | - | - | - |
| $\delta'$ | –3.5(1.1) | 0 *fixed* | 0 *fixed* | - | - | - |
| $\gamma_0$ | 1.044 *fixed* | 0.85 *fixed* | 0.867 *fixed* | 1.17 *fixed* | - | 1.19 *fixed* |
| $q$ | 1.88 *fixed* | 0 *fixed* | 0 *fixed* | 0 *fixed* | - | 0 *fixed* |
| $\chi^2$ | *not reported* | 0.94 | 0.44 | 0.93 | 1.1 | 1.51 |
| ***N data*** | 121 | 73 | 74 | 93 | 53 | 85 |

$K'_{SR,0}$ = 4.4(1). Comparative analysis of these results led the authors to conclude that addition of Fe does significantly affect $K_{SR,0}$ but rather has a weak positive effect on $K'_{SR,0}$. A similar conclusion was reached by Jiang et al. (2004), who showed that Fe substituting for Mg in the pyrope-almandine series has a little effect on the bulk modulus (almandine $K_{SR,0}$ being 2% higher than that of pyrope) while it increases its pressure derivative. The effect of Ca-Mg substitution for the pyrope-grossular solid solution has been analysed again by Jiang et al. (2004), who showed that the $K_{SR,0}$ varies by ca 2% across the pyrope-grossular system and that there are no evident trends in the $K'_{SR,0}$. In view of these considerations, we selected data from four different experiments: one compression (Milani et al., 2015 [sample $Py_{60}Alm_{40}$]), two expansions (Bosenick and Geiger, 1997 [excluding the scattered data at 220 K], Milani et al., 2015 [sample $Py_{100}$]) and one high-temperature RUS measurement (Suzuki and Anderson, 1983). The Grüneisen parameter (1.19) was taken from Gillet et al. (1992) and assumed that it does not vary with temperature. With these constraints, we fitted simultaneously each individual data set with a third-order Birch-Murnaghan compressional EoS in combination with the Holland-Powell thermal-pressure EoS; the final refined EoS parameters (Table 4.1) fit all the data within the experimental uncertainties (Supplementary Material File 1, Figure S4). The final EoS for mantle garnet is provided in Supplementary Material File 5. Considering the bulk modulus systematics for Mg-Fe-Ca aluminous garnets, we are confident that our *P–V–T–K* EoS parameters can be applied to a wide range of mantle garnet compositions.

# 4.3 Density variations in the lithospheric mantle

## 4.3.1 Density calculations

The density of mantle peridotites is function of the chemical composition, modal abundance and elastic properties of their constituent minerals, which in turn are controlled by pressure, temperature and bulk composition of the system. Here, the density structure of the lithospheric mantle was calculated following a two-step approach.

The first step involved the calculation of density profiles for each phase along the geothermal gradients of interest. To our purposes, three geothermal gradients of 35, 45 and 60 mW $m^{-2}$ were chosen as considered representative of extremely cold, intermediate, and relatively hot lithospheric sections. The density of each phase was calculated in the form of 'crystallographic density' according to the relation:

$$\rho_{(phase\ at\ PT)} = \frac{Z_{(phase)} \times Mw_{(phase)}}{\left(\frac{V}{V_0}\right)_{(EoS\ at\ PT)} \times V_{0(phase)} \times Na} \quad (4.1)$$

where $\left(\frac{V}{V_0}\right)_{(EoS\ at\ PT)}$ represents the volume [here the normalized volume $\left(\frac{V}{V_0}\right)$] calculated from the EoS at specific *P–T* conditions (e.g., for a characteristic geotherm or at any *P–T*), $V_{0(phase)}$ is the reference unit-cell volume of the phase measured at ambient conditions, $Mw_{(phase)}$ its molecular weight, $Z_{(phase)}$ is the number of formula units in the unit cell and $Na$ the Avogadro number.

The second step involved the calculation of density profiles for bulk rocks, which were here calculated from the densities $\rho_i$ of n constituent minerals as:

$$\rho_{(bulk\ rock)} = \left(\sum_{i=1}^{n} \rho_i \times \mathrm{v}_i\right)/n \quad (4.2)$$

where $v_i$ is the volume proportion of each mineral.

We computed density profiles for all constituent mineral phases and for two potential lithospheric mantle sections, a fertile and a depleted peridotitic systems, along the 35, 45 and 60 mW $m^{-2}$ geothermal gradients. Calculations for the two lithospheric sections were restricted to a *P–T* range of 1–8 GPa and 350–1375 °C. These gradients were selected from the preferred geotherm family of Hasterok and Chapman (2011), which are based on radiogenic heat production measurements together with xenolith thermobarometry and tectonothermal constraints. Following Hasterok and Chapman (2011), we assumed that the transition from a conductive to an adiabatic geotherm corresponds to the lithosphere-asthenosphere boundary (LAB), which is here used only to discuss the effect of temperature on density profiles.

Our calculations at subsolidus conditions do not include the effects of porosity, mineral texture and rock microstructure as well as no volatile-bearing phases, thus excluding OH groups in NAMs and/or intergranular fluids and/or melts.

Calculations were based on previously studied natural peridotite xenoliths: a spinel lherzolite from the Veneto Volcanic Province (sample SG34 from Beccaluva et al., 2001) was adopted as representative of a fertile mantle, while a spinel harzburgite from Grande Comore island (sample NDR13, unpublished data from Coltorti et al., 1999), now under investigation for other petrological studies, was chosen to represent a depleted mantle. Modal compositions

**Table 4.2.** Mineral phases compositions (a.p.f.u.) and modes (SG34 spinel lherzolite) and selected reference phases for the computation of density profiles for the fertile lithospheric mantle section. References: [1] Zha et al., 1998; [2] Chai et al., 1997, [3] Brown and Collins, 1998; [4] Ono et al., 2018; [5] Sumino and Nishizawa, 1978 (PY-1 sample); # = esd assumed, Fe* = total iron, n.d. = not detected, n.a. = not available.

| | **Olivine** | | **Orthopyroxene** | | **Clinopyroxene** | | **Spinel** | | **Garnet** | |
|---|---|---|---|---|---|---|---|---|---|---|
| | **Selected [1]** | **Model** | **Selected [2]** | **Model** | **Selected [3]** | **Model** | **Selected [4]** | **Model** | **Selected [5]** | **Model** |
| **Si** | 1 | 0.9955 | 1.89 | 1.869 | 1.8756 | 1.857 | n.d. | n.d. | 3.0005 | n.a. |
| **Ti** | n.d. | n.d. | n.d. | 0.0029 | 0.0129 | 0.0136 | 0.0031 | 0.0016 | 0.0272 | n.a. |
| **Al** | n.d. | n.d. | 0.23 | 0.2225 | 0.2833 | 0.3437 | 1.7673 | 1.7484 | 1.7749 | n.a. |
| **Cr** | n.d. | n.d. | 0.01 | 0.0115 | 0.0275 | 0.0256 | 0.1871 | 0.1734 | 0.1202 | n.a. |
| **Fe*** | 0.2 | 0.2106 | 0.17 | 0.2046 | 0.0907 | 0.0983 | 0.2237 | 0.2761 | 0.5317 | n.a. |
| **Mn** | n.d. | 0.0017 | 0.01 | 0.0035 | 0.0026 | 0.0031 | 0.002 | 0.002 | 0.0217 | n.a. |
| **Mg** | 1.8 | 1.7882 | 1.63 | 1.6745 | 0.8513 | 0.7705 | 0.809 | 0.7915 | 2.1868 | n.a. |
| **Ca** | n.d. | 0.0005 | 0.04 | 0.0201 | 0.7596 | 0.7782 | n.d. | n.d. | 0.3326 | n.a. |
| **Na** | n.d. | n.d. | n.d. | n.d. | 0.105 | 0.1097 | n.d. | n.d. | n.d. | n.a. |
| **K** | n.d. | n.d. | n.d. | n.d. | n.d. | n.d. | n.d. | n.d. | n.d. | n.a. |
| **Ni** | n.d. | 0.0079 | n.d. | 0.0025 | 0.0001 | n.d. | 0.0079 | 0.007 | n.d. | n.a. |
| **Zn** | n.d. | n.d. | n.d. | n.d. | n.d. | n.d. | n.d. | 0.0035 | n.d. | n.a. |
| **Unit-cell volume [Å$^3$]** | 292.01(10) | n.a. | 834.1(5)# | n.a. | 432.96(4) | n.a. | 538.78(6) | n.a. | 1535.2(5)# | - |
| **Mode [spl stability field]** | 61.8 | | 20.0 | | 16.6 | | 1.6 | | 0.0 | |
| **Mode [grt stability field]** | 64.4 | | 15.1 | | 14.8 | | 0.0 | | 5.7 | |

**Table 4.3.** Mineral phases compositions (a.p.f.u.) and modes (NDR13 spinel harzburgite) and selected reference phases for the computation of density profiles for the depleted lithospheric mantle section. References: [1] Zha et al., 1998; [2] Gatta et al., 2007; [3] Comodi et al., 1995 (sample 3211); [4] Matsukage et al., 2010; [5] Babuška et al., 1978 (PY-2 sample); Fe* = total iron, n.d. = not detected, n.a. = not available.

| | Olivine | | Orthopyroxene | | Clinopyroxene | | Spinel | | Garnet | |
|---|---|---|---|---|---|---|---|---|---|---|
| | **Selected [1]** | **Model** | **Selected [2]** | **Model** | **Selected [3]** | **Model** | **Selected [4]** | **Model** | **Selected [5]** | **Model** |
| **Si** | 1 | 1.0031 | 1.968 | 1.9687 | 1.962 | 1.9568 | 3.0105 | n.a. | n.d. | 0.0004 |
| **Ti** | n.d. | n.d. | n.d. | 0.0005 | 0.002 | 0.0021 | 0.016 | n.a. | n.d. | 0.0017 |
| **Al** | n.d. | 0.0004 | 0.037 | 0.0545 | 0.121 | 0.0753 | 1.7297 | n.a. | 1 | 0.7961 |
| **Cr** | n.d. | 0.0005 | 0.011 | 0.0142 | 0.023 | 0.0494 | 0.178 | n.a. | 0.92 | 1.124 |
| **Fe*** | 0.2 | 0.1851 | 0.146 | 0.1682 | 0.072 | 0.0816 | 0.4874 | n.a. | 0.31 | 0.3618 |
| **Mn** | n.d. | 0.0028 | n.d. | 0.0044 | 0.001 | 0.0029 | 0.0198 | n.a. | n.d. | 0.0019 |
| **Mg** | 1.8 | 1.7965 | 1.813 | 1.7454 | 0.89 | 0.9779 | 2.191 | n.a. | 0.77 | 0.7057 |
| **Ca** | n.d. | 0.0012 | 0.025 | 0.0344 | 0.828 | 0.7985 | 0.3575 | n.a. | n.d. | 0.0003 |
| **Na** | n.d. | n.d. | n.d. | 0.0071 | 0.102 | 0.0642 | n.d. | n.a. | n.d. | n.d. |
| **K** | n.d. | n.d. | n.d. | n.d. | n.d | 0.0004 | n.d. | n.a. | n.d. | n.d. |
| **Ni** | n.d. | 0.007 | n.d. | 0.0025 | n.d | 0.0019 | n.d. | n.a. | n.d. | 0.0045 |
| **Zn** | n.d. | n.d. | n.d. | n.d. | n.d | n.d. | n.d. | n.a. | n.d. | 0.0035 |
| **Unit-cell volume [Å$^3$]** | 292.01(10) | n.a. | 834.71(3) | n.a. | 434.42(48) | n.a. | 560.68(16) | - | 1537.20(46) | - |
| **Mode [spl stability field]** | 85.4 | | 12 | | 1.6 | | 1.0 | | 0 | |
| **Mode [grt stability field]** | 86.7 | | 9.3 | | 0.9 | | 0.0 | | 3.1 | |

of the selected samples were calculated by least-squares mass balance using bulk-rock and mineral major element analyses (Tables 4.2, 4.3).

Bearing in mind that calculating the density of each phase requires a reference unit-cell volume measured at ambient conditions ($V_{0_{(phase)}}$, Equation 4.1), olivine, pyroxenes, spinel and garnet unit-cell parameters (and related crystal chemical compositions, which slightly differ compared to those expected from our models of fertile and depleted mantle) were selected from literature (Tables 4.2, 4.3). Modal compositions were kept from the two selected mantle xenoliths (SG34 spinel lherzolite and NDR13 spinel harzburgite), however density calculations were carried out by using the mineral compositions and unit-cell volumes of the reference minerals from the literature. All selected mineral compositions were kept fixed for all density calculations.

The spinel-garnet transition was modelled according to the approximate reaction spinel + pyroxenes = garnet + olivine (e.g., Klemme and O'Neill, 2000); mineral modes in the garnet stability field were calculated from stoichiometric balance upon completion of the reaction (Tables 4.2, 4.3). Recent thermodynamic modelling in natural peridotitic systems (Ziberna et al., 2013) indicates that garnet and spinel always coexist and the width and depth of the coexistence interval strongly, but not only, depends on the thermal state of the lithosphere (restricted depth interval – about 15 km – in regions with hot geotherms, and much broader interval – over 100 km – for cold geotherms). We simplified this model by assuming garnet + spinel coexistence intervals of 1.5–4 GPa, 1.5–3 GPa and 1.8–2.4 GPa along the 35, 45 and 60 mW $m^{-2}$ geothermal gradients, respectively, for both fertile and depleted mantle sections. For density calculations, mineral modes were kept fixed in spinel and garnet stability fields, and were imposed to vary linearly in the spinel-garnet stability field.

## 4.3.2 Results

Density profiles for both mineral phases and the fertile and depleted peridotitic systems were calculated along three different geothermal gradients: 35 mW $m^{-2}$, representative of the coldest cratonic mantle sections, 45 mW $m^{-2}$, typical of average cratonic sections, and 60 mW $m^{-2}$, for relatively hot, off-craton, lithospheric sections (Hasterok and Chapman, 2011) (Figures 4.1, 4.2, 4.3).

Figure 4.1 shows that, despite mineral phases having different elastic parameters (Table 4.1), their density variation with depth is largely controlled by the geothermal gradients. Under cold conditions (35 mW $m^{-2}$), density curves for all phases shows a subtle but significant decrease down to ca 1 GPa, which is followed by a marked increase for olivine and pyroxenes and a moderate increase for spinel, magnesiochromite and garnet. Under

relatively hot conditions (60 mW $m^{-2}$), density curves for all phases exhibit a marked decrease down to ca 3 GPa, followed by an increase with depth. It is under intermediate conditions (45 mW $m^{-2}$) and at $P > 1$ GPa that density curves exhibit most of the differences. Indeed, density curves for all mineral phases show a gentle decrease down to ca 1 GPa, where the density of olivine and pyroxenes starts to increase, whereas it continues to decrease down to ca 4.5 GPa for spinel, magnesiochromite and garnet.

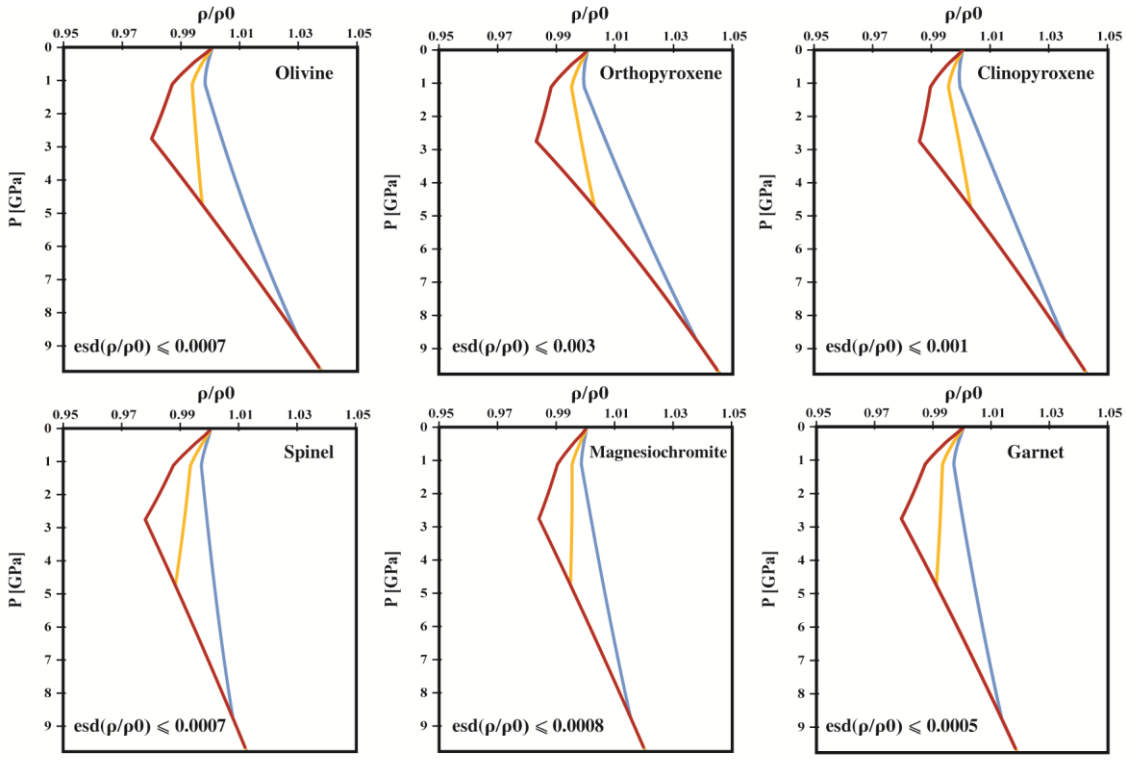


**Figure 4.1.** Density profiles ($\rho/\rho0$) for mineral phases in the studied peridotitic systems (olivine, orthopyroxene, clinopyroxene, spinel, magnesiochromite and garnet) calculated along a 35 mW $m^{-2}$ geotherm (blue curves), 45 mW $m^{-2}$ geotherm (yellow curves) and 60 mW $m^{-2}$ geotherm (red curves). The 35, 45 and 60 mW $m^{-2}$ conductive geotherms for density calculations are from Hasterok and Chapman (2011). Esd($\rho/\rho0$) (estimated standard deviation) refers to the uncertainties associated with EoS fitting (as calculated by the least-squares method) and density calculations. Note that these uncertainties are minimum.

Such distinct behaviour is clearly due to different elastic parameters (Table 4.1), but it is also due to the interplay between increasing temperature and pressure, whose effects are of the same order (see also considerations below). Noteworthy errors associated with density calculations through the newly developed and two selected EoS are minimum (Figure 4.1), and this in turn affects the accuracy of density profiles for bulk rocks. Such errors, esd($\rho/\rho0$) ~$10^{-3}$, translate to uncertainties of density calculations which are ~0.05 % (e.g., 3.416(2) g/$cm^3$ or conversely 3416(2) kg/$m^3$ at ~6 GPa and ~1050 °C for the fertile peridotitic system), which are considerably much less than average uncertainties associated to density

calculations. If we consider a geotherm of 35 mW $m^{-2}$ and both fertile and depleted compositions (Figures 4.2, 4.3), the density in the mantle shows a similar behaviour, progressively increasing with increasing depth. This indicates that the effect of pressure prevails over that of the slowly rising temperature. By comparing the trends of the fertile and depleted mantle sections (Figure 4.4), it is evident that the former is typified by a more pronounced density increase with respect to the depleted one. This is attributable to the higher modes of garnet (due to higher bulk $Al_2O_3$ in fertile compositions), which is among the densest mineral phases in peridotite assemblages (e.g., Lee, 2003).

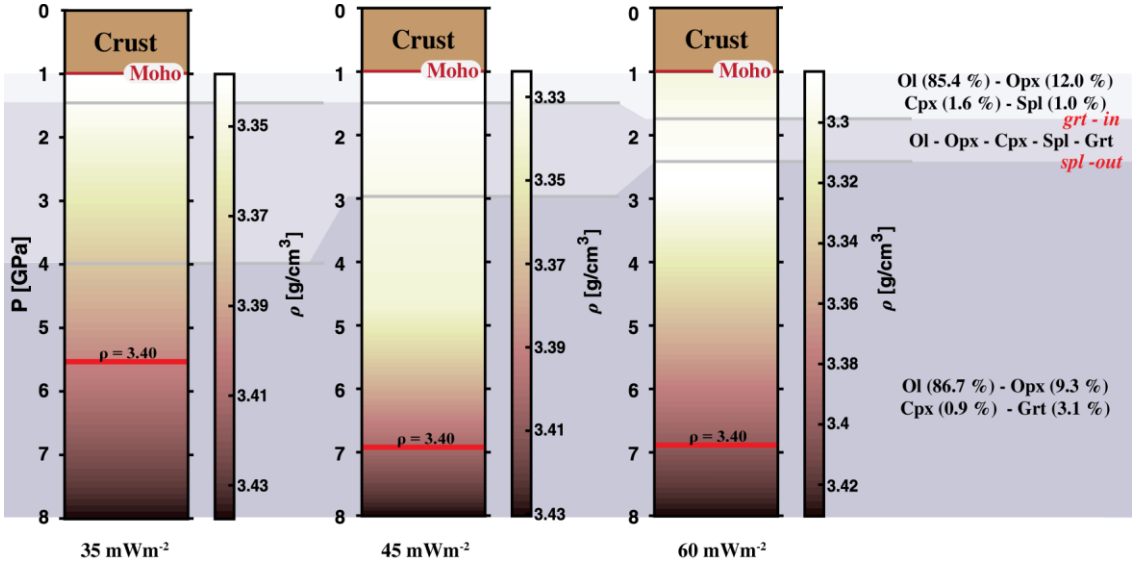


**Figure 4.2.** Density profiles for a depleted peridotitic systems calculated along 35, 45 and 60 mW $m^{-2}$ geotherms. Brown to yellow colour bar represents the density variations along the profiles. Grey lines subdivide the ideal mantle sections into the spinel, spinel + garnet and garnet stability fields, following a simplification of Ziberna et al. (2013) thermodynamic model. The iso-density line for $\rho$ = 3.40 g/$cm^3$ is shown for reference.

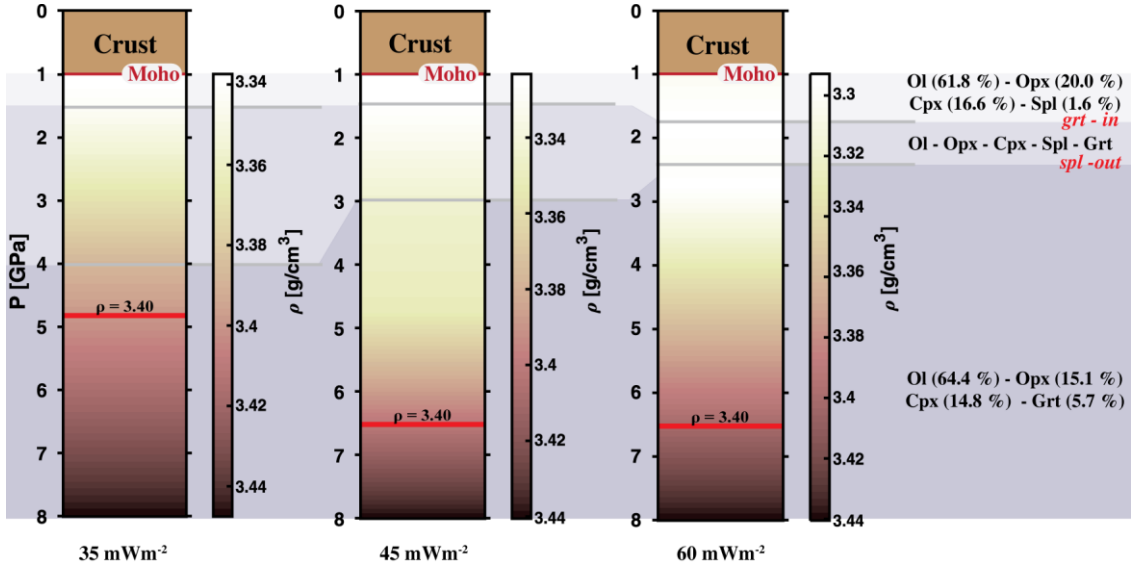

**Figure 4.3 (on the preceding page).** Density profiles for a fertile peridotitic systems calculated along 35, 45 and 60 mW $m^{-2}$ geotherms. Brown to yellow colour bar represents the density variations along the profiles. Grey lines subdivide the ideal mantle sections into the spinel, spinel + garnet and garnet stability fields, following a simplification of Ziberna et al. (2013) thermodynamic model. The iso-density line for $\rho$ = 3.40 g/$cm^3$ is shown for reference.

If we consider a geotherm of 45 mW $m^{-2}$, results are somehow different in the 1–4 GPa interval. Here, the density of the depleted peridotitic system remains nearly constant while it moderately increases for the fertile system; then the density of both systems increases from 4 down to 8 GPa (Figures 4.2, 4.3, 4.4). These results suggest that (i) the effect of temperature on the evolution of the bulk density with depth is comparable to that of pressure and that (ii) the behaviour of the two systems is decoupled down to ca 4 GPa.
If we consider a relatively hot geotherm of 60 mW $m^{-2}$, the temperature increase with depth is so strong that leads to an overall decrease of the bulk density of both depleted and fertile systems in the lithosphere from 1 to about 3 GPa, followed by an increase from 3 down to 8 GPa (Figure 4.2, 4.3). By comparing the trends of the two sections (Figure 4.4), the fertile system shows a more gentle decrease in its density compared to the depleted system. This is again attributable to the higher modes of garnet, which, combined with the *P–T* gradient effects, result in a slightly smoother density profile. Irrespective of the specific depth and width of their coexistence intervals, spinel and garnet have a stronger control on the density variations in case of fertile compositions, due to their higher modes.

## 4.3.3 Discussion

### 4.3.3.1 Density models and the effect of the thermal state

Most of the recently published upper mantle density models derive from phase equilibria calculations based on thermodynamic data, where stable mineral assemblages are computed using Gibbs free-energy minimization techniques. Previous works (Fullea et al., 2014; Ziberna and Klemme, 2016) showed some contrasting results as to whether the lithospheric density is predominantly controlled by the thermal state, bulk composition, or their interplay. Fullea et al. (2014) unravelled the present-day Irish lithospheric structure through LitMod3D code (Fullea et al., 2009) that combines petrological and geophysical observations with thermodynamic data (in the CFMAS system) within a self-consistent framework. This modelling revealed similar vertical density profiles – sharp spinel-garnet phase transition with an abrupt increase of density, a general trend of decreasing density down to ~100 km, followed by an increase (Figure 4.4) – associated with all the mantle compositions discussed in the work (i.e., from fertile to moderately depleted peridotites). Overall, these density

trends suggest a greater control of the thermal state on the lithospheric density rather than bulk composition in the Irish lithosphere (60 to 70 mW $m^{-2}$). Considering the lack of Cr (for which there is evidence that it may considerably change phase relations in the upper mantle) in most previous calculations, Ziberna and Klemme (2016) investigated the density variations for Cr-bearing mantle compositions (Pali-Aike xenoliths, Patagonia) in response to changes in bulk compositions and thermal gradients by means of well-established free energy minimization techniques, with thermodynamic calculations based on the internally consistent dataset of Holland and Powell (1998) complemented for the most relevant Cr-bearing phases in the upper mantle (Ziberna et al., 2013). Contrary to previous results (Fullea et al., 2014), this work showed that the density profiles across the spinel-garnet peridotite transition are not sharp and depend both on bulk composition (especially on $Al_2O_3$ and $Cr_2O_3$) and geothermal gradient (Figure 4.4). Moreover, while under relatively hot thermal conditions (70 mW $m^{-2}$) density profiles for both fertile and depleted compositions show similar trends (i.e., density decrease down to ca 2.5 GPa), this is not the case for intermediate thermal conditions (50 mW $m^{-2}$) where density in the mantle for depleted compositions remains virtually constant down to ca 4 GPa and it rapidly increases for more fertile compositions (Figure 4.4). Accordingly, these authors suggested that it is the interplay between bulk composition and thermal gradient that controls density variations in the lithospheric mantle.

Our models predict a much greater thermal control over the density of the lithospheric mantle, with some compositional control mostly arising at cold-intermediate thermal conditions (Figure 4.4). Considering that we based the spinel-garnet phase transitions on Ziberna et al. (2013) thermodynamic model (cf. Subsection 4.3.1), spinel and garnet coexist over a significant depth interval. Accordingly, our models predict a smooth variation of densities across the spinel-garnet transition and no abrupt changes. As already evidenced by Ziberna and Klemme (2016), the sharp spinel-garnet transitions associated with an abrupt change of density identified by Fullea et al. (2014) can be ascribed to the lack of Cr in their thermodynamic model. If this aspect is ruled out from further discussion, and density curves are analysed overall, there are some similarities with those from Fullea et al. (2014) (Figure 4.4). Indeed, all modelled compositions exhibit an overall decrease of the bulk density up to about 100 km, followed by an increase downwards, for relatively hot thermal conditions (60 to 70 mW $m^{-2}$). Our density curves show even more striking similarities with those from Ziberna and Klemme (2016), for which a similar behaviour is predicted for fertile and depleted compositions under relatively hot thermal conditions (70 mW $m^{-2}$), and a different one under intermediate conditions (50 mW $m^{-2}$) (Figure 4.4).

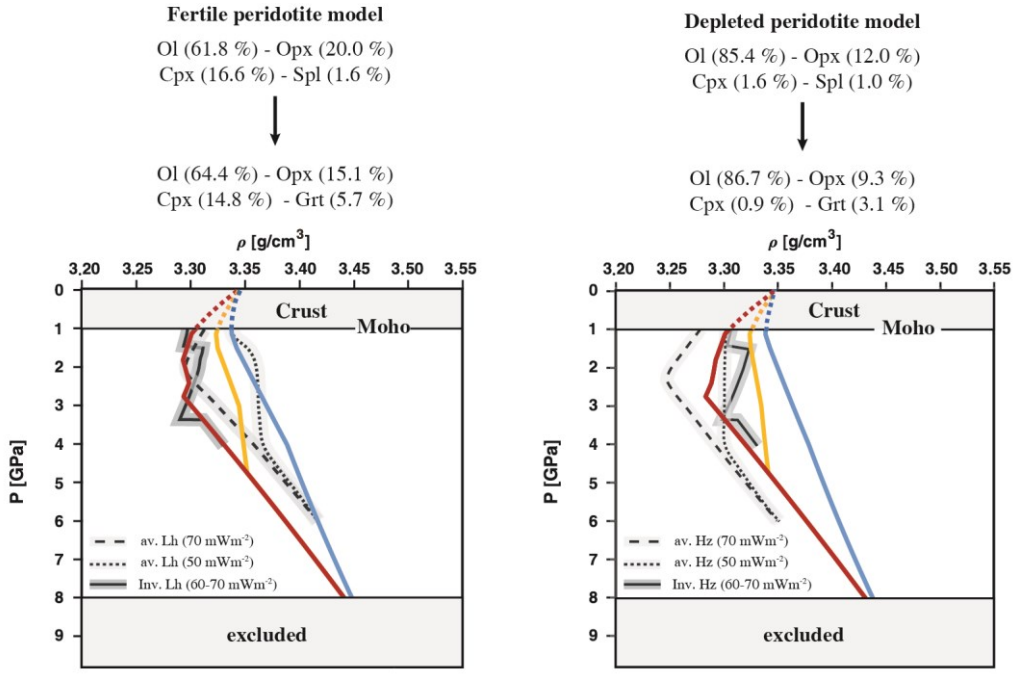


**Figure 4.4.** Comparison of density profiles for fertile (left panel) and depleted (right panel) peridotitic systems calculated along a 35 mW $m^{-2}$ geotherm (blue curves), 45 mW $m^{-2}$ geotherm (yellow curves) and 60 mW $m^{-2}$ geotherm (red curves). Density curves from previous literature are also shown: av. Lh (70 mW $m^{-2}$), av. Lh (50 mW $m^{-2}$), av. Hz (70 mW $m^{-2}$) and av. Hz (50 mW $m^{-2}$) are respectively the average density curves for fertile (TM16, BN4) and depleted (LS1, PA3) mantle xenoliths from Ziberna and Klemme (2016) calculated along the 70 mW $m^{-2}$ and 50 mW $m^{-2}$ geothermal gradients, whereas Inv. Lh (60–70 mW $m^{-2}$) and Inv. Hz (60–70 mW $m^{-2}$) are respectively the density curves of Inver lherzolite and harzburgite mantle xenoliths from Fullea et al. (2014) calculated under the Irish thermal state (60 to 70 mW $m^{-2}$).

Therefore, our investigation shows that density profiles in natural systems with simplified phase relations display comparable trends to those reported in previous studies. In this framework, perspectives are that the thermal gradient exerts substantial control when it comes to the density structure of the lithosphere and that the compositional control on the density evolution with depth may be less than previously suggested. In the next section, we show how density calculations based on simplified phase relations can be reconciled with Perple_X-based results from previous literature. We also infer that the thermal gradient is the main controlling variable of the lithospheric mantle density.

### 4.3.3.2 Comparison between Perple_X and simplified calculations

Although a strict evaluation of similarities and differences of our simplified parameterisation for calculating density variations with respect to classic thermodynamic modelling (e.g., Perple_X) goes beyond the scope of this paper (detailed results of the application of both models to a real mantle section will be presented elsewhere), in the following we provide an application of our model compared with previous results from literature (Ziberna and

Klemme, 2016). To this aim, we selected two of the four representative mantle xenoliths from Pali-Aike, Patagonia, reported in Ziberna and Klemme (2016), namely PA3 (spinel harzburgite) and BN4 (spinel-garnet lherzolite), for which we computed density profiles along the 50 and 70 mW $m^{-2}$ geothermal gradients (Figure 4.5). Input data for Ziberna and Klemme (2016) thermodynamic modelling are whole-rock analyses from Stern et al. (1999), with calculations performed in the $SiO_2$-$Al_2O_3$-$Cr_2O_3$-FeO-MgO-CaO-$Na_2O$ system. In order to provide a clear and consistent comparison between the two methods, input data (i.e., mineral compositions and modes) for our simplified parameterisation were as follows. Olivine, pyroxenes, and spinel mineral compositions and modes were selected from Perple_X calculations of Ziberna and Klemme (2016) at 1 GPa (at the corresponding temperature for the 50 and 70 mW $m^{-2}$ geothermal gradients). Garnet compositions were selected from Perple_X calculations of Ziberna and Klemme (2016) at *P–T* corresponding to spinel-out reaction (which depends on bulk composition and geothermal gradient); garnet, as well as olivine and pyroxenes modes in the garnet stability field, were calculated from stoichiometric balance upon completion of the reaction spinel + pyroxenes = garnet + olivine, using the selected mineral modes and compositions. Selected mineral compositions were kept fixed along the whole section; mineral modes were kept fixed in spinel and garnet stability fields, and were imposed to vary linearly in the spinel-garnet stability field (cf. Section 4.1). Depth intervals of coexistence of spinel + garnet were selected again from Perple_X calculations of Ziberna and Klemme (2016). Density variations with depth and thermal regime for PA3 (spinel harzburgite) and BN4 (spinel-garnet lherzolite) mantle xenoliths are reported in Figure 4.5, along with original curves from Ziberna and Klemme (2016).

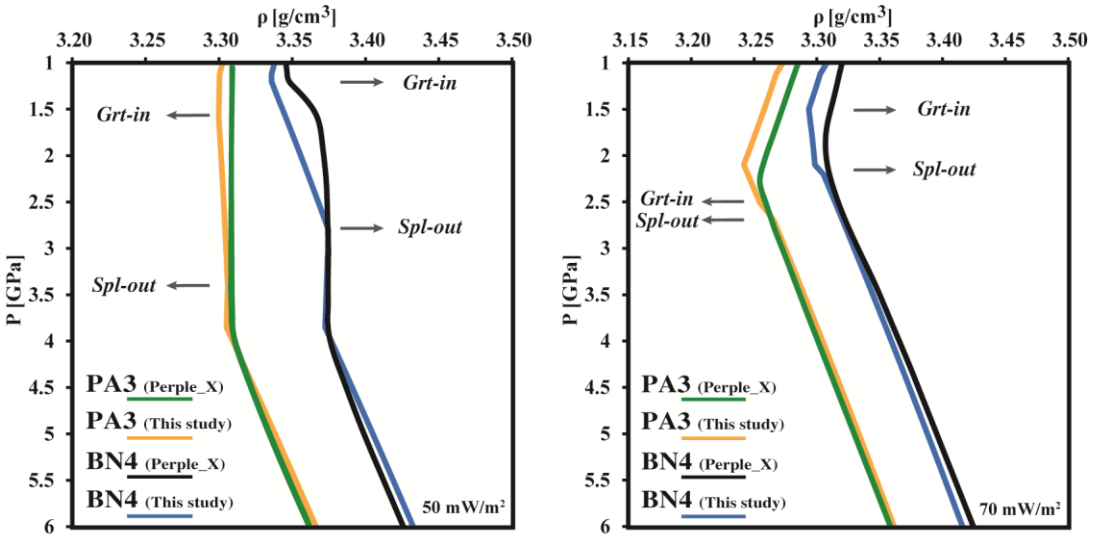

**Figure 4.5 (on the preceding page).** Density profiles for PA3 (spinel harzburgite) and BN4 (spinel-garnet lherzolite) mantle xenoliths calculated along the 50 and 70 mW $m^{-2}$ geothermal gradients following our simplified parameterisation in comparison with Perple_X-based original curves from Ziberna and Klemme (2016). Note the similarities between the two distinct sets of curves, both in their general trends and absolute values, as the density difference is always < 20 $kg/m^3$.

Note that Ziberna and Klemme (2016) thermodynamic model considered phase equilibria, with mineral modes and compositions continuously changing according to *P–T* conditions, which has not been done in this study. Nonetheless, density curves calculated with our simplified parameterisation match well those from Ziberna and Klemme (2016), both in their general trends with depth and absolute values, with a maximum difference between the two models of ca 20 $kg/m^3$ (Figure 4.5). From this similarity, we conclude that our approach with simplified phase relations has enough accuracy for investigating the density structure of the lithosphere. We also infer that the density structure of the lithospheric mantle is predominantly controlled by the thermal gradient variations, with most of the compositional control arising at cold-intermediate thermal conditions. No less importantly, we showed that the newly developed *P–V–T–K* EoS (pyroxenes, spinel and garnet) in combination with the published EoS for mantle olivine and mantle magnesiochromite are applicable for calculating the density of mantle peridotites and its variation, with minimum uncertainties, under different thermal regimes and bulk compositions, without requiring sets of end-member properties and solution models.

## 4.4 Concluding remarks

In this study, we presented an assessment of the thermoelastic parameters of orthopyroxene, clinopyroxene, spinel and garnet based on X-Ray diffraction data and direct elastic measurements available in literature. The newly developed EoS consistently describe the elastic behaviour of these phases under the most relevant *P–T* conditions and bulk compositions of the Earth's mantle, along with the published EoS for mantle olivine and magnesiochromite.

As a case study, we evaluated the influence of bulk composition and thermal regimes on the density structure of potential lithospheric mantle sections, following a simplified parameterisation that does not incorporate phase relations. Accordingly, density profiles for fertile and depleted peridotitic systems based on the EoS of their constituent mineral phases were calculated for three different geothermal gradients (35, 45 and 60 mW $m^{-2}$), for a *P–T* range of 1–8 GPa and 350–1375 °C. In case of very cold geotherms (35 mW $m^{-2}$), the density of both depleted and fertile systems progressively increases with increasing depth. In case

of intermediate geotherms (45 mW $m^{-2}$), the density of a depleted peridotitic system remains nearly constant up to about 4 GPa, while it moderately increases in a fertile system, due to higher modes of garnet. In case of relatively hot geotherms (60 mW $m^{-2}$), the density of both depleted and fertile systems progressively decreases with increasing depth, up to about 3 GPa, and then increases downwards. Moreover, we also provided an example of application of our model in comparison with classic thermodynamic modelling results from literature. From such comparison, we concluded that (i) density profiles for mantle sections can be computed with enough accuracy following our simplified parameterisation, (ii) the thermal gradient exerts substantial control when it comes to the density structure of the lithosphere and (iii) the compositional control on the density evolution with depth may be less than previously suggested.

## Author contribution

[L.F.] Methodology, Formal analysis, Investigation, Data Curation, Writing-Original Draft, Writing-Review & Editing; [B.F.]: Investigation, Writing-Review & Editing; [F.C.]: Investigation, Writing-Review & Editing; [M.M.]: Conceptualization, Writing-Review & Editing, Supervision; [F.N.]: Conceptualization, Methodology, Writing-Review & Editing, Supervision; [M.C.]: Conceptualization, Writing-Review & Editing, Supervision.

## Acknowledgments

Dr. Luca Ziberna is thanked for providing work files that allowed a validation of our simplified parameterisation for calculating density variations with respect to Perple_X models. The authors are grateful to Michel Grégoire and an anonymous reviewer for their constructive comments, which improved an earlier version of the manuscript. Michael Roden is acknowledged for his careful editorial handling and guidance.

## Funding

L.F. acknowledges Istituto Nazionale di Geofisica e Vulcanologia (INGV) for funding his Ph.D. project (XXXV cycle) with thematic ‘Links between rheology, mineralogy and composition of the Earth’s mantle’ and the Italian National Research Program (PRIN Grant 20178LPCPW ‘Micro to Macro - How to unravel the nature of the Large Magmatic Events’ to [M.C.])

# Appendix A. Supplementary data

Supplementary data to this article can be found online at https://doi.org/10.1016/j.lithos.2021.106483.

# References


Abers, G.A., Hacker, B.R., 2016. A MATLAB toolbox and Excel workbook for calculating the densities, seismic wave speeds, and major element composition of minerals and rocks at pressure and temperature. Geochem. Geophys. Geosyst. 17, 616–624.

Afonso, J.C., Ranalli, G., Fernàndez, M., 2007. Density structure and buoyancy of the oceanic lithosphere revisited. Geophys. Res. Lett. 34, 2–6.

Afonso, J.C., Fernàndez, M., Ranalli, G., Griffin, W.L., Connolly, J.A.D., 2008. Integrated geophysical-petrological modeling of the lithosphere and sublithospheric upper mantle: Methodology and applications. Geochem. Geophys. Geosyst. 9.

Afonso, J.C., Fullea, J., Yang, Y., Connolly, J.A.D., Jones, A.G., 2013. 3-D multiobservable probabilistic inversion for the compositional and thermal structure of the lithosphere and upper mantle. II: General methodology and resolution analysis. J. Geophys. Res. Solid Earth 118, 1650–1676.

Anderson, O.L., 1995. Equations of state of solids for geophysics and ceramic science. Oxf. Monogr. Geol. Geophys.

Angel, R.J., 2000. Equations of State. Rev. Mineral. Geochem. 41, 35–59.

Angel, R.J., Jackson, J.M., 2002. Elasticity and equation of state of orthoenstatite, MgSiO3. Am. Mineral. 87, 558–561.

Angel, R.J., Alvaro, M., Gonzalez-Platas, J., 2014. EosFit7c and a Fortran module (library) for equation of state calculations. Zeitschrift für Krist. - Cryst. Mater. 229, 405–419.

Angel, R.J., Alvaro, M., Nestola, F., 2018. 40 years of mineral elasticity: a critical review and a new parameterisation of equations of state for mantle olivines and diamond inclusions. Phys. Chem. Miner. 45, 95–113.

Babuska, V., Fiala, J., Kumazawa, M., Ohno, I., Sumino, Y., 1978. Elastic properties of garnet solid-solution series. Phys. Earth Planet. Inter. 16, 157–176.

Bass, J.D., Anderson, D.L., 1984. Composition of the upper mantle: Geophysical tests of two petrological models. Geophys. Res. Lett. 11, 229–232.

Beccaluva, L., Bonadiman, C., Coltorti, M., Salvini, L., Siena, F., 2001. Depletion events, nature of metasomatizing agent and timing of enrichment processes in lithospheric mantle xenoliths from the Veneto Volcanic Province. J. Petrol. 42, 173–188.

Bosenick, A., Geiger, C.A., 1997. Powder X ray diffraction study of synthetic pyrope grossular garnets between 20 and 295 K. J. Geophys. Res. Solid Earth 102, 22649–22657.

Braun, J., 2010. The many surface expressions of mantle dynamics. Nat. Geosci. 3, 825–833.

Brown, J.M., Collins, M.D., 1998. Elasticity of an upper mantle clinopyroxene. Phys. Chem. Miner. 26, 7–13.

Cameron, M., Sueno, S., Prewitt, C.T., Papike, J.J., 1973. High-Temperature crystal chemistry of acmite, diopside, hedenbergite, jadeite, spodumene, and ureyite. Am. Mineral. 58, 594–618.

Capitanio, F., Morra, G., Goes, S., 2007. Dynamic models of downgoing plate-buoyancy driven subduction: Subduction motions and energy dissipation. Earth Planet. Sci. Lett. 262, 284–297.

Carbonin, S., Martignago, F., Menegazzo, G., Dal Negro, A., 2002. X-ray single-crystal study of spinels: in situ heating. Phys. Chem. Miner. 29, 503–514.

Chai, M., Brown, J.M., Slutsky, L.J., 1997. The elastic constants of an aluminous orthopyroxene to 12.5 GPa. J. Geophys. Res. Solid Earth 102, 14779–14785.
Coltorti, M., Bonadiman, C., Hinton, R.W., Siena, F., Upton, B.G.J., 1999. Carbonatite metasomatism of the oceanic upper mantle: evidence from clinopyroxenes and glasses in ultramafic xenoliths of Grande Comore, Indian Ocean. J. Petrol. 40, 133–165.
Coltorti, M., Bonadiman, C., Casetta, F., Faccini, B., Giacomoni, P.P., Pelorosso, B., Perinelli, C., 2021. Nature and evolution of the northern Victoria Land lithospheric mantle (Antarctica) as revealed by ultramafic xenoliths. Geol. Soc. Lond. Mem. 56
Comodi, P., Princivalle, F., Tirone, M., Zanazzi, P.F., 1995. Comparative compressibility of clinopyroxenes from mantle nodules. Eur. J. Mineral. 7, 141–150.
Connolly, J.A.D., 2009. The geodynamic equation of state: What and how. Geochem. Geophys. Geosyst. 10, Q10014.
Connolly, J.A.D., Petrini, K., 2002. An automated strategy for calculation of phase diagram sections and retrieval of rock properties as a function of physical conditions. J. Metamorph. Geol. 20, 697–708.
Fullea, J., Afonso, J.C., Connolly, J.A.D., Fernàndez, M., García-Castellanos, D., Zeyen, H., 2009. LitMod3D: An interactive 3-D software to model the thermal, compositional, density, seismological, and rheological structure of the lithosphere and sublithospheric upper mantle. Geochem. Geophys. Geosyst. 10.
Fullea, J., Muller, M.R., Jones, A.G., Afonso, J.C., 2014. The lithosphere–asthenosphere system beneath Ireland from integrated geophysical–petrological modeling II: 3D thermal and compositional structure. Lithos 189, 49–64.
Gatta, G.D., Rinaldi, R., Knight, K.S., Molin, G., Artioli, G., 2007. High temperature structural and thermoelastic behaviour of mantle orthopyroxene: an in situ neutron powder diffraction study. Phys. Chem. Miner. 34, 185–200.
Gillet, P., Fiquetw, G., Malézieux, J.M., Geiger, C.A., 1992. High-pressure and high-temperature Raman spectroscopy of end-member garnets: pyrope, grossular and andradite. Eur. J. Mineral. 4, 651–664.
Grimes, N.W., Al-Ajaj, E.A., 1992. Low-temperature thermal expansion of spinel. J. Phys. Condens. Matter 4, 6375–6380.
Hacker, B.R., Abers, G.A., 2004. Subduction Factory 3: An Excel worksheet and macro for calculating the densities, seismic wave speeds, and H2O contents of minerals and rocks at pressure and temperature. Geochem. Geophys. Geosyst. 5.
Hasterok, D., Chapman, D.S., 2011. Heat production and geotherms for the continental lithosphere. Earth Planet. Sci. Lett. 307, 59–70.
Holland, T.J.B., Powell, R., 1998. An internally consistent thermodynamic data set for phases of petrological interest. J. Metamorph. Geol. 16, 309–343.
Holland, T.J.B., Powell, R., 2011. An improved and extended internally consistent thermodynamic dataset for phases of petrological interest, involving a new equation of state for solids. J. Metamorph. Geol. 29, 333–383.
Hugh-Jones, D.A., Angel, R.J., 1997. Effect of Ca2+ and Fe2+ on the equation of state of MgSiO3 orthopyroxene. J. Geophys. Res. Solid Earth 102, 12333–12340.
Hugh-Jones, D., Chopelas, A., Augel, R., 1997. Tetrahedral compression in (Mg,Fe)SiO3 orthopyroxenes. Phys. Chem. Miner. 24, 301–310.
Isaak, D.G., Ohno, I., Lee, P.C., 2006. The elastic constants of monoclinic single-crystal chrome-diopside to 1,300 K. Phys. Chem. Miner. 32, 691–699.
Jiang, F., Speziale, S., Duffy, T.S., 2004. Single-crystal elasticity of grossular- and almandine-rich garnets to 11 GPa by Brillouin scattering. J. Geophys. Res. Solid Earth 109, 1–10.
Klemme, S., O'Neill, H.S., 2000. The near-solidus transition from garnet lherzolite to spinel lherzolite. Contrib. Mineral. Petrol. 138, 237–248.

Lee, C.-T.A., 2003. Compositional variation of density and seismic velocities in natural peridotites at STP conditions: Implications for seismic imaging of compositional heterogeneities in the upper mantle. J. Geophys. Res. Solid Earth 108, 2441.
Li, B., Neuville, D.R., 2010. Elasticity of diopside to 8 GPa and 1073 K and implications for the upper mantle. Phys. Earth Planet. Inter. 183, 398–403.
Lu, C., Mao, Z., Lin, J.-F., Zhuravlev, K.K., Tkachev, S.N., Prakapenka, V.B., 2013. Elasticity of single-crystal iron-bearing pyrope up to 20GPa and 750K. Earth Planet. Sci. Lett. 361, 134–142.
Martignago, F., Negro, A.D., Carbonin, S., 2003. How Cr3+ and Fe3+ affect Mg-Al order-disorder transformation at high temperature in natural spinels. Phys. Chem. Miner. 30, 401–408.
Mazzucchelli, M., Rivalenti, G., Brunelli, D., Zanetti, A., Boari, E., 2009. Formation of highly refractory dunite by focused percolation of pyroxenite-derived melt in the Balmuccia Peridotite Massif (Italy). J. Petrol. 50, 1205–1233.
Matsukage, K.N., Kikuchi, S., Ono, S., Nishihara, Y., Kikegawa, T., 2010. Density and seismic velocities of chromitite body in oceanic mantle peridotite. Am. Mineral. 95, 1422–1428.
McDonough, W.F., Rudnick, R.L., 1998. Mineralogy and composition of the upper mantle. Rev. Mineral. 37, 139–164.
Melchiorre, M., Faccini, B., Grégoire, M., Benoit, M., Casetta, F., Coltorti, M., 2020. Melting and metasomatism/refertilisation processes in the Patagonian subcontinental lithospheric mantle: a review. Lithos 354–355, 105324.
Milani, S., Nestola, F., Alvaro, M., Pasqual, D., Mazzucchelli, M.L., Domeneghetti, M.C., Geiger, C.A., 2015. Diamond–garnet geobarometry: the role of garnet compressibility and expansivity. Lithos 227, 140–147.
Milani, S., Angel, R.J., Scandolo, L., Mazzucchelli, M.L., Ballaran, T.B., Klemme, S., Domeneghetti, M.C., Miletich, R., Scheidl, K.S., Derzsi, M., Tokàr, K., Prencipe, M., Alvaro, M., Nestola, F., 2017. Thermo-elastic behavior of grossular garnet at high pressures and temperatures. Am. Mineral. 102, 851–859.
Nestola, F., Ballaran, T.B., Balic-Zunic, T., Princivalle, F., Secco, L., Dal Negro, A., 2007. Comparative compressibility and structural behavior of spinel MgAl2O4 at high pressures: the independency on the degree of cation order. Am. Mineral. 92, 1838–1843.
Nestola, F., Periotto, B., Anzolini, C., Andreozzi, G.B., Woodland, A.B., Lenaz, D., Alvaro, M., Princivalle, F., 2015. Equation of state of hercynite, FeAl2O4, and high-pressure systematics of Mg-Fe-Cr-Al spinels. Mineral. Mag. 79, 285–294.
Nestola, F., Zaffiro, G., Mazzucchelli, M.L., Nimis, P., Andreozzi, G.B., Periotto, B., Princivalle, F., Lenaz, D., Secco, L., Pasqualetto, L., Logvinova, A.M., Sobolev, N.V., Lorenzetti, A., Harris, J.W., 2019. Diamond-inclusion system recording old deep lithosphere conditions at Udachnaya (Siberia). Sci. Rep. 9, 12586.
Ono, K., Harada, Y., Yoneda, A., Yamamoto, J., Yoshiasa, A., Sugiyama, K., Arima, H., Watanabe, T., 2018. Determination of elastic constants of single-crystal chromian spinel by resonant ultrasound spectroscopy and implications for fluid inclusion geobarometry. Phys. Chem. Miner. 45, 237–247.
Pandolfo, F., Camara, F., Domeneghetti, M.C., Alvaro, M., Nestola, F., Karato, S.-I., Amulele, G., 2015. Volume thermal expansion along the jadeite–diopside join. Phys. Chem. Miner. 42, 1–14.
Pearson, D.G., Canil, D., Shirey, S.B., 2003. Mantle samples included in volcanic rocks: xenoliths and diamonds. In: Treatise on Geochemistry. Elsevier, pp. 171–275.
Prencipe, M., Tribaudino, M., Pavese, A., Hoser, A., Reehuis, M., 2000. A single-crystal neutron-diffraction investigation of diopside at 10 K. Can. Mineral. 38, 183–189.
Sang, L., Bass, J.D., 2014. Single-crystal elasticity of diopside to 14GPa by Brillouin scattering. Phys. Earth Planet. Inter. 228, 75–79.

Scandolo, L., Mazzucchelli, M.L., Alvaro, M., Nestola, F., Pandolfo, F., Domeneghetti, M. C., 2015. Thermal expansion behaviour of orthopyroxenes: the role of the Fe-Mn substitution. Mineral. Mag. 79, 71–87.
Schutt, D.L., Lesher, C.E., 2006. Effects of melt depletion on the density and seismic velocity of garnet and spinel lherzolite. J. Geophys. Res. Solid Earth 111.
Simon, N.S.C., Podladchikov, Y.Y., 2008. The effect of mantle composition on density in the extending lithosphere. Earth Planet. Sci. Lett. 272, 148–157.
Speziale, S., Nestola, F., Jiang, F., Duffy, T.S., 2016. Single-crystal elastic constants of spinel (MgAl2O4) to 11.1 GPa by Brillouin scattering. In: AGU Fall Meeting Abstracts (pp. MR23A-2658).
Stern, C.R., Kilian, R., Olker, B., Hauri, E.H., Kurtis Kyser, T., 1999. Evidence from mantle xenoliths for relatively thin (<100 km) continental lithosphere below the Phanerozoic crust of southernmost South America. Lithos 48, 217–235
Stixrude, L., Lithgow-Bertelloni, C., 2005a. Mineralogy and elasticity of the oceanic upper mantle: Origin of the low-velocity zone. J. Geophys. Res. 110, B03204.
Stixrude, L., Lithgow-Bertelloni, C., 2005b. Thermodynamics of mantle minerals - I. Physical properties. Geophys. J. Int. 162, 610–632.
Stixrude, L., Lithgow-Bertelloni, C., 2011. Thermodynamics of mantle minerals - II. Phase equilibria. Geophys. J. Int. 184, 1180–1213.
Sumino, Y., Nishizawa, O., 1978. Temperature variation of elastic constants of pyrope-almandine garnets. J. Phys. Earth 26, 239–252.
Suzuki, I., Anderson, O.L., 1983. Elasticity and thermal expansion of a natural garnet up to 1,000K. J. Phys. Earth 31, 125–138.
Suzuki, I., Ohno, I., Anderson, O.L., 2000. Harmonic and anharmonic properties of spinel MgAl 2 O 4. Am. Mineral. 85, 304–311.
Thybo, H., Artemieva, I.M., 2013. Moho and magmatic underplating in continental lithosphere. Tectonophysics 609, 605–619.
Wood, B.J., Kiseeva, E.S., Matzen, A.K., 2013. Garnet in the Earth's Mantle. Elements 9, 421–426.
Xu, J., Zhang, D., Dera, P., Zhang, B., Fan, D., 2017. Experimental evidence for the survival of augite to transition zone depths, and implications for subduction zone dynamics. Am. Mineral. 102, 1516–1524.
Xu, Z., Ma, M., Li, B., Hong, X., 2019. Compressibility and thermal expansion of natural clinopyroxene Di0.66Hd0.13Jd0.12Ts0.05. Results Phys. 12, 447–453.
Yang, H., Ghose, S., 1994. Thermal expansion, Debye temperature and Gruneisen parameter of synthetic (Fe,Mg)SiO3 orthopyroxenes. Phys. Chem. Miner. 20, 575–586.
Zha, C., Duffy, T.S., Downs, R.T., Mao, H., Hemley, R.J., 1998. Brillouin scattering and Xray diffraction of San Carlos olivine: direct pressure determination to 32 GPa. Earth Planet. Sci. Lett. 159, 25–33.
Zhang, J.S., Bass, J.D., 2016. Single-crystal elasticity of natural Fe-bearing orthoenstatite across a high-pressure phase transition. Geophys. Res. Lett. 43, 8473–8481.
Ziberna, L., Klemme, S., 2016. Application of thermodynamic modelling to natural mantle xenoliths: examples of density variations and pressure–temperature evolution of the lithospheric mantle. Contrib. Mineral. Petrol. 171, 16.
Ziberna, L., Klemme, S., Nimis, P., 2013. Garnet and spinel in fertile and depleted mantle: insights from thermodynamic modelling. Contrib. Mineral. Petrol. 166, 411–421.

# 5. Sound velocities and single-crystal elasticity of hydrous Fo90 olivine to 12 GPa

Luca FACCINCANI [1,2,✉], Giacomo CRINITI [3], Alexander KURNOSOV [3], Tiziana BOFFA BALLARAN [3], Anthony C. WITHERS [3], Maurizio MAZZUCCHELLI [4], Fabrizio NESTOLA [5] and Massimo COLTORTI [1,2,6]

[1] Department of Physics and Earth Sciences, University of Ferrara, Via Saragat 1, 44122 Ferrara, Italy
[2] Department of Environmental and Prevention Sciences, University of Ferrara, C.so Ercole I D'Este 32, 44121 Ferrara, Italy
[3] Bayerisches Geoinstitut, University of Bayreuth, Universitätsstraße 30, 95440 Bayreuth, Germany
[4] Department of Chemical and Geological Sciences, University of Modena and Reggio Emilia, Via Campi 103, 41125 Modena, Italy
[5] Department of Geosciences, University of Padua, Via Gradenigo 6, 35131 Padua, Italy
[6] Istituto Nazionale di Geofisica e Vulcanologia (INGV) Sezione di Palermo, Via Ugo la Malfa 153, 90146 Palermo, Italy
✉ luca.faccincani@unife.it

This chapter has been published as:
Faccincani et al. (2023) *Physics of the Earth and Planetary Interiors*, **337**, 107011.

## Abstract

Nominally anhydrous minerals (NAMs) may contain significant amounts of water and constitute an important reservoir for mantle hydrogen. The colloquial term 'water' in NAMs is related to the presence of hydroxyl-bearing ($OH^-$) point defects in their crystal structure, where hydrogen is bonded to lattice oxygen and is charge-balanced by cation vacancies. This hydrous component may therefore have substantial effects on the thermoelastic parameters of NAMs, comparable to other major crystal-chemical substitutions (e.g., Fe, Al). Assessment of water concentrations in natural minerals from mantle xenoliths indicates that olivine commonly stores ~0–200 ppm of water. However, the lack of samples originating from depths exceeding ~250 km coupled with the rapid diffusion of hydrogen in olivine at magmatic temperatures makes the determination of the olivine water content in the upper mantle challenging. On the other hand, numerous experimental data show that, at pressures and temperatures corresponding to deep upper mantle conditions, the water storage capacity of olivine increases to 0.2–0.5 wt.%. Therefore, determining the elastic properties of olivine samples with more realistic water contents for deep upper mantle conditions may help in interpreting both seismic velocity anomalies in potentially hydrous regions of Earth's mantle as well as the observed seismic velocity and density contrasts across the 410-km discontinuity.

Here, we report simultaneous single-crystal X-ray diffraction and Brillouin scattering experiments at room temperature up to 11.96(2) GPa on hydrous [0.20(3) wt.% $H_2O$] Fo90 olivine to assess its full elastic tensor, and complement these results with a careful re-analysis of all the available single-crystal elasticity data from the literature for anhydrous Fo90 olivine. While the bulk ($K$) and shear ($G$) moduli of hydrous Fo90 olivine are virtually identical to those of the corresponding anhydrous phase, their pressure derivatives $K'$ and $G'$ are slightly larger, although consistent within mutual uncertainties. We then defined linear relations between the water concentration in Fo90 olivine, the elastic moduli and their pressure derivatives, which were then used to compute the sound velocities of Fo90 olivine with higher degrees of hydration. Even for water concentrations as high as 0.5 wt.%, the sound wave velocities of hydrous and anhydrous olivines were found to be identical within uncertainties at pressures corresponding to the base of the upper mantle. Contrary to previous claims, our data suggest that water in olivine is not seismically detectable, at least for contents consistent with deep upper mantle conditions. In addition to that, our data reveal that the hydration of olivine is unlikely to be a key factor in reconciling seismic velocity and density contrasts across the 410-km discontinuity with a pyrolitic mantle.

**Keywords:** hydrous olivine, Brillouin scattering, elasticity, high pressure; NAMs

## 5.1 Introduction

Although commonly referred to as nominally anhydrous minerals (NAMs), the dominant phases of Earth's upper mantle may contain significant amounts of water (e.g., Bell and Rossman, 1992). The occurrence of water in NAMs is closely related to the presence of hydrogen in their crystal structures, which is bonded to oxygen atoms forming hydroxyl-bearing ($OH^-$) point defects, and its incorporation is typically charge-balanced by the formation of cation vacancies. Olivine, α-$(Mg,Fe)_2SiO_4$, is considered to be the most abundant mineral of Earth's upper mantle and to constitute about 60 vol.% of pyrolitic phase assemblages (Ringwood, 1975). The water concentration detected in natural olivine samples from mantle xenoliths is generally low, in the order of 0–200 ppm wt. (Beran and Libowitzky, 2006; Novella et al., 2015; Peslier et al., 2010). Although a growing body of water analyses of olivine is available in the literature (Bonadiman et al., 2009; Peslier, 2010; Xia et al., 2010, etc.), trends between water content and its distribution across different geological settings are still difficult to determine, as well as the actual abundance of water in olivine in the upper mantle. This is due to both the rapid diffusion of hydrogen in olivine

at magmatic temperatures (e.g., Demouchy and Mackwell, 2006), which leads to partial dehydration of olivine in mantle xenoliths during their ascent, and the lack of xenoliths originating from depths greater than ~250 km. Even though the fast ascent of kimberlite magmas should prevent dehydration in olivine during xenolith transport (Demouchy et al., 2006; Peslier et al., 2008), in contrast to olivines from xenoliths found in alkali basalts which are commonly affected by H loss (e.g., Peslier et al., 2008), our understanding of how the water content of olivines changes as a function of depth largely relies on experimental studies. Indeed, a plethora of experimental data on water solubility in olivines at pressures and temperatures relevant to the upper mantle are available and indicate much higher water contents compared to those detected in natural olivine samples, especially at deep upper mantle conditions where the water storage capacity of olivine increases to 0.2–0.5 wt.% (e.g., Férot and Bolfan-Casanova, 2012; Hirschmann et al., 2005; Mosenfelder, 2006). Therefore, synthetic olivine samples with a more realistic water content expected for deep upper mantle conditions warrant investigation, as this may improve our understanding of various geodynamic processes operating on Earth (Regenauer-Lieb, 2006).

Water incorporation in olivine, even in trace amounts, has long been known to have substantial effects on its physical and chemical properties, such as atomic diffusivity, electrical conductivity, thermal conductivity, rheology, and melting (e.g., Chang et al., 2017; Costa and Chakraborty, 2008; Inoue, 1994; Jung and Karato, 2001; Smyth et al., 2006). From a crystal-chemical perspective, hydrogen incorporation in the crystal structure of olivine may occur both in the octahedral M sites, $Mg^{2+} \leftrightarrow 2H^{+}$, and in tetrahedral T sites, $Si^{4+} \leftrightarrow 4H^{+}$ (e.g., Brodholt and Refson, 2000; Hushur et al., 2009; Smyth et al., 2006). Previous experimental studies about the substitution mechanism of water in olivine showed contrasting results, although it was recognized that the synthesis conditions (pressure and $SiO_2$ activity) were influencing factors (e.g., Bali et al., 2008; Férot and Bolfan-Casanova, 2012; Matveev et al., 2001; Withers and Hirschmann, 2008). However, recent electron microprobe (EPMA) data coupled with transmission Fourier transform infrared spectroscopy (FTIR) analyses (Fei and Katsura, 2020), solid-state nuclear magnetic resonance (NMR) spectroscopy (Xue et al., 2017), and first-principles calculations studies (Umemoto et al., 2011; Xue et al., 2017) suggest that hydrogen substitution in olivine mainly occurs at the T sites at high pressure. Therefore, hydrogen incorporation in the M sites can be ruled out from being the predominant substitution mechanism in olivine under typical mantle conditions, as its occurrence is restricted to shallow depths ($\leq$ 80 km) and high $SiO_2$ activity (Bali et al., 2008; Fei and Katsura, 2020; Withers et al., 2011).

Despite its possible geophysical relevance, the effect of water on the elastic properties of olivine has been poorly constrained. The only elasticity measurements available in the literature were conducted by Mao et al. (2010) on hydrous (0.89 wt.% $H_2O$) end-member forsterite (Fo100) single crystals up to 14 GPa and by Jacobsen et al. (2008, 2009) on hydrous (0.8 wt.% $H_2O$) Fo97 olivine single crystals at ambient pressure. These works showed that the incorporation of water into pure forsterite and near end-member compositions is accompanied by a considerable reduction of the adiabatic bulk ($K_S$) and shear ($G$) moduli at ambient conditions. However, owing to the much larger moduli pressure derivatives of the hydrated samples, $K_S$ and $G$ of the hydrous Fo100 at high pressure are greater than those of the corresponding anhydrous phase (Mao et al., 2010). Nonetheless, the effect of hydration on the elasticity of the more relevant Fo90 olivine mantle composition remains largely unconstrained because no experimental data are available. Furthermore, previous works studied hydrous samples containing 0.8–0.9 wt.% $H_2O$, which is well above the expected water content for olivine at deep upper mantle conditions (e.g., Férot and Bolfan-Casanova, 2012; Hirschmann et al., 2005; Mosenfelder, 2006).

In this work, we set out to investigate the effect of hydration on the elastic properties of hydrous Fo90 olivine samples with more realistic water content for deep upper mantle conditions, as it may help in interpreting both seismic velocity anomalies in potentially hydrous regions of Earth's mantle as well as the observed seismic velocity and density contrasts across the 410-km discontinuity. To this aim, we performed simultaneous single-crystal X-ray diffraction (SCXRD) and Brillouin scattering measurements at room temperature up to 11.96(2) GPa on hydrous [0.20(3) wt.% $H_2O$] Fo90 olivine to constrain its full elastic tensor. By comparing our new accurate data with those available from literature for anhydrous Fo90 olivine, we evaluated the combined effect of $H_2O$ and Fe incorporation on the pressure-dependent elasticity of olivine. Our measurements are suitable to determine the sound wave velocities of hydrous Fo90 olivine at pressures corresponding to the base of the upper mantle, to be integrated in theoretical/experimental studies attempting to constrain the olivine abundance and water content at the 410-km discontinuity.

## 5.2 Materials and methods

Large (200–500 μm) and homogeneous single crystals of hydrous Fo90 olivine used in this study were previously synthesized and characterized by Withers et al. (2011, 2012, sample M475). Major element concentrations determined by wavelength-dispersive EPMA analysis indicate the Mg# of synthesized olivines to be 90.2(1), and water content was determined to

be ~0.20(3) wt.% based on elastic recoil detection analysis (ERDA) (Withers et al., 2012). Polarized FTIR spectroscopy and secondary ion mass spectroscopy (SIMS) measurements were also conducted on the same sample, showing excellent agreement with one another (Withers et al., 2012).

High-pressure Brillouin scattering measurements in DAC were conducted in the so-called platelet geometry (Whitfield et al., 1976). For olivine, at least two crystal platelets with different crystallographic orientations are required to obtain the nine independent elastic stiffness coefficients ($c_{ij}$) given its orthorhombic symmetry. The full elastic tensor is obtained by a least-square fit of experimentally determined densities and sound wave velocities measured in different crystallographic directions using the Christoffel's equation:

$$\left|c_{ijkl}q_j q_l - \rho v_i^2 \delta_{ik}\right| = 0 \qquad (5.1)$$

where $c_{ijkl}$ are the elastic stiffness coefficients in tensorial notation (e.g., Nye, 1985), $q_j$ and $q_l$ are direction cosines, $\rho$ is the density, $v_i$ are the sound wave velocities and $\delta_{ik}$ is the Kronecker delta. To obtain accurate and precise $c_{ij}$ values, it is important that their correlation in the fit procedure is low. This is achieved by using two appropriate crystallographic orientations (Criniti et al., 2021). We used published $c_{ij}$ data for Fo90 olivine (Abramson et al., 1997) to simulate the shear ($v_S$) and compressional velocities ($v_P$) for different crystallographic planes. Synthetic $v_S$ and $v_P$ were randomly scattered by up to ± 30 or ± 60 m/s, respectively, to simulate realistic datasets and to obtain realistic uncertainties in the inversion procedure. Platelets with direction cosines (0.32, 0.91, 0.26) and (0.78, 0.02, 0.62), corresponding to 101 and 161 *hkl* indices, were chosen for high-pressure measurements.

Hydrous Fo90 olivine single crystals were first observed under a polarising microscope and selected based on the absence of inclusions and their sharp optical extinction. Preliminary X-ray diffraction measurements were carried out on a Huber single-crystal diffractometer equipped with a point detector and Mo$K\alpha$ radiation, and driven by the software SINGLE (Angel and Finger, 2011). Sharp diffraction peaks (full width half maxima < 0.055°) were observed upon omega-scan rotations for each crystal, confirming their high quality. Two crystals were selected and subsequently oriented parallel to the (101) or (161) crystallographic planes, glued on glass slides and polished on both sides to obtain platelets (crystals X1 and X2, respectively) with a thickness of ~15 μm. The two platelets were then cut into semi-circular or rectangular shapes (Figure 5.1) using a FEI Scios focused ion beam (Schulze et al., 2017), operated at 30 nA and 30 kV.

High-pressure SCXRD and Brillouin scattering measurements were carried out in a BX-90 piston-cylinder-type diamond anvil cell (DAC) (Kantor et al., 2012) equipped with Almax-Boehler diamond anvils having culets of 500 μm in diameter and conical seats with large opening angles (Boehler and De Hantsetters, 2004). A Re gasket was indented to a thickness of ~70 μm and drilled with an infrared laser to obtain the sample chamber. The two FIB-cut crystal platelets were loaded into the same sample chamber together with a ruby sphere (Figure 5.1) for pressure determination following the calibration reported by Shen et al. (2020). Pre-compressed helium was loaded as quasi-hydrostatic pressure transmitting medium using the gas loading apparatus installed at the Bayerisches Geoinstitut, University of Bayreuth (Kurnosov et al., 2008).

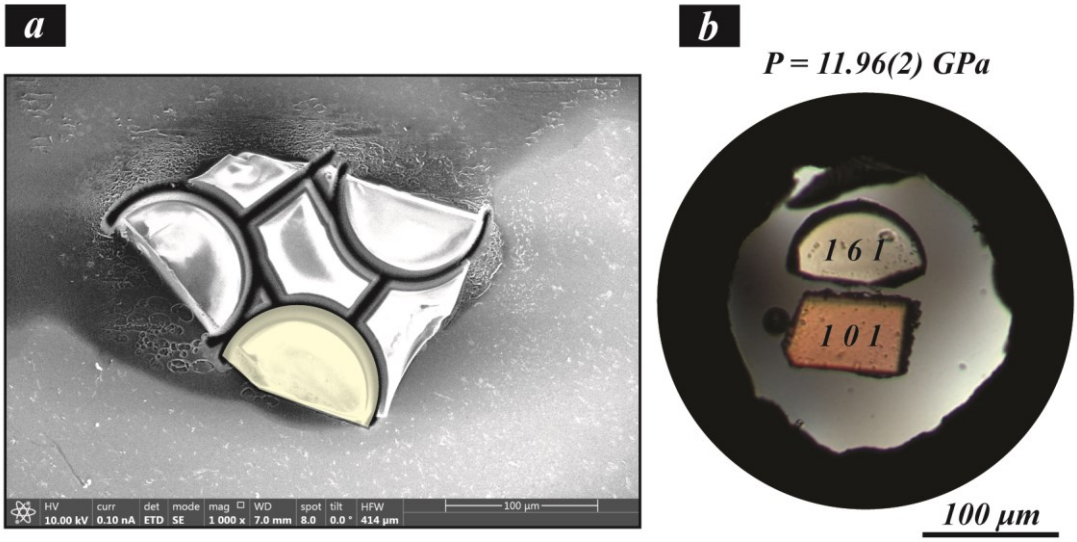


**Figure 5.1.** (a) Secondary electron image of a Fo90 olivine platelet oriented parallel to the (161) plane (crystal X2) after the FIB cutting procedure; a superimposed yellow semicircle denotes the sample that was then loaded in the DAC. (b) Cross-polarized light photomicrographs of platelet X2 (161) and X1 (101) inside the sample chamber of the DAC at high pressure, together with a ruby chip (dark black sphere on the left of 101 platelet).

High-pressure SCXRD and Brillouin scattering measurements were conducted using the system installed at the Bayerisches Geoinstitut, University of Bayreuth (Trots et al., 2011, 2013). The Brillouin scattering system consists of a Coherent Verdi V2 solid-state Nd:$YVO_4$ laser with a 532 nm single wavelength output and a six-pass Sandercock-type tandem Fabry-Perot interferometer (Sandercock, 1982) equipped with a Hamamatsu C11202-50 detector. A source laser power of 100 or 150 mW was used for room pressure and high-pressure measurements, respectively. All measurements were performed in platelet geometry with an external scattering angle of 79.5°, which was calibrated using a fused silica glass standard. Periodic measurements of the standard revealed deviations within ± 0.1°, which correspond

to shifts of up to ± 0.1% in the calculated velocities, well within our experimental uncertainty. Dispersion curves of sound wave velocities versus crystallographic orientation were collected by rotation of the χ circle of the diffractometer between –170° and 180° at steps of 10° or 20°. Densities were derived at each pressure from single-crystal diffraction measurements, which were performed on the same goniometer using a Huber Eulerian single-crystal X-ray diffractometer equipped with a point detector. The system is coupled with an ultra-high intensity rotating anode X-ray source (Mo$K\alpha$, FR-E$^+$ SuperBright from Rigaku) operated at 55 kV and 45 mA and multilayer VaryMax$^{TM}$ focusing optics, and was driven by the software SINGLE (Angel and Finger, 2011). At each pressure point, 14–18 Bragg reflections for each crystal were centred using the eight position centring method (King and Finger, 1979), and cell parameters were determined by vector least-square refinement (Ralph and Finger, 1982).

# 5.3 Results and discussion

## 5.3.1 Compressibility of hydrous Fo90 olivine

High-pressure SCXRD measurements were conducted at seven pressure points, ranging from ambient pressure to ~12 GPa. Unit-cell lattice parameters and volumes of both hydrous Fo90 olivine single crystals investigated in this study are reported in Table 5.1.

**Table 5.1.** Unit-cell lattice parameters and volumes of hydrous Fo90 olivine crystals X1 and X2 measured in the DAC experiment. Pressure is calculated using the ruby fluorescence calibration of Shen et al. (2020).

| | **X1 (platelet *1 0 1*)** | | | | **X2 (platelet *1 6 1*)** | | | |
|---|---|---|---|---|---|---|---|---|
| ***P* (GPa)** | **a (Å)** | **b (Å)** | **c (Å)** | **V (Å$^3$)** | **a (Å)** | **b (Å)** | **c (Å)** | **V (Å$^3$)** |
| 0.00010(1) | 4.7613(5) | 10.2243(2) | 5.9925(3) | 291.72(3) | 4.7610(1) | 10.2227(3) | 5.9921(1) | 291.63(1) |
| 1.40(2) | 4.7499(7) | 10.1753(3) | 5.9701(5) | 288.55(4) | 4.7487(3) | 10.1744(5) | 5.9700(3) | 288.44(2) |
| 3.23(2) | 4.7351(5) | 10.1147(3) | 5.9432(4) | 284.64(3) | 4.7342(2) | 10.1128(4) | 5.9423(2) | 284.49(2) |
| 5.53(4) | 4.7178(7) | 10.0455(3) | 5.9116(5) | 280.16(3) | 4.7176(2) | 10.0436(4) | 5.9108(2) | 280.06(2) |
| 7.66(2) | 4.7029(6) | 9.9847(3) | 5.8837(4) | 276.28(3) | 4.7028(3) | 9.9824(7) | 5.8826(3) | 276.16(3) |
| 9.60(4) | 4.6902(7) | 9.9313(3) | 5.8592(6) | 272.92(3) | 4.6899(3) | 9.9292(5) | 5.8581(2) | 272.80(2) |
| 11.96(2) | 4.6765(6) | 9.8731(2) | 5.8319(5) | 269.27(3) | 4.6762(2) | 9.8707(4) | 5.8309(1) | 269.14(1) |

The two crystals have slightly different volumes, $V$ (X1) > $V$ (X2), with crystal X1 showing larger uncertainties on the measured lattice parameters. This is due to its crystallographic orientation, which limits the observations in both **a*** and **c***. Therefore, lattice parameters

measured for crystal X2 are likely more accurate. The variation with pressure of the lattice parameters and volumes, normalized with respect to their room pressure values, are reported in Figure 5.2 and compared with literature data. Hydrous olivine is most compressible along the **b**-direction ([010]) and least compressible along the **a**-direction ([100]), as also observed for end-member Fo100 and Fo90 (e.g., Downs et al., 1996; Pamato et al., 2019). The EoSFit7c program was used to fit the *P–V* data of both crystals using a third-order Birch-Murnaghan Equation of State (BM3 EoS) (Angel et al., 2014):

$$P = \frac{3}{2}K_{T0}\left[\left(\frac{V_0}{V}\right)^{\frac{7}{3}} - \left(\frac{V_0}{V}\right)^{\frac{5}{3}}\right]\left\{1 + \frac{3}{4}(K'_{T0} - 4)\left[\left(\frac{V_0}{V}\right)^{\frac{2}{3}} - 1\right]\right\} \quad (5.2)$$

where $V_0$ is the ambient pressure unit-cell volume, $K_{T0}$ the isothermal bulk modulus and $K'_{T0}$ its pressure derivative. The resulting BM-EoS parameters, simultaneously refined using the data weighted by the uncertainties in *P* and *V*, are: $V_0$ = 291.65(2) Å$^3$, $K_{T0}$ = 124.5(1.0) GPa and $K'$= 4.5(2), where values in parenthesis correspond to 1σ uncertainties on each parameter. The fitted $V_0$ value is in excellent agreement (within 1σ) with the unit-cell volume measured at room pressure for crystal X2. To judge the correctness of truncation of the BM-EoS to third order and to assess whether higher order terms ($K''$) might be significant in the EoS, we plotted the Eulerian finite strain ($f_E$) versus the normalized stress ($F_E$) ($f_E$-$F_E$ plot; Angel, 2000) (Supplementary Figure S1). Assessment of the $f_E$-$F_E$ plot indicates that data are adequately described by a BM-EoS truncated to third order. Moreover, we have constructed confidence ellipses (Angel, 2000) in $K_{T0}$ and $K'_{T0}$ obtained for the fit to the hydrous olivine *P–V* dataset to visualise the extent of the correlation between such parameters and to assess the quality of the EoS (Supplementary Figure S1). Following the approach of Angel (2000) and Angel et al. (2014), linearized BM3 EoSs have been used to fit the variation with pressure of the **a**-, **b**- and **c**-axis by substituting *V* with $l^3$, $3K_{T0}$ with $M_{l,0}$ and $3K'_{T0}$ with $M'_{l,0}$:

$$P = \frac{1}{2}M_{l,0}\left[\left(\frac{l_0}{l}\right)^{7} - \left(\frac{l_0}{l}\right)^{5}\right]\left\{1 + \frac{1}{4}(M'_{l,0} - 12)\left[\left(\frac{l_0}{l}\right)^{2} - 1\right]\right\} \quad (5.3)$$

The resulting EoS parameters are: $a_0$ = 4.7610(1) Å, $M_{0a}$ = 539.1(5.7) GPa, $M'_a$= 23.7(1.4), $b_0$ = 10.2238(3) Å, $M_{0b}$ = 283.4(2.8) GPa, $M'_b$= 10.7(6) and $c_0$ = 5.9921(1) Å, $M_{0c}$ = 372.1(2.6) GPa, $M'_c$= 12.1(5). As described in Angel et al. (2014), the linear moduli and their

pressure derivatives defined in this fashion have numerical values three times those of the corresponding $K_{T0}$ and, therefore, must be divided by three in order to return volume-like values. The resulting axial compressibility for the hydrous olivine follows the scheme $\beta_b > \beta_c > \beta_a$ (as observed for the anhydrous phase) and the obtained $M_{l,0}$ and $M'_{l,0}$ values compare well with those of the anhydrous phase reported in the literature, as discussed later.

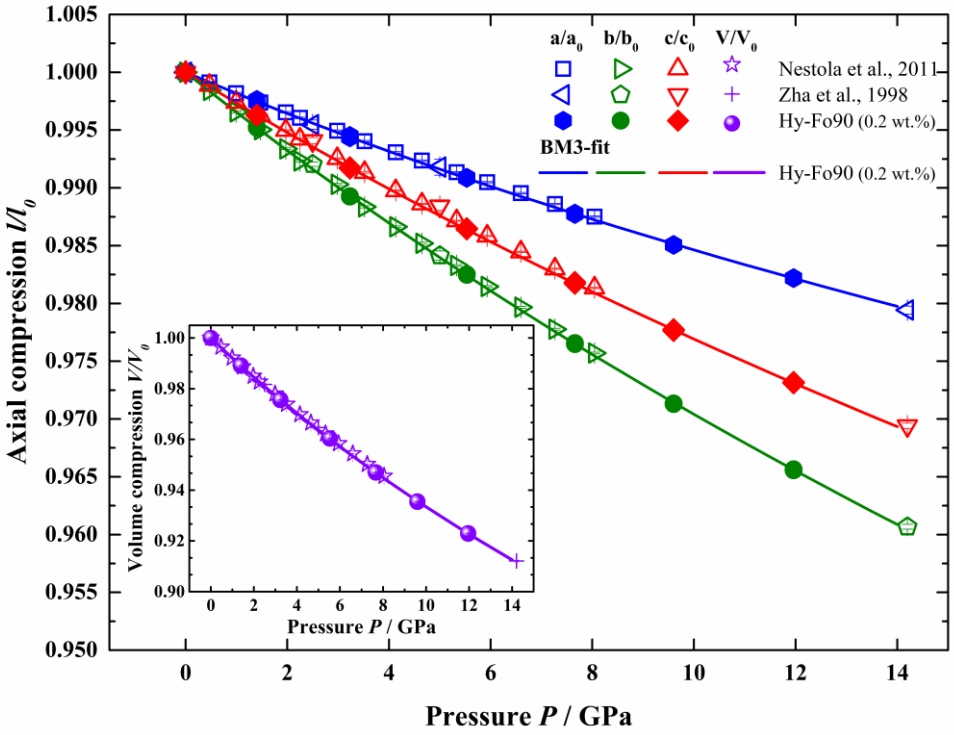


**Figure 5.2.** Unit-cell parameters and unit-cell volumes (inset) of crystals X1 and X2 normalized to their room pressure values; data were fitted with a third-order Birch-Murnaghan EoS using the EosFit7c program (Angel et al., 2014). Literature data of anhydrous Fo90-92 olivines (Nestola et al., 2011; Zha et al., 1998; Supplementary Table S1) are shown for reference. Note the good agreement between the BM3 fits and relative compression data of hydrous Fo90 olivine and the literature data for the corresponding anhydrous phase.

Angel et al. (2018) recently reviewed all the published single-crystal data that constrain the elastic properties and EoS of mantle-composition olivine (Fo90 to Fo92), also testing the mutual consistency of the different datasets used. Therefore, data selected by Angel et al. (2018) will be used as a comparison for hydrous olivine. The unit-cell lattice parameters reported by Nestola et al. (2011) and Zha et al. (1998), normalized to their corresponding room pressure values, are compared to the single crystal hydrous Fo90 olivine data obtained in this study (Figure 5.2). When compared to the *P–V* and linearized BM3 EoS fits of the hydrous Fo90 olivine data obtained in this study, the relative compression curves (lattice parameters and volume) for the corresponding anhydrous phase show good agreement.

Hence, we do not observe anomalies in the axial compressibility scheme or the unit-cell volume compression of the hydrous phase.

### 5.3.2 Sound wave velocities of hydrous Fo90 olivine and $c_{ij}$ inversion strategy

Sound wave velocities of hydrous Fo90 olivine were measured at seven pressure points, ranging from ambient pressure to ~12 GPa, i.e., the same conditions of SCXRD measurements (Table 5.2). Typical Brillouin spectra collected in the low- and high-pressure range (Figure 5.3a) show distinct and resolved compressional ($v_P$) and shear ($v_{S1}$ and $v_{S2}$) wave velocities peaks for most ranges of rotation angle ($\chi$) of the diffractometer (Figure 5.3b).

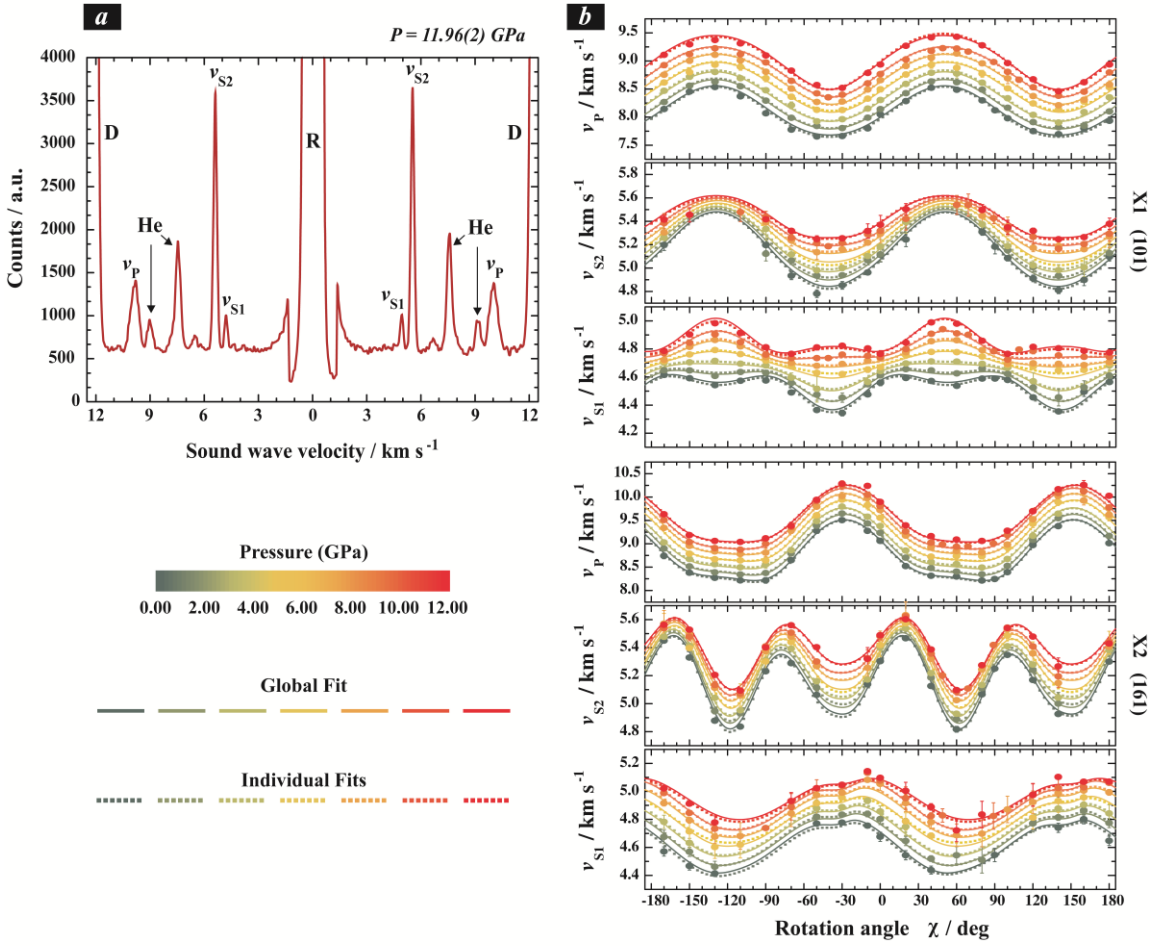


**Figure 5.3.** (a) Selected Brillouin spectrum of crystal X2 (161) at 11.96(2) GPa showing distinct and well-resolved compressional $v_P$, slow and fast shear $v_{S1}$ and $v_{S2}$ wave velocities peaks, as well as spectral contributions of the diamond anvils (D), pressure medium (He) and elastic scattering (R). (b) Data points (filled symbols) as a function of the rotation angle ($\chi$) for both platelets and dispersion curves obtained from the global fit (solid lines) and individual fits (dashed lines), showing excellent agreement between the two fitting strategies.

To obtain the nine elastic stiffness coefficients $c_{ij}$, the Christoffel's equation (Equation 5.1) is usually solved using a non-linear least-squares inversion of the density and all the acoustic velocities, collected with varying azimuthal angles, of the crystal platelets at each individual pressure point. This procedure has been referred to as individual fit in previous publications (Kurnosov et al., 2017; Criniti et al., 2021). Individual fits were performed at each pressure point by inverting all the measured acoustic velocities and density data, which were calculated self-consistently from the measured unit-cell volumes. Individual fits converged with small residuals at each pressure point (Figure 5.3b) thanks to compressional and shear wave velocities being observed for most ranges of rotation angle ($\chi$) and the low correlation between individual elastic stiffness coefficients resulting from the choice of the orientations of the two crystal platelets X1 and X2. Uncertainties in the determined $c_{ij}$ values are generally less than 1%, except for $c_{12}$ (< 2%) (Table 5.2).

Recently, a non-conventional fitting procedure for Brillouin data (referred to as global fit) was proposed by Kurnosov et al. (2017) and described in detail in Buchen (2018). It consists of a global inversion of all sound velocity and density data, instead of independently inverting the data measured at each individual pressure point. This is practically done by fitting all sound velocity and density data with third-order finite strain EoSs describing the evolution with compression of each $c_{ij}$, using the formalism of Stixrude and Lithgow-Bertelloni (2005):

$$c_{ijkl} = (1+2f_E)^{\frac{5}{2}}\{c_{ijkl,0} + \left(3K_0c'_{ijkl,0} - 5c_{ijkl,0}\right)f_E + \left(6K_0c'_{ijkl,0} - 14c_{ijkl,0} - \frac{3}{2}K_0\delta_{kl}^{ij}(3K'_0 - 16)\right)f_E^2\} \quad (5.4)$$

where $c_{ijkl}$ is the elastic stiffness coefficient in tensorial notation at a given density (i.e., pressure), $f_E$ is the finite Eulerian strain defined as $\frac{1}{2}\left[\left(\frac{\rho_0}{\rho}\right)^{\frac{2}{3}} - 1\right]$, $c_{ijkl,0}$ is the elastic stiffness coefficient at ambient conditions and $c'_{ijkl,0}$ its pressure derivative, $K_0$ is the bulk modulus at ambient conditions and $K'_0$ its pressure derivative, and $\delta^{ij}_{kl}$ is equal to −3 for $c_{1111}$, $c_{2222}$, and $c_{3333}$ and to −1 for the other six independent components of the elastic tensor. Thus, by refining the ambient-pressure stiffness coefficients ($c_{ij,0}$) and their pressure derivatives ($c'_{ij,0}$), a fit of all measured velocities at all pressure points is obtained. This approach has the advantage that all velocity data from all pressure points are used to constrain the $c_{ij}$s, minimizing the effect of data scattering on the calculated $c_{ij}$s and thus reducing their estimated uncertainties (Buchen, 2018).

**Table 5.2.** Elastic stiffness coefficients ($c_{ij}$) and elastic moduli obtained from the individual fit and global fit procedure, reported in GPa. Numbers in brackets represent one standard deviation (std). $\rho$ uncertainties propagates both the std of the unit-cell volumes from SCXRD and the chemical composition from EPMA.

**Individual Fits**

| $P$ (GPa) | $\rho$ (g cm$^{-3}$) | $c_{11}$ | $c_{22}$ | $c_{33}$ | $c_{44}$ | $c_{55}$ | $c_{66}$ | $c_{12}$ | $c_{13}$ | $c_{23}$ | $K_{SV}$ | $G_V$ | $K_{SR}$ | $G_R$ | $K_{SVHR}$ | $G_{VHR}$ |
|---|---|---|---|---|---|---|---|---|---|---|---|---|---|---|---|---|
| 0.00010(1) | 3.345(6) | 319.2(1.0) | 195.7(6) | 232.7(7) | 63.2(2) | 77.1(3) | 77.8(3) | 71.7(1.2) | 69.6(5) | 73.5(6) | 130.8(4) | 79.2(1) | 126.5(4) | 76.2(1) | 128.7(4) | 77.7(1) |
| 1.40(2) | 3.382(6) | 330.8(6) | 205.8(4) | 242.5(5) | 66.3(2) | 80.3(2) | 81.8(3) | 75.9(1.1) | 75.2(6) | 80.1(4) | 137.9(4) | 82.2(1) | 133.8(4) | 79.3(1) | 135.9(4) | 80.7(1) |
| 3.23(2) | 3.428(6) | 342.8(6) | 215.6(4) | 254.0(5) | 69.8(3) | 82.7(2) | 85.3(3) | 83.4(9) | 83.4(4) | 87.1(4) | 146.7(3) | 84.8(1) | 142.4(3) | 82.0(1) | 144.5(3) | 83.4(1) |
| 5.53(4) | 3.483(6) | 359.2(1.1) | 229.1(4) | 264.1(6) | 74.5(2) | 85.9(5) | 87.9(5) | 94.1(1.8) | 91.1(7) | 94.8(6) | 156.9(5) | 87.8(2) | 152.5(5) | 85.2(1) | 154.7(5) | 86.5(1) |
| 7.66(2) | 3.532(6) | 374.3(1.1) | 238.6(4) | 276.2(8) | 77.4(2) | 88.7(2) | 93.3(3) | 101.9(1.4) | 98.7(7) | 102.3(6) | 166.1(4) | 91.0(1) | 161.3(4) | 88.2(1) | 163.7(4) | 89.6(1) |
| 9.60(4) | 3.575(6) | 388.1(1.2) | 249.8(6) | 286.2(9) | 80.2(2) | 91.0(3) | 96.7(3) | 109.7(1.8) | 106.0(7) | 108.8(8) | 174.8(5) | 93.5(1) | 169.8(5) | 90.9(1) | 172.3(4) | 92.2(1) |
| 11.96(2) | 3.624(6) | 404.0(1.3) | 260.7(8) | 296.5(9) | 83.6(3) | 94.0(3) | 99.8(4) | 115.6(1.6) | 116.1(7) | 118.2(8) | 184.6(5) | 96.2(1) | 179.4(5) | 93.5(1) | 182.0(5) | 94.8(1) |
| **Global Fit** | | | | | | | | | | | | | | | | |
| 0.00010(1) | 3.345(6) | 319.2(7) | 197.4(4) | 233.9(5) | 63.8(2) | 77.6(2) | 78.5(3) | 72.4(1.0) | 69.9(4) | 74.3(4) | 131.5(3) | 79.6(1) | 127.4(3) | 76.6(1) | 129.5(3) | 78.1(1) |
| 1.424(7) | 3.382(6) | 329.9(7) | 205.4(4) | 241.9(5) | 66.3(2) | 79.8(2) | 81.2(3) | 77.7(1.0) | 75.3(4) | 79.6(4) | 138.1(3) | 81.8(1) | 133.8(3) | 78.9(1) | 135.9(3) | 80.3(1) |
| 3.26(2) | 3.428(6) | 343.2(8) | 215.5(5) | 252.0(6) | 69.6(2) | 82.4(2) | 84.7(3) | 84.5(1.0) | 82.3(5) | 86.3(5) | 146.3(3) | 84.5(1) | 142.0(3) | 81.7(1) | 144.2(3) | 83.1(1) |
| 5.56(3) | 3.483(6) | 359.6(9) | 227.9(5) | 264.3(7) | 73.5(2) | 85.6(2) | 88.9(3) | 93.0(1.2) | 91.1(5) | 94.7(6) | 156.6(4) | 87.8(1) | 152.1(4) | 85.1(1) | 154.3(4) | 86.4(1) |
| 7.72(4) | 3.532(6) | 374.5(1.1) | 239.3(6) | 275.6(8) | 77.1(3) | 88.6(3) | 92.8(4) | 101.0(1.4) | 99.2(6) | 102.5(6) | 166.1(4) | 90.8(1) | 161.4(4) | 88.1(1) | 163.7(4) | 89.5(1) |
| 9.69(5) | 3.575(6) | 387.9(1.2) | 249.6(7) | 285.6(9) | 80.4(3) | 91.1(3) | 96.3(4) | 108.2(1.6) | 106.7(7) | 109.6(7) | 174.7(5) | 93.5(1) | 169.8(5) | 90.8(1) | 172.2(5) | 92.1(1) |
| 12.04(7) | 3.624(6) | 403.4(1.4) | 261.5(9) | 297.3(1.0) | 84.2(4) | 94.1(4) | 100.3(5) | 116.7(1.8) | 115.5(8) | 118.0(9) | 184.7(6) | 96.5(2) | 179.7(5) | 93.8(1) | 182.2(5) | 95.2(1) |

Even though this fitting procedure is particularly suited for very high pressure data, where some of the $c_{ij}$s are poorly constrained due to the lack of observations (e.g., Criniti et al., 2021), it can be applied to any high-pressure sound velocity dataset and the two procedures should yield consistent results as long as the collected data are of high quality, the high-pressure evolution of all $c_{ij}$ is well described by a third-order finite strain EoS, and no phase transition takes place in the investigated pressure interval. Therefore, we also applied the global fit procedure to our dataset, which yielded very consistent results compared to those obtained by individual fits. The $c_{ij}$s calculated from two procedures show virtually no discrepancies, with values typically identical within two standard deviations (Table 5.2, Figure 5.4).

Because density is measured at each pressure point, it is possible to calculate pressure without relying on a secondary scale (e.g., ruby) using the relative change in volume of the sample, obtained by X-ray diffraction, and the 3$^{rd}$-order finite strain equations described above. From these, an expression for the isothermal bulk modulus in the Reuss bound ($K_{TR}$) as a function of volume is obtained and the absolute pressure ($P_{abs}$) can be calculated by integrating $K_{TR}/V$ over a given volume interval:

$$P_{abs} = \int_{V_0}^{V} \frac{K_{TR}(V)}{V} dV = 3K_{TR0} f_E (1 + 2f_E)^{\frac{5}{2}} \left[1 + \frac{3}{2}(K'_{TR0} - 4) f_E\right] \qquad (5.5)$$

where $K_{TR,0}$ is the bulk modulus at ambient conditions, $K'_{TR,0}$ is its pressure derivative, $f_E$ is the finite Eulerian strain defined as $\frac{1}{2}\left[\left(\frac{V_0}{V}\right)^{\frac{2}{3}} - 1\right]$. The experimentally determined adiabatic bulk modulus $K_{SR}$ (Table 5.2) was converted into $K_{TR}$ using the relations $K_{SR} = K_{TR}(1 + \alpha\gamma T)$ and $\alpha = \gamma C_V / K_{TR} V$. The thermoelastic parameters used for the conversion are $\theta_D$ = 644 K, $\gamma_0$ = 1.044 and $q$ = 1.88, corresponding to Fo90 (Angel et al., 2018), and are here assumed to be $H_2O$-independent. Then, $K_{TR0}$ and $K'_{TR0}$ were calculated by fitting a BM3 EoS to our $K_T$–$V$ dataset. A comparison between the absolute pressure and the pressures determined from the ruby fluorescence shift is plotted in Supplementary Figure S2, along with the BM3 EoS fits to the $K_{SR}$–$\rho$ datasets obtained from the global and individual fits, which show excellent agreement.

Figure 5.4 shows individual $c_{ij}$ as a function of absolute pressure, as well as selected literature data for anhydrous Fo90 olivines for comparison, following the re-analysis of all the published single crystal data proposed by Angel et al. (2018) (Supplementary Table S2). The longitudinal coefficients ($c_{11}$, $c_{22}$ and $c_{33}$), the off-diagonal coefficients ($c_{12}$, $c_{13}$ and $c_{33}$)

and the shear coefficients $c_{44}$ and $c_{66}$ follow a nearly linear increase with pressure, whereas the shear coefficient $c_{55}$ exhibits a slightly downward trend towards higher pressures. The longitudinal coefficients $c_{11}$, $c_{22}$, $c_{33}$ and the shear coefficients $c_{44}$, $c_{55}$, $c_{66}$ follow similar trends with pressure compared to the anhydrous phase; only $c_{66}$ is slightly offset to lower values in the range of 5 to 10 GPa (Figure 5.4e).

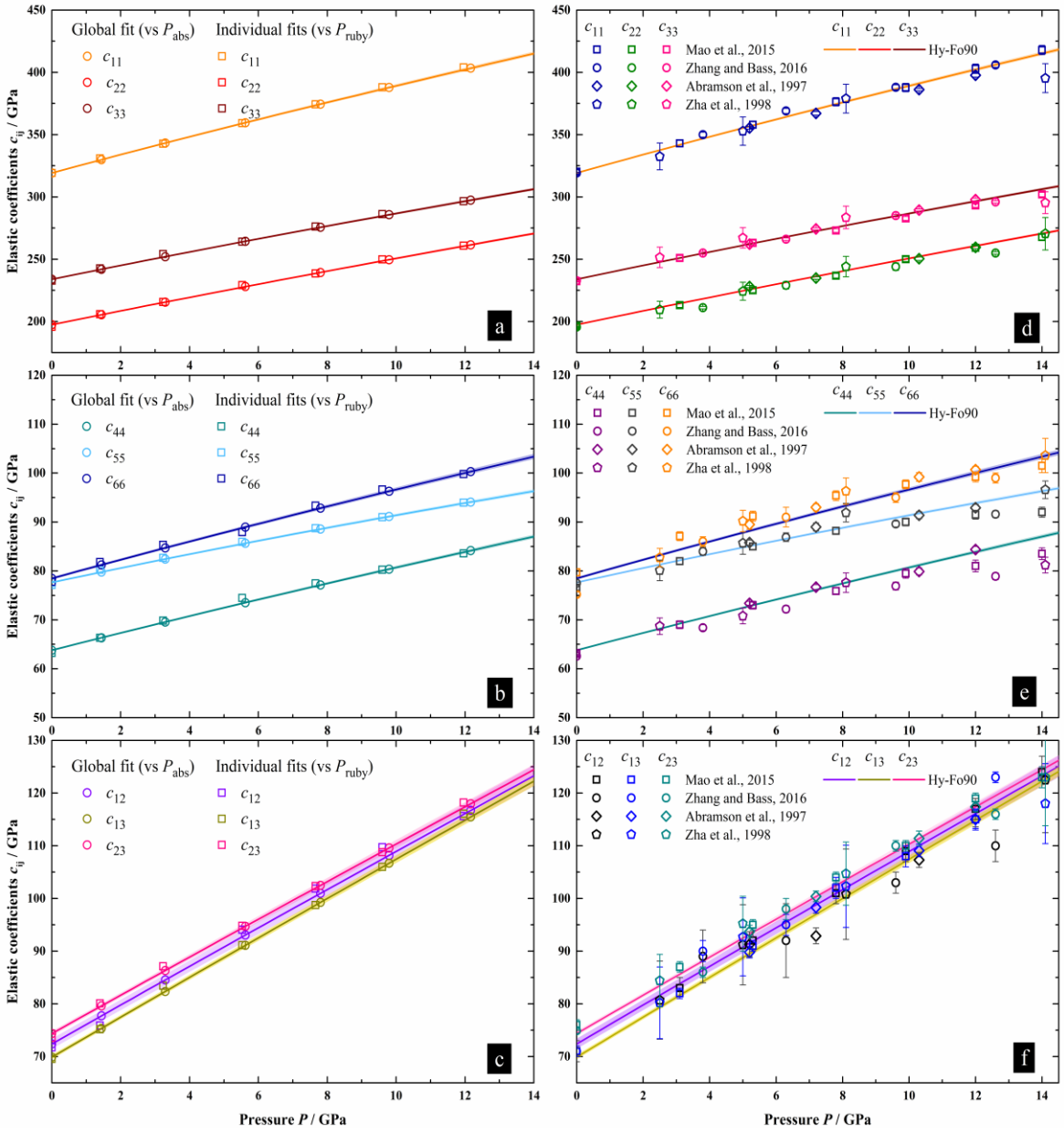


**Figure 5.4.** (a-b-c) Comparison of the $c_{ij}$ obtained through the global fit (open circles) and individual fits (open squares), showing values typically identical within two standard deviations (Table 5.2); the solid lines represent 3rd order EoS fits of each $c_{ij}$ (global fit parameters) (Table 5.3). (d-e-f) Comparison of the $c_{ij}$ of anhydrous Fo90 olivines selected from previous literature (Abramson et al., 1997; Mao et al., 2015; Zha et al., 1998; Zhang and Bass, 2016), and the fit curves for each $c_{ij}$ (global fit parameters) of hydrous Fo90 olivine obtained in this study. Note that the fits of the experimentally determined $c_{ij}$s for hydrous olivine and the $c_{ij}$s of the corresponding anhydrous phase are nearly identical.

The off-diagonal coefficients $c_{12}$, $c_{13}$, $c_{23}$ are characterized by very similar values along the whole pressure interval, with the stiffness scheme being $c_{23} > c_{12} > c_{13}$. Due to the small differences in the magnitude of the off-diagonal coefficients, their values are frequently the same within uncertainties, especially at high pressure. The off-diagonal coefficients $c_{12}$, $c_{13}$, $c_{23}$ of the anhydrous phase are scattered but show comparable trends with those of the hydrous phase, especially $c_{23}$. Even if $c_{13}$ is generally stiffer than $c_{12}$, in contrast with the hydrous phase, their systematics is more complex, as either they frequently cross over or are the same within uncertainties. Third-order finite strain EoSs (Equation 5.4) were also used to fit the selected $c_{ij}$ for anhydrous Fo90 olivines (Supplementary Table S2); the determined $c_{ij,0}$ and $c'_{ij,0}$ are reported in Table 5.3. The longitudinal, shear and off-diagonal moduli of hydrous and anhydrous Fo90 olivines are identical within two standard deviations, and the same holds true for their pressure derivatives, except for $c'_{11,0}$ of hydrous Fo90 which is slightly larger. The fit curves of the $c_{ij}$s for hydrous and anhydrous olivine (Supplementary Figure S3) are in good agreement with each other, except for $c_{11}$, $c_{22}$, $c_{44}$, and $c_{55}$ of hydrous Fo90 which become moderately stiffer than their anhydrous corresponding at high pressure; this suggests a relatively small effect of water on the elastic properties of Fo90 olivine.

**Table 5.3.** Resulting fit parameters of the third-order finite strain expression for the $c_{ij,0}$ and $c'_{ij,0}$ (as shown in Figure 5.4) and anhydrous Fo90 (Supplementary Figure S3).

| | ***Hydrous Fo90 olivine*** | | ***Anhydrous Fo90 olivine*** | |
|---|---|---|---|---|
| | $c_{ij,0}$ | $c'_{ij,0}$ | $c_{ij,0}$ | $c'_{ij,0}$ |
| $c_{11}$ | 319.2(7) | 7.18(9) | 320.0(9) | 6.65(12) |
| $c_{22}$ | 197.4(4) | 5.41(5) | 195.9(9) | 5.17(11) |
| $c_{33}$ | 233.9(5) | 5.43(7) | 233.2(6) | 5.35(8) |
| $c_{44}$ | 63.8(2) | 1.72(2) | 63.2(4) | 1.61(5) |
| $c_{55}$ | 77.6(2) | 1.45(2) | 77.7(3) | 1.34(5) |
| $c_{66}$ | 78.5(3) | 1.87(3) | 78.0(6) | 1.93(7) |
| $c_{12}$ | 72.4(1.0) | 3.57(12) | 71.3(1.1) | 3.40(14) |
| $c_{13}$ | 69.9(4) | 3.67(5) | 71.0(7) | 3.74(10) |
| $c_{23}$ | 74.3(4) | 3.52(6) | 75.4(7) | 3.39(9) |

## 5.3.3 Elastic properties of hydrous Fo90 *vs* anhydrous Fo90 olivine

The adiabatic $K_S$ and $G$ were calculated from the $c_{ij}$ values in the Reuss and Voigt bounds and in the Voigt-Reuss-Hill average at each experimental pressure point and are reported in Table 5.2. The elastic moduli obtained in this study were then fitted with third-order finite strain EoS to obtain the elastic moduli at ambient conditions ($K_{S0}$ and $G_0$) and their pressure derivatives ($K'_{S0}$ and $G'_0$) using the finite strain EoS of Stixrude and Lithgow-Bertelloni (2005):

$$K = (1+2f_E)^{\frac{5}{2}}\left[K_0 + (3K_0K_0' - 5K_0)f_E + \frac{27}{2}(K_0K_0' - 4K_0)f_E^2\right] \quad (5.6)$$

$$G = (1+2f_E)^{\frac{5}{2}}\left[G_0 + (3K_0G_0' - 5G_0)f_E + \left(6K_0G_0' - 24K_0 - 14G_0 + \frac{9}{2}K_0K_0'\right)f_E^2\right] \quad (5.7)$$

The EoS parameters for $K$ and $G$ in the Voigt and Reuss bound are reported in Table 5.4. Both $K_S$ and $G$ show a monotonic increase with pressure (Figure 5.5a) and are perfectly described by third-order EoS.

To quantify the effect of 0.20 wt.% $H_2O$ on the Fo90 elastic properties, the EoS parameters for hydrous Fo90 olivine determined in this study have to be compared to those of the corresponding anhydrous phase. The elastic behaviour of anhydrous Fo90 olivine has been largely investigated in the past decades and its full elastic tensor has been constrained by a variety of techniques. Angel et al. (2018) presented a re-analysis of all available single crystal data for mantle-composition olivine (Fo90-92) providing best-fit EoS parameters, which were recently used to calculate olivine density profiles over the upper mantle under different thermal regimes (Faccincani et al., 2021). However, a comparison of the EoS parameters determined in this study with those from Angel et al. (2018) cannot be made for two main reasons: (i) a best fit of the shear modulus data is missing, (ii) the fit includes high-temperature volume data and high-pressure, high-temperature (*HP–HT*) elasticity data, which are not available for hydrous Fo90 olivine. For this reason, we refitted the high-pressure elasticity data ($K_S$ and $G$) for anhydrous Fo90 originally used in the fit from Angel et al. (2018) with the same formalism used for hydrous Fo90 olivine (Equations 5.6 and 5.7). The utilised data correspond to Fo90 olivines, and were selected up to ~14 GPa, i.e., the uppermost limit of olivine stability field. In our examination, we also made a re-analysis of the available shear modulus data to provide the best fit for $G_0$ and $G'_0$ of anhydrous Fo90 olivine. $K_S$ and $G$ were recalculated from the $c_{ij}$ values reported at high pressure by Abramson et al. (1997) where the data are complete (i.e., four pressure points), the data of Zha et al. (1998) (i.e., four pressure points), the data of Mao et al. (2015) (i.e., seven pressure points) and the data of Zhang and Bass (2016) (i.e., five pressure points) (Figure 5.5b, Supplementary Table S2). The EoS parameters for $K_S$ and $G$ in the Voigt and Reuss bound are reported in Table 5.4.

The EoS parameters for hydrous and anhydrous Fo90 olivine at ambient conditions are consistent within errors, especially $K$ and $G$ (Table 5.4). A comparison of the two obtained sets of EoS parameters indicates that the incorporation of 0.20 wt.% $H_2O$ into the olivine

crystal structure causes only a minor reduction in $K_{S0}$ and $G_0$ of ~0.2% and ~0.7%, respectively, and an increase in $K'_{S0}$ and $G'_0$ of ~2.5% and ~5%, respectively. This suggests a negligible effect of water incorporation on $K$ and $G$ of Fo90 olivine and a moderate, positive effect on $K'$ and $G'$. For this reason, the elastic behaviour of hydrous and anhydrous Fo90 olivine is indistinguishable within uncertainties up to ~14 GPa.

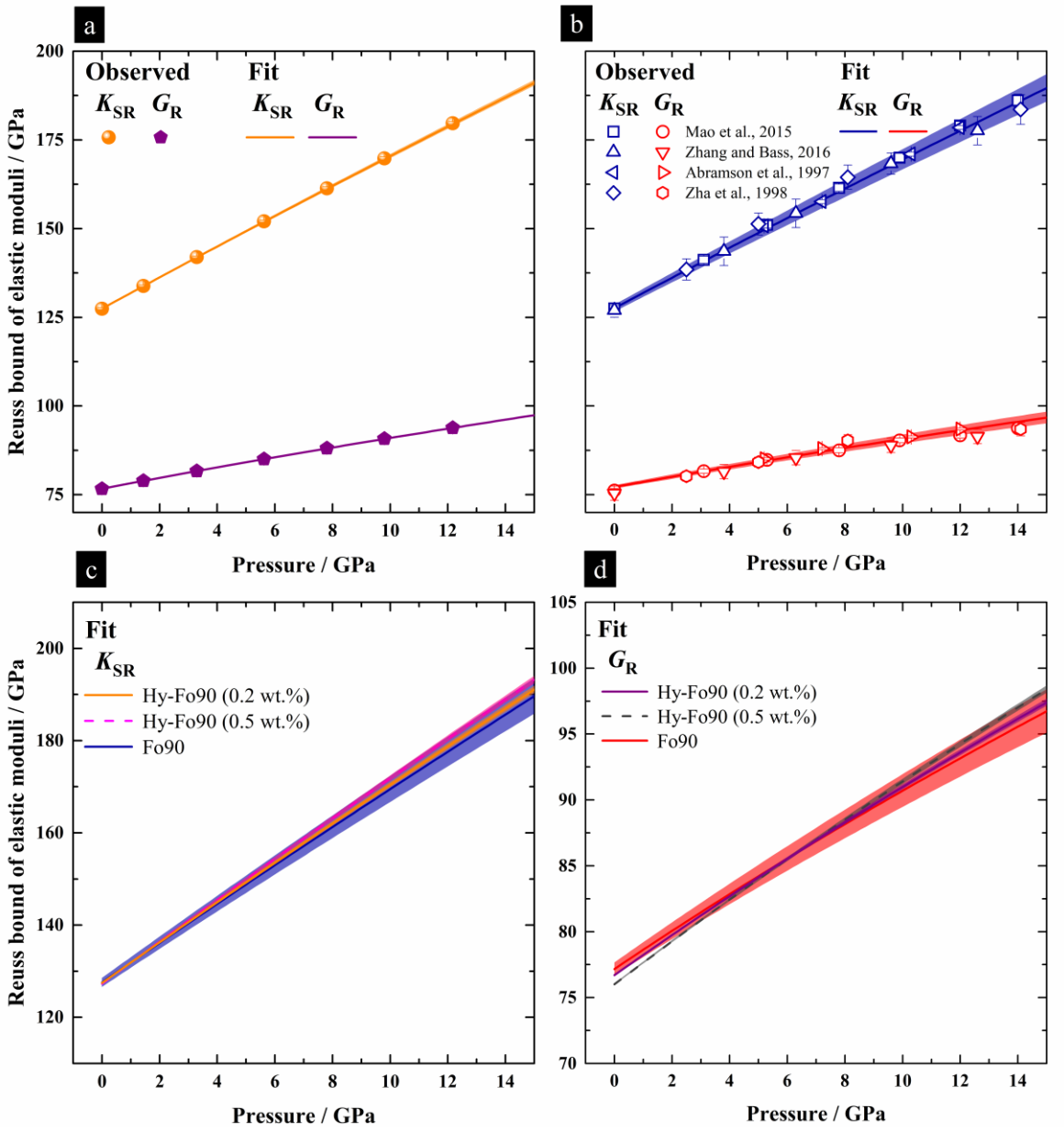


**Figure 5.5.** (a) Variation as a function of pressure of the bulk ($K$) and shear ($G$) moduli of hydrous Fo90 calculated in the Reuss bound from the experimental high-pressure elasticity measurements of this study; the solid line and shaded area are the fit of the experimental data and the associated uncertainty, respectively. (b) Variation as a function of pressure of the bulk ($K$) and shear ($G$) moduli of anhydrous Fo90 calculated in the Reuss bound from previous experimental high-pressure elasticity measurements (Abramson et al., 1997; Mao et al., 2015; Zha et al., 1998; Zhang and Bass, 2016); the solid line and shaded area are the fit of the experimental data and the associated uncertainty, respectively. (c-d) Superimposition of fit curves for hydrous Fo90 and anhydrous Fo90 olivine; the dashed lines represent a linear extrapolation of the effect of incorporation of 0.5 wt. % $H_2O$ on the

(*Continued*) elastic properties of Fo90 olivine (see text and Table 5.4). Uncertainties are calculated by propagating the experimental errors on density and elastic moduli.

This is consistent with a recent high-pressure single-crystal X-ray diffraction study conducted on a sample of Fo95 olivine with a low water content (~0.15 wt.% $H_2O$) (Xu et al., 2020), where hydrogen substitution is predominantly associated with the T site. As the effect of water on the elastic moduli and their derivatives in our Fo90 and Fo100 (Mao et al., 2010) may also depend on different H substitution mechanisms in olivine, besides distinct water contents, comparisons among different data should be made carefully. The Fo100 single crystals studied by Mao et al. (2010) were synthesized by Smyth et al. (2006), run SZ0408A, to which the reader is referred for synthesis conditions and FTIR spectrum. For this sample, it was suggested that hydration predominantly occurred through the octahedral substitution $Mg^{2+} \leftrightarrow 2H^{+}$. On the other hand, a tetrahedral substitution $Si^{4+} \leftrightarrow 4H^{+}$ has been suggested for our sample (Withers et al., 2011). Note, however, that the FTIR spectra of hydrous Fo100 (Smyth et al., 2006, Figure 2) and hydrous Fo90 (Withers et al., 2011, Figure 2) both show strong absorbance features in the identical high wavenumber region, hinting that the two samples should present the same substitution mechanism. Various pieces of evidence suggest that absorption features in the high wavenumber region (~3.450–3.600 $cm^{-1}$) are related to OH bonding to T sites (Fei and Katsura, 2020; Umemoto et al., 2011; Xue et al., 2017), therefore we may expect that both the Fo100 and Fo90 sample contain predominantly Si vacancies. The important observation, however, for the aim of this study is that both samples present the same type of defects and therefore we can compare the effect of hydration on their elastic properties directly, upon normalization with respect to $H_2O$ concentration. The effect of water on the elastic parameters can be expressed as:

$$\Delta_{H_2O} M \left( \frac{[M]}{wt.\%\ H_2O} \right) = \frac{M_{hydrous} - M_{dry}}{X_{H_2O}(wt.\%)} \tag{5.8}$$

where $M$ can be $K_{S0}$, $G_0$ (in GPa), $K'_{S0}$ or $G'_0$ (non-dimensional) and $X_{H2O}$ is the water content of the hydrous sample in wt.%. $\Delta_{H2O}$M values defined in this fashion yield the change in elastic properties for a reference water content of 1 wt.%; the obtained results for both Fo90 and Fo100 are reported in Table 5.4. $\Delta_{H2O}$M values are affected by large uncertainties, especially in the case of Fo90. This mostly arises from the fitting parameters of anhydrous Fo90, which are less well-constrained because four different datasets were combined in the EoS fit of the elastic moduli (Table 5.4). $\Delta_{H2O}K_{S0}$ and $\Delta_{H2O}G_{S0}$ for Fo90 and Fo100 are on the margins of being mutually consistent. Contrary to the prediction by Jacobsen et al. (2008,

2009), $K_{S0}$ of Fo100 is slightly more reduced by $H_2O$ compared to Fo90 and the two $G_0$'s show similar reductions. However, $\Delta_{H2O}K'_{S0}$ and $\Delta_{H2O}G'_{S0}$ values are in excellent agreement within mutual uncertainties (Table 5.4). Therefore, the more pronounced effect observed by Mao et al. (2010) on hydrous Fo100 elastic properties arises by virtue of the higher water content, and not from a different effect of water in Fe-free and Fe-bearing samples as shown in Table 5.4. This also suggests that hydration is most likely to have a linear effect on the pressure derivatives of olivines.

**Table 5.4.** EoS parameters for $K$ and $G$ in the Voigt and Reuss bound for hydrous and anhydrous Fo90 olivine and $\Delta_{H2O}M$ ($[M]$/wt.% $H_2O$) values calculated for hydrous Fo90 olivine and hydrous Fo100 forsterite.

***Anhydrous Fo90 olivine – best fit***

| | $K_{SV}$ | | $G_V$ | | $K_{SR}$ | | $G_R$ | |
|---|---|---|---|---|---|---|---|---|
| $M_0$ **(GPa)** | 131.8(1.0) | | 80.2(5) | | 127.5(1.0) | | 77.2(5) | |
| $M'_0$ | 4.29(14) | | 1.42(5) | | 4.33(14) | | 1.48(6) | |

***This study – Hydrous Fo90 olivine (global fit parameters)***

| | $K_{SV}$ | *% change* | $G_V$ | *% change* | $K_{SR}$ | *% change* | $G_R$ | *% change* |
|---|---|---|---|---|---|---|---|---|
| $M_0$ **(GPa)** | 131.5(2) | –0.2 | 79.57(6) | –0.7 | 127.4(2) | –0.1 | 76.70(6) | –0.6 |
| $M'_0$ | 4.40(3) | 2.5 | 1.49(1) | 5.2 | 4.44(3) | 2.6 | 1.55(1) | 4.9 |

$\Delta_{H_2O}M^{\backsim}$***%/wt.% $H_2O$ – Hydrous Fo90 olivine***

| | $K_{SV}$ | $G_V$ | $K_{SR}$ | $G_R$ |
|---|---|---|---|---|
| $M_0$ **(GPa)** | –1.5(5.1) | –3.2(2.6) | –0.5(5.1) | –2.5(2.5) |
| $M'_0$ | 0.55(72) | 0.35(26) | 0.55(72) | 0.35(31) |

$\Delta_{H_2O}M^{\backsim}[M]$***/wt.% $H_2O$*** [1] ***– Hydrous Fo100 forsterite [data from Mao et al., 2010 and Zha et al., 1996]***

| | $K_{SV}$ | $G_V$ | $K_{SR}$ | $G_R$ |
|---|---|---|---|---|
| $M_0$ **(GPa)** | –4.0(8) | –2.7(4) | –2.8(7) | –2.6(4) |
| $M'_0$ [1] | 0.33(23) | 0.39(13) | 0.33(23) | 0.39(13) |

***Hydrous Fo90 olivine – extrapolation to 0.5 wt.% $H_2O$***

| | $K_{SV}$ | *% change* | $G_V$ | *% change* | $K_{SR}$ | *% change* | $G_R$ | *% change* |
|---|---|---|---|---|---|---|---|---|
| $M_0$ **(GPa)** | 131.1(2) | –0.5 | 78.60(6) | –2.0 | 127.3(2) | –0.2 | 76.00(6) | –1.5 |
| $M'_0$ | 4.56(3) | 6.4 | 1.60(1) | 13.0 | 4.61(3) | 6.4 | 1.66(1) | 12.4 |

[1] $\Delta_{H2O}$M values yield the change in $K$, $G$, $K'$, and $G'$ for a reference water content of 1 wt.%.

[2] We assumed that $M'_0$ in the Voigt-Reuss-Hill bound ≈ $M'_0$ in the Voigt and Reuss bounds.

### 5.3.4 Effect of hydration on sound wave velocities of Fo90 olivine and its geophysical implications

Using the new experimental data obtained in this study, we calculated the aggregate sound wave velocities of hydrous Fo90 olivine with 0.20 wt.% $H_2O$ as a function of pressure. Aggregate sound wave velocities of anhydrous Fo90 olivine are compared with those for hydrous olivine (Figure 5.6). As the effect of temperature on the elasticity of hydrous olivine is currently unknown, all the calculations were performed at 300 K. In this context, Ye et al. (2009) showed that the thermal expansion coefficient of hydrous (0.89 wt.% $H_2O$) end-member forsterite (Fo100) is marginally larger, ~4.5(2.6) %, than that of Fo100. If this applies also for Fo90, the lower water content of our hydrous olivine (0.20 wt.% $H_2O$) would have a negligible effect on its thermal expansion. Moreover, the effect of water on the thermal expansion of hydrous (~2.5 wt.% $H_2O$) wadsleyite and ringwoodite, i.e., the high-pressure polymorphs of olivine, seems to be negligible (Inoue et al. 2004). Therefore, we propose that $H_2O$ is unlikely to have a significant effect on the thermal expansion of olivine. The $v_P$ and $v_S$ of hydrous Fo90 follow similar trends to those of the elastic moduli (Figure 5.6), with velocities being consistent with those of anhydrous Fo90 up to ~14 GPa. Mao et al. (2010) showed that $v_P$ and $v_S$ of the hydrous Fo100 cross and exceed those of the corresponding anhydrous phase at about 4 and 3 GPa, respectively, and rapidly diverge at higher pressure. The prominent rise of $v_P$ and $v_S$ with increasing pressure is due to the higher water content of the hydrous Fo100 sample employed by Mao et al. (2010) and not to a different effect of water in Fe-free and Fe-bearing samples, as shown in Table 5.4.

The 410-km global seismic discontinuity is widely accepted to be caused by the phase transition of olivine to its high pressure polymorph wadsleyite (Frost, 2008). Several works attempted to constrain the bulk olivine content in the upper mantle by comparing sound wave velocities of olivine and wadsleyite, calculated from either experimental or computational mineral physics data, with the observed seismic velocity contrasts across the discontinuity (e.g., Bass and Anderson, 1984; Dziewonski and Anderson, 1981; Núñez-Valdez et al., 2013; Wang et al., 2014, 2019). However, the calculated velocity contrasts across the discontinuity for a pyrolite composition (~60 vol.% olivine) are not consistent with global 1-D seismic models (e.g., Preliminary Earth Reference Model, PREM, or AK135; Dziewonski and Anderson, 1981; Kennett et al., 1995), pointing towards a bottom upper mantle that is less olivine-rich than pyrolite. Considering the reduction of the sound wave velocities of wadsleyite due to the incorporation of water (Mao et al., 2008a, 2008b), it was proposed that water dissolved in olivine and wadsleyite may reconcile the pyrolite model with seismological observations. Water is preferentially partitioned in wadsleyite ($D_{wad/ol}$ =

6; Thio et al., 2016) and whether the presence of water can resolve seismological observations with pyrolitic mantle olivine contents will depend on both the expected amount of water in olivine and to what extents it affects $v_P$ and $v_S$ of olivine. Available experimental data for hydrous olivine indicate storage capacities up to 0.9 wt.% (Smyth et al., 2006), but the water content of olivine under relevant deep upper mantle conditions will be much lower, around 0.2–0.5 wt.% $H_2O$ (e.g., Férot and Bolfan-Casanova, 2012; Hirschmann et al., 2005; Mosenfelder et al., 2006). In this regard, our data are particularly significant and indicate that the incorporation of ~0.20 wt.% $H_2O$ into Fo90 olivine crystal structure does not significantly affect its $v_P$ and $v_S$ at high pressure.

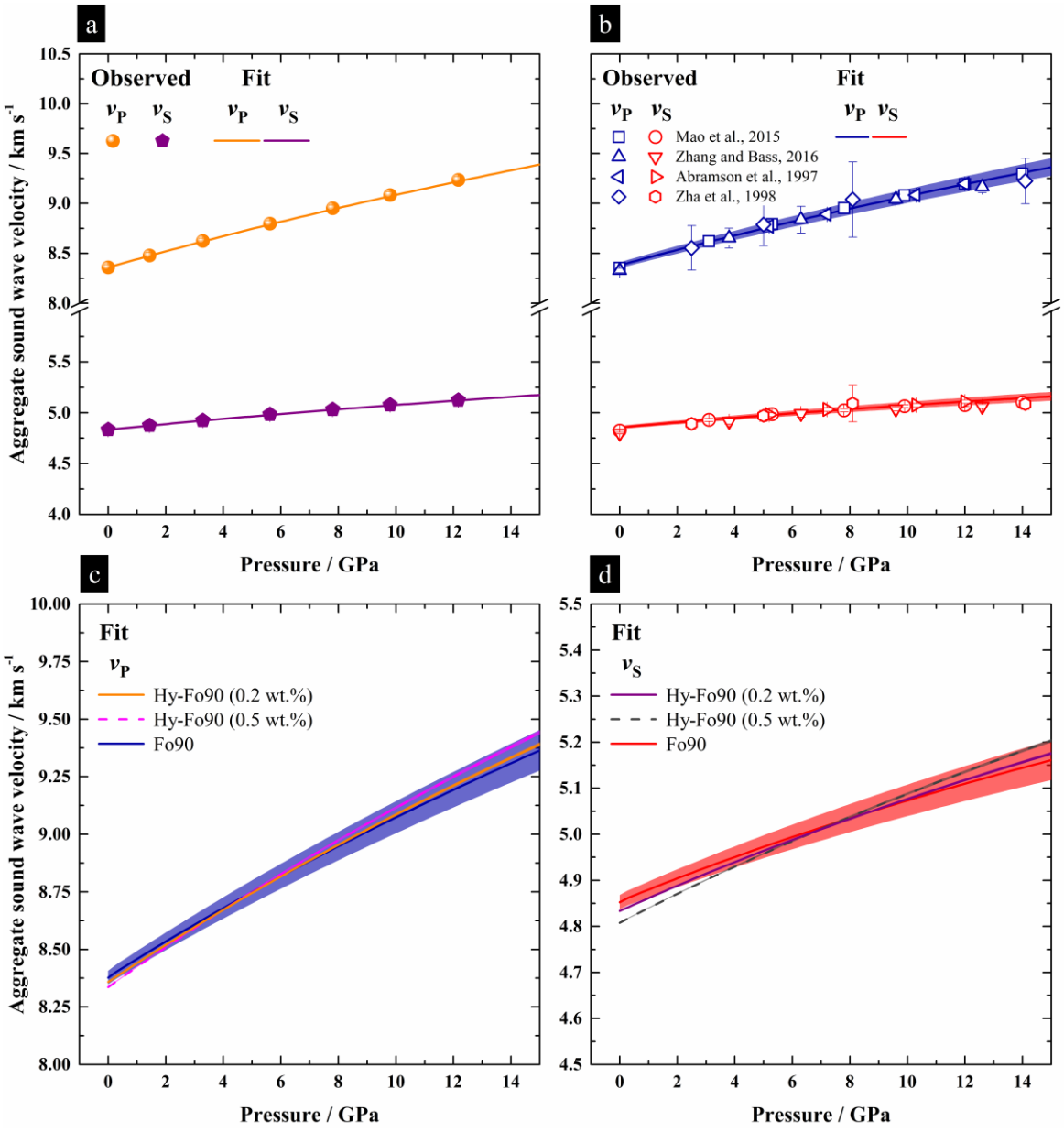


**Figure 5.6.** (a) Variation as a function of pressure of the aggregate compressional and shear wave velocities of hydrous Fo90 calculated from the experimental high-pressure elasticity measurements of this study; the solid line and shaded area the fit of the experimental data and the associated uncertainty, respectively. (b) Variation as a function of pressure of the aggregate compressional and

(*Continued*) shear wave velocities of anhydrous Fo90 calculated from previous experimental high-pressure elasticity measurements (Abramson et al., 1997; Mao et al., 2015; Zha et al., 1998; Zhang and Bass, 2016); the solid line and shaded area the fit of the experimental data and the associated uncertainty, respectively. (c-d) Superimposition of fit curves for hydrous Fo90 and anhydrous Fo90 olivine. Uncertainties are calculated by propagating the experimental errors on density and elastic moduli.

To explore whether the presence of higher water contents in olivine would cause greater effects on its $v_P$ and $v_S$, $\Delta_{H2O}M$ values obtained for Fo90 were scaled to 0.5 wt.% $H_2O$ to determine the variations in $K$, $K'$, $G$ and $G'$ associated with the incorporation of such amount of water and calculate the sound velocities of Fo90 hosting 0.5 wt.% $H_2O$ (Table 5.4, Figures 5.5c-5.6c). Because hydration causes an increase in the unit-cell volume, the room pressure volume of Fo90 with 0.5 wt.% $H_2O$ was estimated using the expression $V_{0\ \text{hydrous}}$ [Å$^3$] = $V_{0\ \text{anhydrous}}$ [Å$^3$] + 5.5 x $10^{-5}$ [Å$^3$] x $H_2O$ [ppm] from Smyth et al. (2006); $V_{0\ \text{anhydrous}}$ was calculated using the same expression solved with the data of the hydrous olivine from this study (i.e., $V_0$ = 291.65(2) Å$^3$ and ~2000 ppm). Then, the resulting volume of Fo90 with 0.5 wt.% $H_2O$ was converted into density. The calculated sound wave velocities for Fo90 with 0.5 wt.% $H_2O$ are reported in Figure 5.6c and compared to those of hydrous Fo90 with 0.20 wt.% $H_2O$ and anhydrous Fo90. The incorporation of 0.5 wt.% $H_2O$ into Fo90 olivine slightly reduces its elastic moduli (mostly $G$) and sound wave velocities at ambient pressure (Table 5.4, Figures 5.5c-5.6c). Nonetheless, $v_P$ and $v_S$ of the hydrous phase become indistinguishable within uncertainties with those of the anhydrous phase at pressures exceeding ~2 and ~5 GPa, owing to the larger $K'_{S0}$ and $G'_0$. This advises caution when speculating on the water content in the deep upper mantle based on its effect on olivine elastic properties and seismic wave velocities. Furthermore, our data also suggest that $H_2O$ incorporation in olivine may not reconcile seismological observations at the 410-km discontinuity with a pyrolitic mantle, although we are aware that direct determinations of sound wave velocities of hydrous olivine and hydrous wadsleyite at combined *HP–HT* (e.g., Buchen et al., 2018) are needed to refine these findings.

The discrepancy between the observed and calculated wave velocities for a pyrolite composition may also arise from strong variations of olivine content and upper mantle lithologies near the 410-km seismic discontinuity, for which corroborating evidence has been found by Zhang and Bass (2016). Indeed, olivine contents inferred from regional seismic models of the Pacific region are extremely variable and increase from approximately 20–40 % in the central Pacific to 60–90 % in the western U.S. and eastern Pacific regions. Given the indistinguishable seismic behaviour of hydrous and anhydrous Fo90 olivine at high pressure, we argue that this high degree of heterogeneity does not stem from the

potentially different responses of dry and wet regions of the deep upper mantle, but rather may arise from variations in olivine content.

## 5.4 Concluding remarks

The sound velocities and single-crystal elastic coefficients of Fo90 olivine with 0.20 wt.% $H_2O$ were measured up to ~12 GPa at room temperature by simultaneous single-crystal X-ray diffraction and Brillouin scattering experiments. Compared to the anhydrous phase, $K$ and $G$ of hydrous Fo90 at ambient conditions are virtually identical, while their pressure derivatives are slightly larger, although consistent within mutual uncertainties. For this reason, the elastic behaviour of hydrous and anhydrous Fo90 olivine is indistinguishable within uncertainties up to pressures corresponding to the base of the upper mantle. Using our new accurate data, we investigated the effect of hydration on aggregate sound velocities of Fo90. At ambient pressure, the compressional and shear wave velocities of hydrous Fo90 with 0.2 and 0.5 wt.% $H_2O$ are identical to, or slightly slower than, those of the anhydrous phase. In both cases however, $v_P$ and $v_S$ of the hydrous and anhydrous phases are indistinguishable within uncertainties at deep upper mantle conditions. Therefore, if amounts of water were to be incorporated into Fo90 olivine crystal structure, its elastic and seismic behaviour at high pressure may remain unchanged. Based on our findings, we suggest that water in olivine is not seismically detectable, at least for contents up to 0.2–0.5 wt.%, i.e., the amount of water expected in olivine at deep upper mantle conditions. We therefore advise caution about speculations of the water content in the deep upper mantle based on its effect on olivine elastic properties and sound wave velocities. In addition, our data also suggest that the hydration of olivine is unlikely to be a key factor in reconciling seismic velocity and density contrasts across the 410-km discontinuity with a pyrolitic mantle.

## Author contribution

[L.F.] Conceptualization, Methodology, Formal analysis, Investigation, Data Curation, Writing-Original Draft, Writing-Review & Editing; [G.C.]: Methodology, Formal analysis, Investigation, Data Curation, Writing-Review & Editing; [A.K.]: Methodology, Investigation, Writing-Review & Editing; [T.B.B.]: Methodology, Investigation, Writing-Review & Editing, Supervision; [A.W.]: Investigation, Writing-Review & Editing; [M.M.]: Writing-Review & Editing, Supervision; [F.N.]: Writing-Review & Editing, Supervision; [M.C.]: Conceptualization, Writing-Review & Editing, Supervision.

## Acknowledgments

The authors would like to thank R. Njul for his help in double-side polishing the two single crystals to platelets and D. Wiesner for her help in the operation of the FIB device. L.F. acknowledges Istituto Nazionale di Geofisica e Vulcanologia (INGV) for funding his Ph.D. project (XXXV cycle) with thematic 'Links between rheology, mineralogy and composition of the Earth's mantle' and the University of Ferrara for the 2021 IUSS international mobility program. This research was also supported by the Italian National Research Program (PRIN Grant 20178LPCPW 'Micro to Macro - How to unravel the nature of the Large Magmatic Events' to M.C.)

## Appendix A. Supplementary data

Supplementary data to this article can be found online at https://doi.org/10.1016/j.pepi.2023.107011.

## References

Abramson, E.H., Brown, J.M., Slutsky, L.J., Zaug, J., 1997. The elastic constants of San Carlos olivine to 17 GPa. J. Geophys. Res. Solid Earth 102, 12253–12263.
Angel, R.J., 2000. Equations of State. Rev. Mineral. Geochemistry 41, 35–59.
Angel, R.J., Alvaro, M., Gonzalez-Platas, J., 2014. EosFit7c and a Fortran module (library) for equation of state calculations. Zeitschrift für Krist. - Cryst. Mater. 229, 405–419.
Angel, R.J., Alvaro, M., Nestola, F., 2018. 40 years of mineral elasticity: a critical review and a new parameterisation of equations of state for mantle olivines and diamond inclusions. Phys. Chem. Miner. 45, 95–113.
Angel, R.J., Finger, L.W., 2011. SINGLE : a program to control single-crystal diffractometers. J. Appl. Crystallogr. 44, 247–251.
Bali, E., Bolfan-Casanova, N., Koga, K.T., 2008. Pressure and temperature dependence of H solubility in forsterite: An implication to water activity in the Earth interior. Earth Planet. Sci. Lett. 268, 354–363.
Bass, J.D., Anderson, D.L., 1984. Composition of the upper mantle: Geophysical tests of two petrological models. Geophys. Res. Lett. 11, 229–232.
Bell, D.R., Rossman, G.R., 1992. Water in Earth's Mantle: The Role of Nominally Anhydrous Minerals. Science (80-. ). 255, 1391–1397.
Beran, A., Libowitzky, E., 2006. Water in natural mantle minerals II: Olivine, garnet and accessory minerals, in: Reviews in Mineralogy and Geochemistry 62: Water in Nominally Anhydrous Minerals. pp. 169–192.
Boehler, R., De Hantsetters, K., 2004. New anvil designs in diamond-cells. High Press. Res. 24, 391–396.
Bonadiman, C., Hao, Y., Coltorti, M., Dallai, L., Faccini, B., Huang, Y.X., 2009. Water contents of pyroxenes in intraplate lithospheric mantle. Eur. J. Mineral. 21, 637–647.
Brodholt, J.P., Refson, K., 2000. An ab initio study of hydrogen in forsterite and a possible mechanism for hydrolytic weakening. J. Geophys. Res. Solid Earth 105, 18977–18982.
Buchen, J., 2018. The Elastic Properties of Wadsleyite and Stishovite at High Pressures: Tracing Deep Earth Material Cycles. University of Bayreuth.

Buchen, J., Marquardt, H., Speziale, S., Kawazoe, T., Boffa Ballaran, T., Kurnosov, A., 2018. High-pressure single-crystal elasticity of wadsleyite and the seismic signature of water in the shallow transition zone. Earth Planet. Sci. Lett. 498, 77–87.
Chang, Y.-Y., Hsieh, W.-P., Tan, E., Chen, J., 2017. Hydration-reduced lattice thermal conductivity of olivine in Earth's upper mantle. Proc. Natl. Acad. Sci. 114, 4078–4081.
Costa, F., Chakraborty, S., 2008. The effect of water on Si and O diffusion rates in olivine and implications for transport properties and processes in the upper mantle. Phys. Earth Planet. Inter. 166, 11–29.
Criniti, G., Kurnosov, A., Boffa Ballaran, T., Frost, D.J., 2021. Single-Crystal Elasticity of MgSiO3 Bridgmanite to Mid-Lower Mantle Pressure. J. Geophys. Res. Solid Earth 126.
Demouchy, S., Jacobsen, S.D., Gaillard, F., Stern, C.R., 2006. Rapid magma ascent recorded by water diffusion profiles in mantle olivine. Geology 34, 429.
Demouchy, S., Mackwell, S., 2006. Mechanisms of hydrogen incorporation and diffusion in iron-bearing olivine. Phys. Chem. Miner. 33, 347–355.
Downs, R.T., Zha, C.-S., Duffy, T.S., Finger, L.W., 1996. The equation of state of forsterite to 17.2 GPa and effects of pressure media. Am. Mineral. 81, 51–55.
Dziewonski, A.M., Anderson, D.L., 1981. Preliminary reference Earth model. Phys. Earth Planet. Inter. 25, 297–356.
Faccincani, L., Faccini, B., Casetta, F., Mazzucchelli, M., Nestola, F., Coltorti, M., 2021. EoS of mantle minerals coupled with composition and thermal state of the lithosphere: Inferring the density structure of peridotitic systems. Lithos 404–405, 106483.
Fei, H., Katsura, T., 2020. Pressure Dependence of Proton Incorporation and Water Solubility in Olivine. J. Geophys. Res. Solid Earth 125, 1–13.
Férot, A., Bolfan-Casanova, N., 2012. Water storage capacity in olivine and pyroxene to 14GPa: Implications for the water content of the Earth's upper mantle and nature of seismic discontinuities. Earth Planet. Sci. Lett. 349–350, 218–230.
Frost, D.J., 2008. The Upper Mantle and Transition Zone. Elements 4, 171–176.
Hirschmann, M.M., Aubaud, C., Withers, A.C., 2005. Storage capacity of H2O in nominally anhydrous minerals in the upper mantle. Earth Planet. Sci. Lett. 236, 167–181.
Hushur, A., Manghnani, M.H., Smyth, J.R., Nestola, F., Frost, D.J., 2009. Crystal chemistry of hydrous forsterite and its vibrational properties up to 41 GPa. Am. Mineral. 94, 751–760. https://doi.org/10.2138/am.2009.2990
Inoue, T., 1994. Effect of water on melting phase relations and melt composition in the system Mg2SiO4-MgSiO3-H2O up to 15 GPa. Phys. Earth Planet. Inter. 85, 237–263.
Inoue, T., Tanimoto, Y., Irifune, T., Suzuki, T., Fukui, H., Ohtaka, O., 2004. Thermal expansion of wadsleyite, ringwoodite, hydrous wadsleyite and hydrous ringwoodite. Phys. Earth Planet. Inter. 143–144, 279–290.
Jacobsen, S.D., 2006. Effect of water on the equation of state of nominally anhydrous minerals, in: Reviews in Mineralogy and Geochemistry 62: Water in Nominally Anhydrous Minerals. pp. 321–342.
Jacobsen, S.D., Jiang, F., Mao, Z., Duffy, T.S., Smyth, J.R., Holl, C.M., Frost, D.J., 2009. Correction to "Effects of hydration on the elastic properties of olivine." Geophys. Res. Lett. 36, L12302.
Jacobsen, S.D., Jiang, F., Mao, Z., Duffy, T.S., Smyth, J.R., Holl, C.M., Frost, D.J., 2008. Effects of hydration on the elastic properties of olivine. Geophys. Res. Lett. 35, L14303.
Jung, H., Karato, S.-I., 2001. Effects of water on dynamically recrystallized grain-size of olivine. J. Struct. Geol. 23, 1337–1344.
Kantor, I., Prakapenka, V., Kantor, A., Dera, P., Kurnosov, A., Sinogeikin, S., Dubrovinskaia, N., Dubrovinsky, L., 2012. BX90: A new diamond anvil cell design for X-ray diffraction and optical measurements. Rev. Sci. Instrum. 83, 125102.
Kennett, B.L.N., Engdahl, E.R., Buland, R., 1995. Constraints on seismic velocities in the Earth from traveltimes. Geophys. J. Int. 122, 108–124.

King, H.E., Finger, L.W., 1979. Diffracted beam crystal centering and its application to high-pressure crystallography. J. Appl. Crystallogr. 12, 374–378.
Kurnosov, A., Kantor, I., Boffa-Ballaran, T., Lindhardt, S., Dubrovinsky, L., Kuznetsov, A., Zehnder, B.H., 2008. A novel gas-loading system for mechanically closing of various types of diamond anvil cells. Rev. Sci. Instrum. 79, 045110.
Kurnosov, A., Marquardt, H., Frost, D.J., Ballaran, T.B., Ziberna, L., 2017. Evidence for a Fe3+-rich pyrolitic lower mantle from (Al,Fe)-bearing bridgmanite elasticity data. Nature 543, 543–546.
Mao, Z., Fan, D., Lin, J.-F., Yang, J., Tkachev, S.N., Zhuravlev, K., Prakapenka, V.B., 2015. Elasticity of single-crystal olivine at high pressures and temperatures. Earth Planet. Sci. Lett. 426, 204–215.
Mao, Z., Jacobsen, S.D., Jiang, F., Smyth, J.R., Holl, C.M., Duffy, T.S., 2008a. Elasticity of hydrous wadsleyite to 12 GPa: Implications for Earth's transition zone. Geophys. Res. Lett. 35, L21305.
Mao, Z., Jacobsen, S.D., Jiang, F., Smyth, J.R., Holl, C.M., Frost, D.J., Duffy, T.S., 2010. Velocity crossover between hydrous and anhydrous forsterite at high pressures. Earth Planet. Sci. Lett. 293, 250–258.
Mao, Z., Jacobsen, S.D., Jiang, F.M., Smyth, J.R., Holl, C.M., Frost, D.J., Duffy, T.S., 2008b. Single-crystal elasticity of wadsleyites, β-Mg2SiO4, containing 0.37–1.66 wt.% H2O. Earth Planet. Sci. Lett. 268, 540–549.
Matveev, S., O'neill, H.S.C., Ballhaus, C., Taylor, W.R., Green, D.H., 2001. Effect of Silica Activity on OH- IR Spectra of Olivine: Implications for Low-aSiO2 Mantle Metasomatism. J. Petrol. 42, 721–729.
Mosenfelder, J.L., Sharp, T.G., Asimow, P.D., Rossman, G.R., 2006. Hydrogen incorporation in natural mantle olivines, in: Earth's Deep Water Cycle. Geophysical Monograph Series 168. pp. 45–56.
Nestola, F., Nimis, P., Ziberna, L., Longo, M., Marzoli, A., Harris, J.W., Manghnani, M.H., Fedortchouk, Y., 2011. First crystal-structure determination of olivine in diamond: Composition and implications for provenance in the Earth's mantle. Earth Planet. Sci. Lett. 305, 249–255.
Novella, D., Bolfan-Casanova, N., Nestola, F., Harris, J.W., 2015. H2O in olivine and garnet inclusions still trapped in diamonds from the Siberian craton: Implications for the water content of cratonic lithosphere peridotites. Lithos 230, 180–183.
Núñez-Valdez, M., Wu, Z., Yu, Y.G., Wentzcovitch, R.M., 2013. Thermal elasticity of (Fe x ,Mg 1− x ) 2 SiO 4 olivine and wadsleyite. Geophys. Res. Lett. 40, 290–294.
Nye, J.F., 1985. Physical properties of crystals: their representation by tensors and matrices. Oxford university press.
Pamato, M.G., Nestola, F., Novella, D., Smyth, J.R., Pasqual, D., Gatta, G.D., Alvaro, M., Secco, L., 2019. The High-Pressure Structural Evolution of Olivine along the Forsterite–Fayalite Join. Minerals 9, 790.
Peslier, A.H., 2010. A review of water contents of nominally anhydrous natural minerals in the mantles of Earth, Mars and the Moon. J. Volcanol. Geotherm. Res. 197, 239–258.
Peslier, A.H., Woodland, A.B., Bell, D.R., Lazarov, M., 2010. Olivine water contents in the continental lithosphere and the longevity of cratons. Nature 467, 78–81.
Peslier, A.H., Woodland, A.B., Wolff, J.A., 2008. Fast kimberlite ascent rates estimated from hydrogen diffusion profiles in xenolithic mantle olivines from southern Africa. Geochim. Cosmochim. Acta 72, 2711–2722.
Ralph, R.L., Finger, L.W., 1982. A computer program for refinement of crystal orientation matrix and lattice constants from diffractometer data with lattice symmetry constraints. J. Appl. Crystallogr. 15, 537–539.
Regenauer-Lieb, K., 2006. Water and Geodynamics. Rev. Mineral. Geochemistry 62, 451–473.

Ringwood, A.E., 1975. Composition and Petrology of the Earth's Mantle, Mac Graw-Hill Book Company.
Sandercock, J.R., 1982. Trends in brillouin scattering: Studies of opaque materials, supported films, and central modes, in: Cardona, M., Güntherodt, G. (Eds.), Light Scattering in Solids III: Recent Results. Springer Berlin Heidelberg, Berlin, Heidelberg, pp. 173–206.
Schulze, K., Buchen, J., Marquardt, K., Marquardt, H., 2017. Multi-sample loading technique for comparative physical property measurements in the diamond-anvil cell. High Press. Res. 37, 159–169.
Shen, G., Wang, Y., Dewaele, A., Wu, C., Fratanduono, D.E., Eggert, J., Klotz, S., Dziubek, K.F., Loubeyre, P., Fat'yanov, O. V., Asimow, P.D., Mashimo, T., Wentzcovitch, R.M.M., 2020. Toward an international practical pressure scale: A proposal for an IPPS ruby gauge (IPPS-Ruby2020). High Press. Res. 40, 299–314.
Smyth, J.R., Frost, D.J., Nestola, F., Holl, C.M., Bromiley, G., 2006. Olivine hydration in the deep upper mantle: Effects of temperature and silica activity. Geophys. Res. Lett. 33, L15301.
Speziale, S., Marquardt, H., Duffy, T.S., 2014. Brillouin Scattering and its Application in Geosciences, in: Reviews in Mineralogy and Geochemistry. pp. 543–603.
Stixrude, L., Lithgow-Bertelloni, C., 2005. Thermodynamics of mantle minerals - I. Physical properties. Geophys. J. Int. 162, 610–632.
Thio, V., Cobden, L., Trampert, J., 2016. Seismic signature of a hydrous mantle transition zone. Phys. Earth Planet. Inter. 250, 46–63.
Trots, D.M., Kurnosov, A., Ballaran, T.B., Tkachev, S., Zhuravlev, K., Prakapenka, V., Berkowski, M., Frost, D.J., 2013. The Sm:YAG primary fluorescence pressure scale. J. Geophys. Res. Solid Earth 118, 5805–5813.
Trots, D.M., Kurnosov, A., Vasylechko, L., Berkowski, M., Boffa Ballaran, T., Frost, D.J., 2011. Elasticity and equation of state of Li2B4O7. Phys. Chem. Miner. 38, 561–567.
Umemoto, K., Wentzcovitch, R.M., Hirschmann, M.M., Kohlstedt, D.L., Withers, A.C., 2011. A first-principles investigation of hydrous defects and IR frequencies in forsterite: The case for Si vacancies. Am. Mineral. 96, 1475–1479.
Wang, J., Bass, J.D., Kastura, T., 2014. Elastic properties of iron-bearing wadsleyite to 17.7GPa: Implications for mantle mineral models. Phys. Earth Planet. Inter. 228, 92–96.
Wang, W., Walter, M.J., Peng, Y., Redfern, S., Wu, Z., 2019. Constraining olivine abundance and water content of the mantle at the 410-km discontinuity from the elasticity of olivine and wadsleyite. Earth Planet. Sci. Lett. 519, 1–11.
Whitfield, C.H., Brody, E.M., Bassett, W.A., 1976. Elastic moduli of NaCl by Brillouin scattering at high pressure in a diamond anvil cell. Rev. Sci. Instrum. 47, 942–947.
Withers, A.C., Bureau, H., Raepsaet, C., Hirschmann, M.M., 2012. Calibration of infrared spectroscopy by elastic recoil detection analysis of H in synthetic olivine. Chem. Geol. 334, 92–98.
Withers, A.C., Hirschmann, M.M., 2008. Influence of temperature, composition, silica activity and oxygen fugacity on the H2O storage capacity of olivine at 8 GPa. Contrib. to Mineral. Petrol. 156, 595–605.
Withers, A.C., Hirschmann, M.M., Tenner, T.J., 2011. The effect of Fe on olivine H2O storage capacity: Consequences for H2O in the martian mantle. Am. Mineral. 96, 1039–1053.
Xia, Q.-K., Hao, Y., Li, P., Deloule, E., Coltorti, M., Dallai, L., Yang, X., Feng, M., 2010. Low water content of the Cenozoic lithospheric mantle beneath the eastern part of the North China Craton. J. Geophys. Res. 115, B07207.
Xu, J., Fan, D., Zhang, D., Li, B., Zhou, W., Dera, P.K., 2020. Investigation of the crystal structure of a low water content hydrous olivine to 29.9 GPa: A high-pressure single-crystal X-ray diffraction study. Am. Mineral. 105, 1857–1865.

Xue, X., Kanzaki, M., Turner, D., Loroch, D., 2017. Hydrogen incorporation mechanisms in forsterite: New insights from 1 H and 29 Si NMR spectroscopy and first-principles calculation. Am. Mineral. 102, 519–536.
Ye, Y., Schwering, R.A., Smyth, J.R., 2009. Effects of hydration on thermal expansion of forsterite, wadsleyite, and ringwoodite at ambient pressure. Am. Mineral. 94, 899–904.
Zha, C., Duffy, T.S., Downs, R.T., Mao, H., Hemley, R.J., 1996. Sound velocity and elasticity of single-crystal forsterite to 16 GPa. J. Geophys. Res. Solid Earth 101, 17535–17545.
Zha, C., Duffy, T.S., Downs, R.T., Mao, H., Hemley, R.J., 1998. Brillouin scattering and X-ray diffraction of San Carlos olivine: direct pressure determination to 32 GPa. Earth Planet. Sci. Lett. 159, 25–33.
Zhang, J.S., Bass, J.D., 2016. Sound velocities of olivine at high pressures and temperatures and the composition of Earth's upper mantle. Geophys. Res. Lett. 43, 9611–9618.

# 6. Conclusions and future perspectives

The works in this thesis essentially comprise experimental studies and relevant modelling which address three different aspects linked to Earth's mantle physico-chemical state, structure, and dynamics. Here, concluding remarks of project (1), project (2), and project (3) will be provided, and future perspectives will be discussed.

**Project (1) – Relatively oxidized conditions for diamond formation at Udachnaya (Siberia).** Inclusions in lithospheric diamonds originate in the deep roots of cratons at depths between about 130 and 230 km and may deliver unique information about the physical-chemical environment in which their host diamonds were formed, including the nature of the medium from which diamonds grow. Redox reactions have been traditionally invoked for the formation of natural diamonds, but recently, results from thermodynamic modelling of CHO-bearing fluids indicated that decreasing temperature or ascent along a conductive geotherm reduce carbon solubility in fluids with composition near the water maximum (i.e., with a relatively oxidized character), and this may provide alternative modes of diamond formation. Corroborating evidence has been presented in this thesis, and while it is dangerous to generalize – not all diamonds formed under relatively oxidizing conditions, as the existence of inclusions of methane, carbonate or $CO_2$ demonstrates that diamonds may form over a wide range of oxygen fugacity values – determining the systematics of $fO_2$ conditions at which diamonds form requires more data on inclusions in diamonds similar to those provided here. Suitable touching-pair inclusions for oxygen fugacity determinations are very rare, whereas isolated mchr are among the more common inclusions found in diamonds. Future works shall include the investigation of a suite of mchr inclusions in Siberian diamonds, for which the $Fe^{3+}/\sum Fe$ ratios have already been determined by synchrotron Mössbauer spectroscopy, the crystal-chemical composition can be determined by single-crystal X-ray diffraction, the residence temperature by nitrogen thermometry, and the entrapment pressure by elastic geobarometry (see Nestola et al., 2019, *Sci Rep*, 9, 1-8). All these pieces of information can be exploited to calculate the chemical composition of olivines in equilibrium with mchr, to be converted into $fO_2$ values for such assemblages.

**Project (2) – EoS of mantle minerals coupled with composition and thermal state of the lithosphere: Inferring the density structure of peridotitic systems.** Studies of mantle xenoliths from all over the world have shown that the lithospheric mantle is predominantly constituted by peridotites, which span a wide range of compositions, from fertile lherzolites

to depleted/ultradepleted harzburgites and dunites. These compositional variations affect the density of the lithosphere, given that changes in whole rock compositions lead to different mineral compositions and modal mineralogy. Understanding the thermoelastic properties of mantle minerals is important to model the UM density structure, which is critical to our comprehension of the tectonic evolution of the lithosphere as well as a prerequisite for the interpretation of geophysical data. In this thesis, the EoS of mantle pyroxenes, garnet, and spinel have been assessed and combined with previously published EoS for mantle olivine and magnesiochromite to evaluate how the variations in bulk composition and thermal regimes affect the density structure of the lithospheric mantle. Results showed that variations in the thermal gradient exhibit a first-order control on the density structure of the lithosphere, while bulk composition changes have lesser effects. Future work shall include both the use of a more appropriate phase relation model and the evaluation of the thermoelastic parameters of eclogitic garnet and omphacitic clinopyroxene to model the structure and fate of the subducted slab in the UM.

**Project (3) – Sound velocities and single-crystal elasticity of hydrous Fo90 olivine to 12 GPa.** Although nominally anhydrous, natural olivines originating from the shallow UM can accommodate up to 400 ppm $H_2O$ in the form of hydrogen (H) atoms attached to structural oxygen in lattice defects. The presence of hydroxyl-bearing ($OH^-$) point defects in the crystal structure of olivine (and all NAMs) has been shown to affect several physical properties, including elasticity and the velocities of propagating sound waves. Experimental studies indicate that olivine may host up to 0.2–0.5 wt.% $H_2O$ at deeper UM conditions and thus, investigating the elastic properties and sound wave velocities of hydrous Fo90 olivine is highly warranted, as this may help in interpreting both seismic velocity anomalies in potentially hydrous regions of Earth's mantle as well as the observed seismic velocity and density contrasts across the 410-km discontinuity. In this thesis, high-pressure Brillouin scattering and single-crystal X-ray diffraction measurements have been conducted on Fo90 olivine with ~0.20 wt.% $H_2O$ and results have been complemented with a robust re-analysis of all the available single-crystal elasticity data from the literature for anhydrous Fo90 olivine. Although the elastic moduli and pressure derivatives of hydrous and anhydrous Fo90 are slightly different, our results demonstrate that the sound wave velocities of hydrous and anhydrous olivines are indistinguishable within uncertainties at pressures corresponding to the base of the UM. This suggests that water in olivine is not seismically detectable, and its incorporation is unlikely to be a key factor in reconciling seismological observations at the 410-km discontinuity with a pyrolitic mantle. Future studies shall include direct

determination of sound wave velocities of hydrous olivine at combined *HP–HT* conditions by Brillouin scattering, as well as investigations of hydrous, iron-richer samples (e.g., Fo70 - Fo80) which are more relevant to the Martian mantle.

# Acknowledgements

The National Institute of Geophysics and Volcanology (INGV) is acknowledged for funding my PhD project (XXXV cycle) with thematic 'Links between rheology, mineralogy and composition of the Earth's mantle'.
I am extremely grateful to my supervisor, Massimo Coltorti, for his unwavering support and belief in me. I would also like to extend my sincere thanks to my co-supervisors, Fabrizio Nestola (University of Padova), Maurizio Mazzucchelli (University of Modena and Reggio Emilia) and Carlo Doglioni (INGV, Rome).
Günther J. Redhammer and Michel Grégoire are also acknowledged for accepting to revise and evaluate this thesis work, giving it more credibility and robustness.
Giacomo Criniti, Tiziana Boffa Ballaran and Alexander Kurnosov are acknowledged for their assistance and immense help in the Brillouin lab at the Bayerisches Geoinstitut.
A special mention goes to my friend and colleague Federico Casetta, for always being there with his nice and encouraging words and for his training course for handling the administration.

Ai miei meravigliosi genitori, per il vostro instancabile sostegno e altruismo, per essermi da esempio tutti i giorni e per avermi cresciuto con dei valori.
Ad Andrea, semplicemente grazie per aver sempre trovato del tempo per ascoltarmi e per il tuo supporto, che spero di aver ricambiato nel corso di questi anni.
A Valeria, per essermi stata sempre vicino, soprattutto nei momenti più difficili, e per avermi saputo ascoltare e aiutare in ogni circostanza.
E a tutta la mia famiglia, che so di aver reso orgogliosa.